Universität Hamburg
Department Physik

Transverse Beam Diagnostics for the XUV Seeding Experiment at FLASH

Dissertation

zur Erlangung des Doktorgrades
des Departments Physik
der Universität Hamburg

vorgelegt von

Jörn Bödewadt
aus Geesthacht

Hamburg
2011

Gutachter der Dissertation	Prof. Dr. Shaukat Khan Prof. Dr. Markus Drescher
Gutachter der Disputation	Prof. Dr. Shaukat Khan Prof. Dr. Jörg Roßbach
Datum der Disputation	9.12.2011
Vorsitzender des Prüfungsausschusses	Dr. Georg Steinbrück
Vorsitzender des Promotionsausschusses	Prof. Dr. Peter Hauschildt
Dekan der Fakultät für Mathematik, Informatik und Naturwissenschaften	Prof. Dr. Heinrich Graener

Abstract

High-gain free-electron lasers (FEL) offer intense, transversely coherent, and ultra short radiation pulses in the extreme ultraviolet, the soft- and the hard-X-ray spectral range. Undulator radiation from spontaneous emission is amplified. Due to the stochastic emission process, the radiation exhibits a low temporal coherence, and the structure of the amplified radiation in the temporal and in the spectral domain shows large shot-to-shot fluctuations. In order to improve the temporal coherence, an external radiation pulse is used to induce (or seed) the FEL process. With this, only a defined wavelength range within the FEL bandwidth is amplified provided that the irradiance of the external radiation exceeds the noise level of the FEL amplifier. In addition to the improved longitudinal coherence, a seeded FEL provides the possibility to perform pump-probe experiments with an expected temporal resolution of the order of the pulse durations. In order to experimentally proof this statement, a test experiment for direct HHG-seeding at wavelength below 40 nm was installed at the free-electron laser facility FLASH at DESY. Crucial for the seeded operation of an FEL is the six-dimensional laser-electron overlap of the seed laser pulses with the electron bunches. Hence, dedicated diagnostics to measure and mechanisms to control the overlap are essential. Within this thesis, a transport beamline for the seed laser beam and the transverse diagnostics for seed laser- and the electron-beam were developed and commissioned. Results of the performance of the seed injection beamline are presented, and first measurements of the seeded operation of the FEL are analyzed and evaluated.

Zusammenfassung

Freie-Elektronen-Laser (FEL) erzeugen hoch intensive, transversal kohärente und ultrakurze Strahlungspulse sowohl im extrem ultravioletten Spektralbereich sowie im weichen und harten Röntgenbereich. Spontane Undulatorstrahlung wird hierfür verstärkt. Aufgrund des stochastischen Erzeugungsprozesses weist die verstärkte Strahlung eine geringe zeitliche Kohärenz auf und die zeitliche und spektrale Pulsstruktur unterliegt starken Fluktuationen von Schuss zu Schuss. Um die zeitliche Kohärenz der FEL Pulse zu verbessern, werden externe Strahlungsquellen verwendet, welche den FEL Prozess induzieren (häufig wird der Begriff "seeden" verwendet). Unter der Voraussetzung, dass die externe Bestrahlungsstärke das Rauschen des FEL-Verstärkers übersteigt, wird nur ein definierter Wellenlängenbereich innerhalb der FEL Bandbreite verstärkt. Darüber hinaus bietet ein geseedeter FEL die Möglichkeit, Pump-Probe Experimente mit einer zeitlichen Auflösung durchzuführen, die in der Größenordnung der verwendeten Pulsdauern liegt. Um diese Aussage experimentell zu verifizieren, wurde am Freie-Elektronen Laser FLASH am DESY ein Testexperiment aufgebaut, mit dem Ziel, den FEL Prozess bei Wellenlängen unterhalb von 40 nm zu seeden. Entscheidend dafür, ist der sechsdimensionale Überlapp zwischen den externen Laserpulsen und den Elektronenpaketen. Daher ist es nötig, entsprechende Diagnostik zur Messung aufzubauen, die den Überlapp messen kann, sowie die notwendigen Mittel bereitzustellen, diesen einzustellen. In dieser Arbeit wurde die Strahlführung zur Einkopplung der Seedpulse in den FEL als auch die transversale Strahldiagnostik für Laser- als auch Elektronenstrahlen entworfen, aufgebaut und in Betrieb genommen. Ergebnisse der ersten Inbetriebnahme der Einkopplung sowie erste Messungen zum geseedeten Betrieb des FEL werden analysiert und ausgewertet.

Contents

List of Figures

List of Tables

1 Introduction

The exploration of the structure and the dynamics of matter has driven the research and development of new tools to investigate processes and structures on the sub-atomic level. These tools, namely short-wavelength, high-brilliance coherent light sources, give researchers the opportunity to do fundamental studies on atoms, ions, molecules, and clusters, on the creation and characterization of warm dense matter, on diffraction imaging of nanoparticles, spectroscopy of bulk solids and surfaces, as well as surface reactions and spin dynamics [TAvB+09]. A figure of merit for characterizing a light source is the brilliance which has the unit [photons/(s mm^2 mrad^2 0.1 % bandwidth]. It describes how tight a photon beam can be focused in space and time. For more than half a century, synchrotron radiation produced by particle accelerators has been the source for probing the inner structure of matter with light. Although synchrotron radiation was at first seen as an unwanted by-product in electron synchrotrons used for high energy-physics experiments, scientists soon realized that this high-intensity, broad-spectral radiation could be used for many applications as well. These parasitically operated 'first generation' light sources were followed by electron storage rings designed, from the beginning, as synchrotron light sources of the so-called 'second generation'. Examples are BESSY I in Berlin [BES] or the NSLS in Brookhaven [NSL]. Further developments of undulators[1], optimized magnetic lattice designs for low transverse beam emittance, and sophisticated control systems allowed to increase the brilliance by orders of magnitude to up to 10^{25} photons/(s mm^2 mrad^2 0.1 % bandwidth). Most investigations are done nowadays on modern synchrotron radiation facilities offering hard X-ray pulses exceeding 100 keV photon energy like the ESRF in Grenoble (France) [ESR], PETRAIII in Hamburg (Germany) [PET], or SPring-8 in Sayo-cho (Japan)[SPR], which are examples of this 'third generation' light sources (see Fig. 1.1).

All the light sources mentioned above are based on electron or positron storage rings. The particle beam quality is characterized by the longitudinal and the transverse emittance. Due to the fact that in storage rings both emittances are determined by an equilibrium of

[1] see Section 2.1 for definition

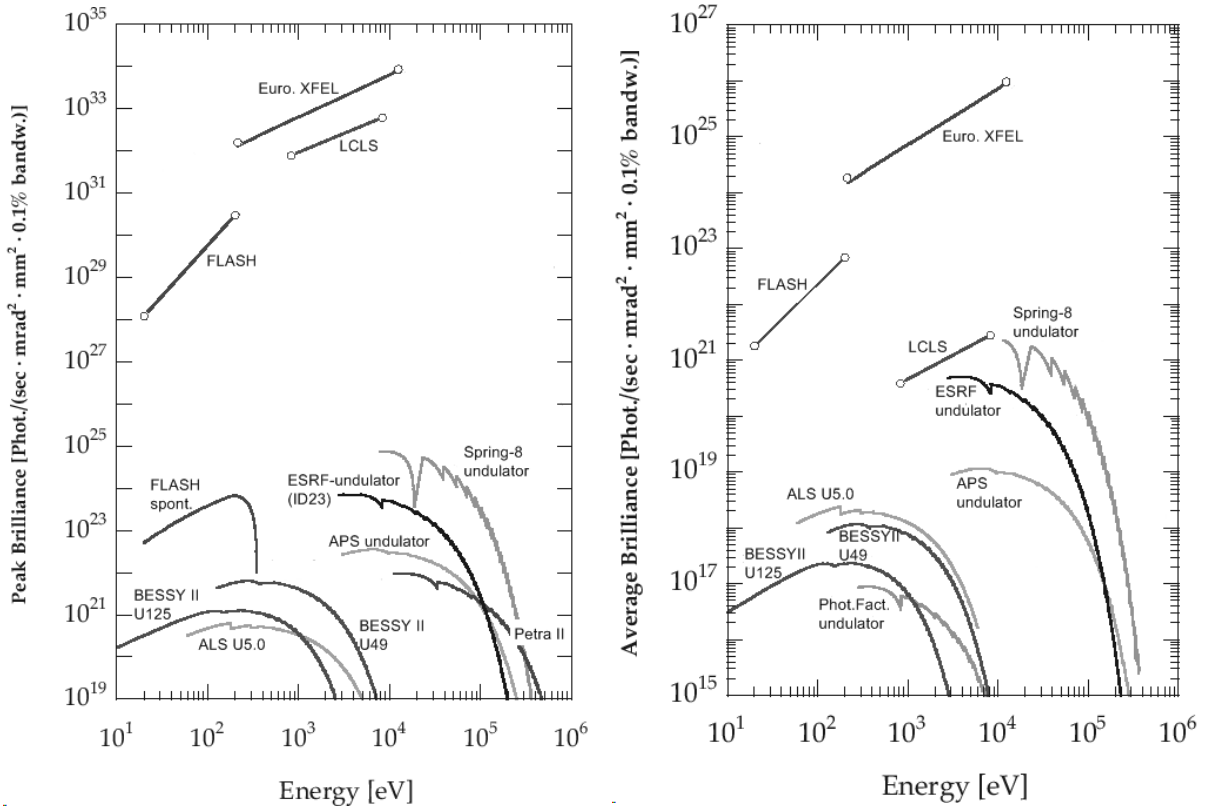

Figure 1.1: *Peak and average brilliance of various free-electron lasers and synchrotron radiation facilities as function of the photon energy [MT01].*

quantum excitation and radiation damping, these parameters have fundamental lower limits, defined by the lattice functions, the bending radii of the dipole magnets, the nominal beam energy, and the synchrotron frequency of the machine [Wie03a, Wie03b]. Typical values for the transverse emittance[2] are a few nm-rad horizontally and a few tens of pm-rad vertically. The bunch length is of the order of 10 - 100 ps defining also the radiation pulse length. Although, slicing techniques [SCC+00] exist to create shorter radiation pulses, these methods result in a highly reduced brilliance.

Another way to generate transversely coherent radiation from these beams is to monochromize the light and use spatial filter to create a point-like source. Nevertheless, only ten to hundred photons per pulse remain of the radiation pulse from the undulator.Therefore, these light sources cannot cover the physics of atomic time scales or studies on dilute samples on a single-shot basis. The invention of the free-electron laser (FEL) increased the number of coherently radiated photons per pulse by several orders of magnitude within a pulse length, which is a hundred or thousand times shorter than from a synchrotron radiation facility. The time scale that can be resolved with FELs is of the order of sub hundred femtoseconds and is basically limited by the ability to synchronize

[2]here, the not-normalized or natural emittance

external lasers to the FEL pulses and by the FEL pulse duration itself. In comparison to the synchrotron light sources of the earlier generations, high-gain FELs are driven by a linear accelerator (linac), producing a high-brightness electron beam. Operational soft- and hard-X-ray FELs are FLASH in Hamburg (Germany) [FLA], FERMI@elettra in Trieste (Italy) [FER], LCLS in Standford (USA) [LCL], and SACLA in Sayo-cho (Japan) [SAC]. Sources offering much higher temporal resolution, like soft X-ray lasers based on high-harmonic generation (HHG), with pulse durations in the sub-fs regime, have the advantage that they are intrinsically synchronized with optical laser pulses. The drawback is, again, the low photon number per pulse, making for example experiments with multi-photon excitation nearly impossible. All experiments that need both, high photon flux and good temporal resolution of the order of femtoseconds, would directly profit if one could combine the FEL with an optical laser-based light source. Such a scheme, known as laser-seeded FEL for extreme ultraviolet (XUV) and soft X-ray photons, is under development at different facilities around the world (e.g. SCSS, SPARC, FERMI@elettra). Here, the FEL is used as an amplifier for externally generated laser pulses. The challenge is to seed the FEL with a sufficiently high input signal in order to overcome the noise of the amplifier. A stable and effective coupling between seed photons and electrons in the six-dimensional phase space is essential for the reliable operation of such a light source.

At the free-electron laser in Hamburg (FLASH) at DESY an experiment to study the feasibility for XUV laser seeding using a HHG source is installed since 2010 (called sFLASH). The goal is to demonstrate FEL seeding at wavelengths below 40 nm, and to perform experiments to characterize the achievable temporal resolution for pump-probe experiments. Sophisticated diagnostics for the transverse and longitudinal photon and electron beam parameters is essential in order to reliably measure and control the laser-electron overlap. This motivates the development of compact diagnostic units being able to measure the transverse beam parameters of photons and electrons simultaneously. Within this thesis such diagnostic units were designed and commissioned. Beside that, a new injection beamline was set up to transport the seed laser pulses from the generation point into the FEL undulator. Simulations of the FEL performance for changing seed beam properties like different focusing and wavefront distortions are done in order to define the tolerances for the injection beamline optics quality. The injection beamline and its diagnostics was installed and successfully used to obtain the laser-electron overlap for the seeding experiment and to characterize the transverse photon beam properties.

2 Free-Electron Lasers

2.1 Layout of an FEL

This Section gives a brief description of the main components of a free-electron laser. In general, present-day FELs consist of an electron source to produce a high-quality electron beam, a linear accelerator to accelerate the beam up to the GeV range, and a long undulator section to produce the FEL radiation. In order to initiate the high-gain FEL process, the electron beam has to meet certain criteria. Generally speaking, the higher the electron density in the six-dimensional phase-space the easier a collective beam instability for the FEL process is driven and the faster the radiation intensity reaches its maximum and saturates. The beam instability causes the electron bunch to form a longitudinal, periodic density modulation with the same periodicity as the radiation wavelength. These micro-bunched electron beams radiate coherently and the radiation power scales quadratically with the number of electrons N_e, in contrast to the incoherent radiation where the power growth linearly with N_e. In Section 2.2.2 this phenomenon will be discussed in more detail.

Electron Source

One of the key components to generate a high-quality electron beam is the electron emitter, where the initial parameters for the electron beam are determined. Crucial for the FEL process is the transverse beam emittance which has to be sufficiently low to generate a transversely small beam spot. A large transverse emittance cannot be compensated afterwards. Commonly used electron emitters for short wavelength FELs are photo cathodes and thermionic cathodes [GDG+04]. The minimum value of the emittance is limited to the thermal emittance given by the initial kinetic energy of the released electrons and the emission area. Typical reported values for the thermal emittance are 0.3 - 0.6 mm mrad [KAB+10, TSB+04]. The repulsive space charge forces of the electrons results in an emittance growth, which can be counteracted by a rapid acceleration. For that

reason, a high accelerating field together with a transverse focusing has to be applied to the emitted electrons to achieve a final transverse emittance of the order of 1 - 2 mm mrad for typical bunch charges of 1 nC.

Accelerating Structures

Typical electron energies needed for soft- and hard-X-ray FELs are of the order of one to tens of GeV. To achieve these beam energies, RF-driven accelerating structures with high accelerating gradients are used. The main accelerators of the large FEL facilities using RF frequencies of typically between 1 and 6 GHz (e.g. FLASH: 1.3 GHz; LCLS: 2.856 GHz; SACLA: 5.712 GHz) reaching accelerating gradients of 20 to 40 MV/m, depending on the technology. For machines with low repetition rate (60 to 120 bunches per second), normal-conducting-material structures are used. Using superconducting accelerator structures gives the advantage to increase the number of electron bunches per second by up to two orders of magnitude. This is possible, because much longer RF pulses can be filled into the superconducting cavities, since the power loss is much lower compared to the normal-conducting cavities. Such machines would operate with macro-pulse trains (see also Fig. 2.5) of e.g. 10 Hz with an intra-bunch repetition rate of up to 5 MHz [ABC+07]. The challenges for the operation of the accelerating modules is to have a sufficiently low phase and amplitude jitter which requires sophisticated high- and low-level RF systems. Especially in the first accelerating structures, a jitter in phase and amplitude of the RF field results in a beam arrival time jitter at the undulator and, consequently, in a fluctuation of the arrival time of the FEL pulses at the user experiments [Löh09]. Here, the advantage of a superconducting accelerator, in comparison to a normal-conducting one, is the possibility to measure the arrival time for each bunch and set up a feedback loop that acts on the following bunches within the macro-pulse train [WKBB+10].

Bunch Compression

Since it is not possible to create electron bunches with a high peak-current ($\approx$ kA) at non-relativistic energies, where space charge effects lead to an instantaneous emittance blow-up, one has to compress the bunches during the acceleration process. The most common technique is the compression of energy-chirped bunches in magnetic chicanes, so-called bunch compressors (BC). Figure 2.1 illustrates the mechanism. The electrons are accelerated off-crest in the accelerating structures to generate an energy chirp along the bunch. Beside the fundamental RF frequency that is used for the accelerator, a higher-order harmonic RF frequency is used in order to create a linear slope on the electron bunch energy profile. The bunch tail receives higher energy relative to the head. Due to a shorter

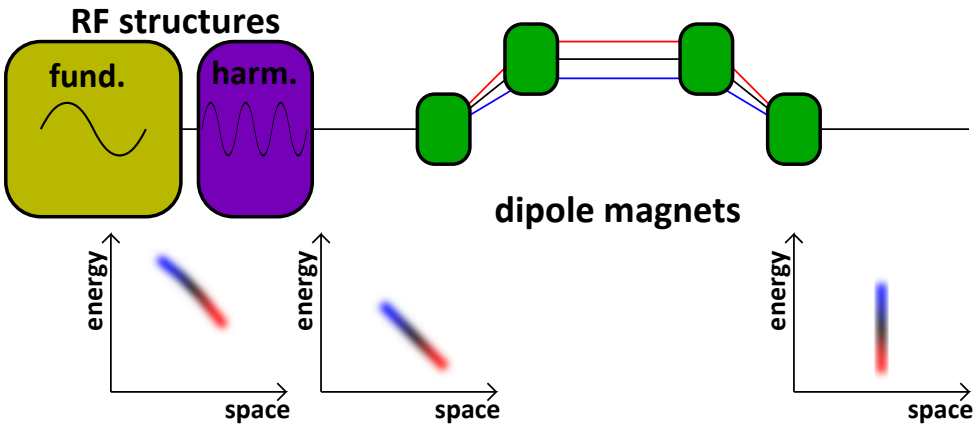

Figure 2.1: *Principle of the mechanism of electron bunch compression. The longitudinal phase space distribution (lower diagrams) shows a curvature after the first RF structure (fund.) which is linearized by a higher-harmonic RF structure (harm.). In a magnetic chicane, electrons in the tail with higher energy (blue) catch up with electrons in the head (red) due to a shorter trajectory.*

trajectory through the magnetic chicane, particles with higher energy will travel a shorter time, and therefore, catch up with particles of lower energy. Usually, the compression takes place in several stages. Further information can be found in [Stu04].

Undulator

When ultra-relativistic electron bunches travel through a magnetic structure with alternating dipole fields (wiggler or undulator), they move on a sinusoidal trajectory, thus emitting synchrotron radiation. In case of an undulator, the deflection angle of the electrons with respect to the undulator axis is smaller than the opening angle of the radiation cone of the emitted light. The maximum deflection angle depends on the particle energy and the layout of the undulator characterized by the undulator parameter

$$K = \frac{eB_u\lambda_u}{2\pi m_e c}. \tag{2.1}$$

Here, e and m_e are the electron charge and mass, respectively, c is the speed of light in vacuum, B_u is the peak magnetic field and λ_u the period length of the magnetic structure. Many different undulator technologies were developed for synchrotron radiation sources and FELs [PS09]. For soft- and hard-X-ray FELs permanent-magnet devices with fixed or variable-gap structures are in use.

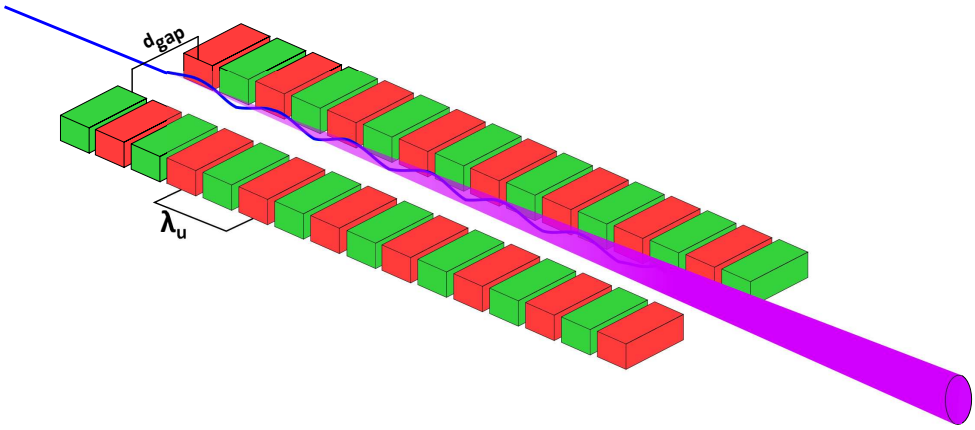

Figure 2.2: *Illustration of an electron beam on a sinusoidal trajectory creating synchrotron radiation while passing an undulator structure.*

2.2 Principle of Free-Electron Lasers

The following Sections will describe the basic principles of undulator radiation and the FEL process. Different schemes of operation modes of FELs were proposed and realized in recent years. Some of them will be discussed here.

2.2.1 Undulator Radiation

Charged particles which are deflected by the magnetic field of a dipole magnet emit synchrotron radiation with a broad continuous spectrum. It is characterized by the critical frequency

$$\omega_c = \frac{3c\gamma^3}{2R}.$$

Here, $\gamma = E/(m_e c^2)$ is the relativistic Lorenz factor for a given electron energy E, and R the bending radius of the particle trajectory. Most of the radiated power is emitted in a cone with an opening angle $1/\gamma$.
If the particles are forced to move on a sinusoidal path, the maximum deflection angle θ_{max} is given by

$$\theta_{max} = \frac{K}{\gamma}.$$

For an undulator, this angle is typically smaller than the radiation cone of the synchrotron light. Radiation emitted from different locations of the trajectory superimposes along the undulator resulting in a constructive and destructive interference. On the undulator axis,

this leads to a maximum emission of radiation at the resonance wavelengths

$$\lambda_n = \frac{\lambda_u}{2n\gamma^2} \cdot \left(1 + \frac{K^2}{2}\right), \tag{2.2}$$

with n being an odd integer. In the ideal case, the spectral width of the radiation depends only on the number of periods N of the undulator and is given by

$$\frac{\Delta\lambda}{\lambda} = \frac{1}{nN}.$$

In reality, the spectral width is increased due to the electron beam energy spread and the betatron oscillation of the individual electrons.

2.2.2 FEL Process

Free-electron lasers can be classified in low-gain and high-gain FELs. In case of the low-gain FEL, the growth rate of the radiation power for one passage of the electron bunch through the undulator is only a few percent. Nevertheless, when placed in an optical resonator, the output power of such a device can have a radiation power in the gigawatt range after multiple passages of electron bunches through the undulator.
In the high-gain FEL, the radiation field growth dramatically during one single passage of an electron bunch through a long undulator. The reason for that lies in the high charge density of the electron bunch which leads, in the presences of the periodic undulator field and a sufficient incidence radiation field, to a microbunching instability. This in turn stimulates a coherent emission of radiation that is proportional to the square of the number of electrons. Again, this enhances the microbunching even further and results in an exponential growth of the radiation power. In the so-called Self-Amplified Spontaneous Emission (SASE) mode of the FEL, the incident radiation field originates from spontaneous undulator radiation of the same electron bunch. A brief description of the one-dimensional high-gain FEL theory is given in Chapter 3.2.2.

2.2.3 Operation Modes

Since the invention of the FEL, various different ideas for operation modes were proposed and realized. Like in the language of conventional lasers, FELs can be classified as FEL oscillators and FEL amplifiers. Figure 2.3 shows an illustration of different operation modes for the FEL, which will be explained in the following Sections.

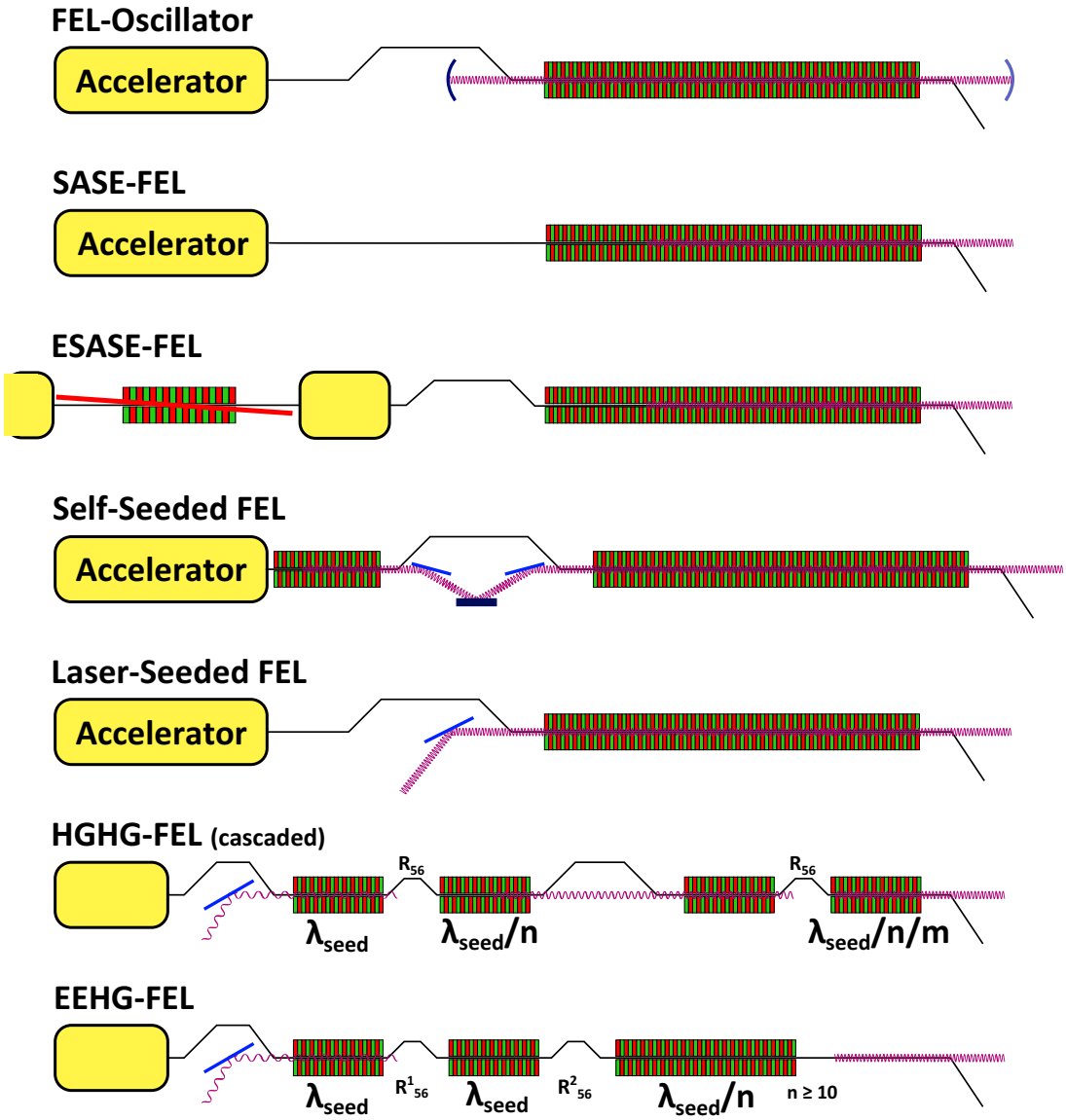

Figure 2.3: *Illustration of different possible operation modes for free-electron lasers. It shows the accelerator structures (yellow), the path of the electron beam with dipole chicanes which are essential for the operation mode, the seed laser radiation and the FEL radiation with mirrors, and the undulators. In the XUV and the soft X-ray wavelength region the SASE-FEL, the HGHG-FEL and the laser-seeded FEL mode are realized.*

FEL Oscillator - Low-Gain FEL

The first FELs were operated in the low-gain FEL regime, mostly operated as FEL oscillators (FELO). Like in a conventional laser, the light is trapped in an optical cavity. Started experimentally in the infrared wavelength range, one tried to decrease the wavelength as far as possible. Due to the lack of mirrors for wavelengths in the vacuum ultraviolet (VUV) regime or below, no FELO was realized so far in that wavelength region. First proposals for X-ray FELOs were made in the 1980th [CL84]. With the progress in accelerator technology, it seems now feasible to realize such machines [KSR08] which would give a new frontier in the average brightness for X-ray sources.

SASE - High-Gain FEL

The SASE-FEL can also be classified, in a certain way, as a laser oscillator as well as an amplifier, since the generated radiation in the first part of the undulator originates from spontaneous emission of radiation, as in a quantum laser oscillator. The advantage of this device over conventional lasers is that the wavelength can be continuously tuned. However, the spectrum or respectively pulse structure of the radiation strongly depends on the characteristics of the electron bunches. If, for example, the electron bunch length σ_b exceeds the coherence length l_c of the FEL, the radiation will consist in average of $M = \sigma_b/l_c$ longitudinal modes and therefore the radiation has a low temporal coherence (see also Chapter 3). Nevertheless, several approaches were proposed to decrease the lasing bunch length to amplify only a single longitudinal mode. At the LCLS, electron bunches with only 20 pC bunch charge were used and compressed to a few fs bunch length. Another idea is to create an energy modulation in a small fraction of the electron bunch by interaction of an external laser with the electrons in an undulator before the final acceleration. A dispersive section converts the energy modulation into a density modulation, thus creating an ultra short high-peak current section within the bunch which would produce a single-mode radiation pulse in the SASE-FEL (called enhanced SASE or short ESASE) [Zho05].

Regenerative Amplifier FEL

A combination of the SASE FEL and the oscillator FEL is given by the so-called regenerative amplifier FEL (RAFEL) which was proposed in 1997 [NFG+97] and later demonstrated in the infrared wavelength range. Here, a small portion of the output radiation of the FEL is fed back into the undulator within an optical cavity. The bandwidth of the mirrors is much smaller than the bandwidth of the FEL, and therefore, the pulse that is

fed back will act as a seed pulse with defined wavelength. Such a scheme was also proposed for the soft- and hard-X-ray regime [FFK+99, HR06], but so far not experimentally demonstrated.

Self-Seeding

To narrow the bandwidth and to increase the brightness of the FEL radiation, an operation mode called FEL self-seeding was proposed [FSS+97]. Such a two-stage FEL consists of a short SASE FEL operated below saturation whose output radiation passes a monochromator and is amplified in a second undulator. So far, no facility realized this type of operation mode, although a first test is foreseen at the Linear Coherent Light Source (LCLS) [GKS10, Fri].

Laser-Seeding

A similar idea to improve the properties of the FEL, as in the self-seeding mode, is to run a single-stage FEL in an amplifier mode using an external source with good spectral properties as radiation input (called direct seed) for the FEL. Sources in the UV spectral range are available with conventional frequency-conversion techniques using non-linear crystal materials [FHPW61]. At higher photon energies (10 - 100 eV), so-called high-harmonic generation (HHG) sources can be used (for more details see Chapter 3). The challenge here is to create a sufficiently high input power for the FEL to exceed the noise of the spontaneous emission. A proof-of-principle experiment for HHG-laser-seeding was performed at the Spring-8 Compact SASE Source (SCSS) test facility [LHG+08].

HGHG

Similar to the frequency-conversion of conventional lasers, an up-conversion of FEL frequencies is possible. For that, a longitudinal energy modulation along the electron bunch is induced by a laser-electron interaction at a wavelength λ_{seed} within an undulator, sometimes called modulator. In a dispersive section, this energy modulation is converted into a density modulation. The periodic current modulation contains more than the fundamental harmonic, and therefore, leads to coherent radiation when passing an undulator tuned to a higher harmonic of the modulator. A proof-of-principle experiment was demonstrated at the Brookhaven National Laboratory at a seed wavelength of $\lambda_{seed} = 10.6$ nm. Such a configuration, known as high-gain harmonic-generation (HGHG) FEL, can also be operated in a cascaded design, which would in principle allow to reach the hard X-ray

spectral range [WY01]. The first FEL facility using a two-staged HGHG configuration is FERMI@Elettra in Trieste (Italy) [FER].

EEHG

Another recently proposed [Stu09] scheme for a short-wavelength FEL is to make use of an effect similar to a so-called beam echo effect, which originally was observed in circular accelerators. Here, the idea is to generate an energy modulation of the electron bunch similar to the HGHG-FEL and use a dispersive section to dramatically overcompress in the longitudinal phase space. Another energy modulation of this distribution within a second undulator is performed. In a second dispersive section, this modulation can be compressed in a way that a longitudinal microbunching structure appears, leading to a periodical charge modulation at a much lower wavelength. In a third undulator, this electron bunch can radiate coherently at that wavelength. First proof-of-principle experiments where performed [XCD+10].

2.3 The FLASH Facility

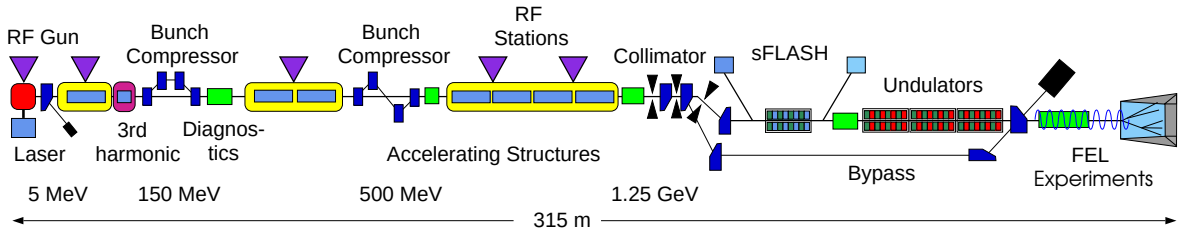

Figure 2.4: *Schematical layout of the FLASH facility. The beam direction is from left to right. The electron beam is generated in a laser-driven RF gun photo injector and accelerated up to 1.25 GeV in a superconducting linear accelerator. Two magnetic bunch compressors allow to generate high-peak current electron bunches which are sent into a 30 m long fixed-gap undulator. The generated FEL radiation is transported to the experimental hall to serve five different user beamlines. A variable-gap undulator was installed in 2010 for experimental HHG-seeding applications (sFLASH). An additional electron beamline allows to bypass the undulator section. This is typically used during accelerator studies.*

FLASH (Free-electron LASer in Hamburg) is the free-electron laser user facility at DESY [AAA+07, SFF+09]. It was originally constructed and operated till end of 2002 as a test facility for the superconducting accelerator technology (TESLA test facility, TTF) [BFR+01] and to perform a proof-of-principle experiment for the operation of a SASE FEL in the wavelength range from 120 - 80 nm [AAA+00, ABB+02a, ABB+02b]. Since 2002 the facility has been upgraded several times [SFH08]. The latest upgrade was in winter 2009/2010 [SFF+10] to increase the electron beam energy to 1.25 GeV, giving now the possibility to produce laser-like radiation in the extreme ultraviolet and soft X-ray spectral range at wavelengths down to 4.1 nm [DES10]. Since summer 2005 FLASH has been operated as an FEL user facility [SFF+09].

The FLASH facility consists of a high-brightness electron gun, seven superconducting accelerator modules, each of them equipped with eight 9-cell niobium cavities at a resonance frequency of 1.3 GHz, a module with four superconducting cavities operated at 3.9 GHz used to linearize the longitudinal phase space distribution of the electron beam, two bunch compressor sections, a collimation section, six 4.5 m long fixed-gap undulator segments, the beam dump section, the photon diagnostic beamline, and the experimental hall with five user beamlines. In addition, an experimental section between the collimator and the SASE undulator accommodates the optical replica synthesizer (ORS) experiment [ea09] as well as a variable-gap undulator for a direct laser seeding experiment (sFLASH). Furthermore, sophisticated beam diagnostics, controls, and feedback systems are installed along the whole machine. A schematic layout of the machine is shown in Fig. 2.4.

Although, the main purpose of FLASH is to deliver high-intensity XUV pulses for user experiments, it also serves as a test facility for new diagnostic techniques for the European XFEL [EXF] and as a test bed for the International Linear Collider (ILC) project [ILC].

2.3.1 Beam Production

The FLASH electron beam is generated in a laser-driven normal-conducting RF photo injector. The RF gun consists of a 1 1/2-cell TM_{010} π-mode copper cavity at 1.3 GHz operation. On its back plane, a Cs_2Te photo cathode is inserted. Electrons are emitted when the cathode is irradiated with a 262 nm wavelength laser pulse from the injector laser system. The system produces about 6.5 ps (rms) long UV laser pulses at a repetition rate of up to 3 MHz [S$^+$05]. Depending on the user requests different time structures can be chosen. Typically, 800 μs long macro-pulse trains are generated at a repetition rate of 10 Hz. The repetition rate within the pulse train can vary from 40 kHz to 1 MHz with variable number of bunches. Figure 2.5 shows a schematic of the time structure.
After electrons are emitted from the cathode, they are accelerated immediately in the electric field of the RF cavity with field gradients up to 45 MV/m [L$^+$07][1]. A solenoid magnet focuses the electrons transversely. This results in a high-brightness electron beam with a normalized emittance of typically better than 2 mm mrad at 1 nC bunch charge and at a beam energy of 150 MeV [LSC$^+$06]. By changing the laser pulse energy, the electron bunch charge can be varied between 0.1 - 3 nC. Typically, the machine runs at 0.5 - 0.8 nC.

2.3.2 Beam Compression

As described in Section 2.1, the electron bunches at FLASH are compressed longitudinally in two magnetic bunch compressors. The bunches are accelerated off-crest in the modules upstream of each compressor (ACC1 and ACC2/ACC3). The third-harmonic module ACC39 is used to linearize the longitudinal phase space distribution (see Section 2.1). The first compressor operates at 150 MeV, while the second bunch compressor works at 500 MeV beam energy.

2.3.3 Undulator Section

Downstream of the energy collimator, the undulator section starts with two 1.4 m long electromagnetic undulators for electron bunch diagnostics, followed by a 10 m long

[1] The reference reports a gradient up to 60 MV/m. This was achieved with a 10 MW klystron at PITZ. At FLASH a 5 MW klystron is used, which results in a maximum gradient of 45 MV/m.

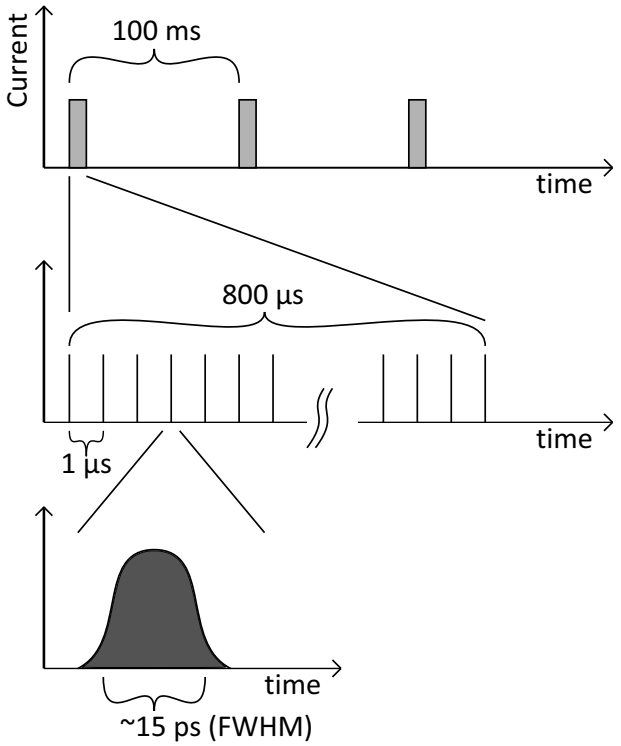

Figure 2.5: *Time structure of the electron bunches at FLASH. Macro-pulses have a repetition rate of 10 Hz. A macro-pulse contains of up to 800 bunches with a bunch spacing of 1 µs. Larger bunch spacings are possible as well. Than the number of bunches per macro-pulse decreases. The bunches are generated with a bunch length of about 15 ps (FWHM).*

variable-gap undulator and an FEL-radiation extraction chicane. The 30 m long fixed-gap SASE undulator, consisting of six 4.5 m long undulator modules, serves the experimental hall with high-intense FEL-radiation. In addition, an electromagnetic undulator after the SASE undulator generates THz radiation for far-infrared (FIR)/XUV pump-probe experiments.

2.3.4 Photon Diagnostics and Experimental Hall

The electron beam is deflected by a large dipole magnet and sent into the main beam dump. Thus, the FEL beam is separated and guided to the experimental hall. Synchrotron radiation produced in the dipole magnet is used as a reference for the arrival time of the electron beam for user experiments. In order to characterize the FEL beam, it passes several diagnostics stations. Here, different types of beam position, beam profile and intensity monitors are installed, which can on-line measure these beam properties [TAvB$^+$09]. In the experimental hall, five user beamlines (Bl1 - BL3, PG1, PG2) allow different types of experiments. Two of the beamlines (PG1 and PG2) make use of a high-resolution plane grating monochromator. In PG1, a focus spot size of approximately 5 μm (FWHM) can be realized using a special imaging optic. Toroidal or ellipsoidal mirrors are used for the other beamlines. Here, the spot sizes range between 20 and 100 μm (FWHM). A NIR laser system allows to perform pump-probe experiment at all beamlines, except for PG1. At BL3, THz radiation from the FIR undulator can be used for pump-probe studies.

2.4 The sFLASH Experiment

An experiment (sFLASH) to test the technical feasibility of direct FEL laser-seeding, using an HHG seed source and the FLASH electron beam, was proposed in 2006. The aim is to deliver intrinsically synchronized near-infrared (NIR) laser pulses and intense laser-seeded FEL pulses at wavelengths below 40 nm to a pump-probe station and to perform studies with sub-10 fs temporal resolution [MAB+08b]. Therefore, about 40 m of the FLASH electron beamline was redesigned to accommodate a new 10 m long variable-gap undulator, injection and extraction beamlines for the seed and the FEL beam, and all diagnostics needed to control the transverse and longitudinal overlap of electron bunches and photon pulses. Figure 2.6 shows a schematic layout of the FLASH beamline between the last dipole magnet of the energy collimator, where the seed laser is injected, and the existing SASE undulators. The following sections give a detailed description of the sFLASH setup.
The NIR laser pulses are generated at a repetition rate of 10 Hz in a laser laboratory adjacent to the FLASH tunnel. A small fraction of the pulse energy is directly sent to the experimental station for pump-probe applications. The main part is used for HHG. After wavelength conversion in the HHG target, the beam is sent into the FLASH tunnel, where four plane mirrors and one spherical mirror guide and focus it into the undulator. Here, the seed beam overlaps with the electron beam from the FLASH accelerator and initiates the FEL process. The amplified pulse is extracted and reflected to the experimental station. The seeded part of the FEL pulse is intrinsically synchronized with the NIR pulse coming from the laser building.

2.4.1 Seed Source

Laser System

The seed laser source is located in a laser laboratory adjacent to the FLASH tunnel. It consists of a NIR laser system and a high-harmonic generation (HHG) source. Table 2.1 summarizes the main parameters of the system. The laser pulses are generated in a passively mode-locked Ti:sapphire laser oscillator, which is pumped by a Nd:YAG laser at a repetition rate of 81 MHz. By varying the laser cavity with a piezoelectric-controlled mirror, the system is synchronized to the FLASH master laser oscillator with a precision better than 100 fs (rms) [FBG+03]. From the oscillator, the pulses are sent to the laser amplifier operated at 10 Hz, which is based on the chirped pulse amplification (CPA) technique. It consists of a pulse stretcher, a regenerative amplifier followed by a multi-pass

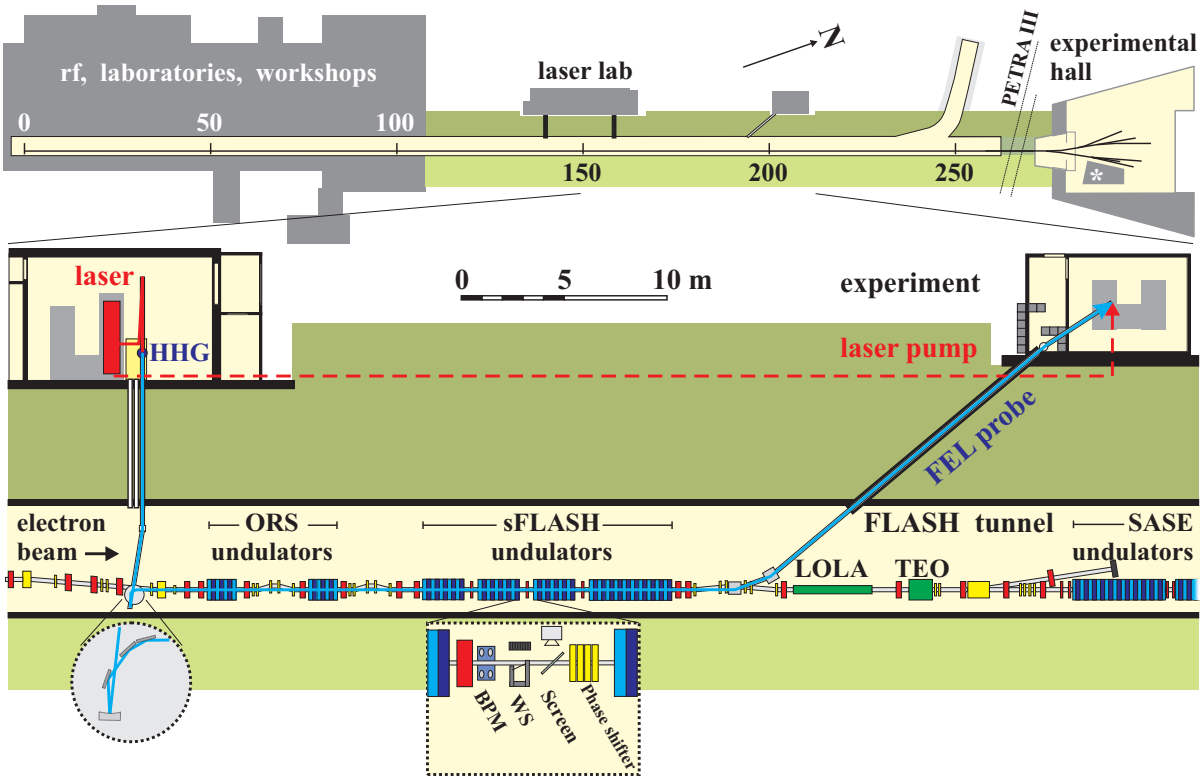

Figure 2.6: *A 40 m long section (bottom) preceding the SASE undulators was modified to accommodate four additional undulators for sFLASH. Seed pulses from the HHG source in a building adjacent to the FLASH tunnel are aligned to the electron beam by a mirror chamber before the last dipole of the energy collimator (bottom left). At the sFLASH undulator exit, the electron beam is displaced by a magnetic dipole chicane while the FEL radiation is reflected to an experimental hutch. Delayed NIR laser pulses will be sent directly to the hutch for pump-probe applications (dashed line). Dipole magnets and steerers (yellow), quadrupoles (red), as well as devices for longitudinal bunch diagnostics are shown. The insets at the bottom show details of the injection beamline, as well as the transverse beam diagnostics, like beam position monitors (BPM), wire scanners (WS), and screens between two undulator modules.*

amplifier, both pumped by the same Nd:YAG laser, and a compressor. In this system, the pulse compression is split into two compression stages. A reflective grating compressor shortens the pulses in air from several 100 ps to a few 100 fs. An in-vacuum transmission grating compressor finally compresses the pulses to about 15 fs (rms). The reason for the two-stage compression scheme is to prevent the laser pulses to be distorted by non-linear effects when traveling in air. The drawback of such a scheme is the pulse energy loss which is a factor of two higher than for one compression stage. Recently, a full in-vacuum single-stage reflective compressor was designed and is being commissioned for future experiments. For the HHG process the laser beam polarization has to be linear. At the present stage of the setup, the polarization plane is always oriented parallel to the ground level. Figure 2.8 shows a schematical layout of the seed laser system.

Parameter	**Value**
Repetition rate	10 Hz
NIR pulse energy at the HHG source	<20 mJ
NIR pulse energy stability	5 %
NIR pulse duration	(14 ± 0.1) fs (rms)
NIR center wavelength	(811 ± 0.1) nm
NIR bandwidth	(13.8 ± 0.1) nm (rms)
NIR laser M_x^2; M_y^2	1.11 ± 0.02; 1.75 ± 0.13
H21 pulse energy at the HHG source	≈ 2.5 nJ
H21 pulse energy stability	25 %
H21 center wavelength	(38.6 ± 0.2) nm

Table 2.1: *Main parameter of the NIR drive laser system and the HHG source. H21 indicates the values of the 21st harmonic of NIR laser after the HHG target. Details can be found in [Mit11].*

HHG Target

The HHG target chamber is located below the ground floor of the laser building in a 2x1.5x1.1 m^3 pit with a direct connection to the accelerator tunnel. For the HHG process, an argon gas pulse is sent into a square capillary. So far, two different dimensions for the capillary (20x1x1 mm^3 and 50x2x2 mm^3) were used for the setup. The NIR laser beam can be focused into the gas target using several focal lengths (f = 1.5 m, 3 m, 5 m, and 7 m). The target itself can be moved $\pm$ 150 mm in beam direction with respect to the laser beam focus. In addition, the target is remotely adjustable in the transverse directions. The opening time of the gas valve is typically 200-500 μs with a backing pressure of

approximately 1 bar. So far, the laser beam was focused using the focal mirror $f_1 = 1.5\,\mathrm{m}$ and $f_2 = 3\,\mathrm{m}$ which leads to beam waist sizes of the NIR laser beam of $w_0^x = 107 \pm 4\,\mu\mathrm{m}$, $w_0^y = 97 \pm 6\,\mu\mathrm{m}$ and $w_0^x = 173 \pm 2\,\mu\mathrm{m}$, $w_0^y = 186 \pm 4\,\mu\mathrm{m}$, respectively. After the HHG target chamber, three additional vacuum chambers are installed for diagnostics purposes and to allow differential pumping in order to fulfill the accelerator vacuum conditions. In the last differential pumping chamber, a mirror triplet can be moved into the beam to reflect the HHG radiation into a diagnostics branch above the pit. Here, a grating spectrometer is used to analyze the harmonic spectrum. Figure 2.7 shows a typical measurement after optimizing the 21st harmonic ($\omega_{21} = 32.1\,\mathrm{eV}$). Beside the spectrum, one can measure the far- and the near-field beam distribution of the 21st harmonic. Therefore, either two plane mirrors or one plane and one spherical mirror are inserted into the beamline, which reflect the beam to an XUV-CCD. Multi-layer mirrors guarantee that the beam is spectrally filtered and the observed beam size depicts only the 21st harmonic.

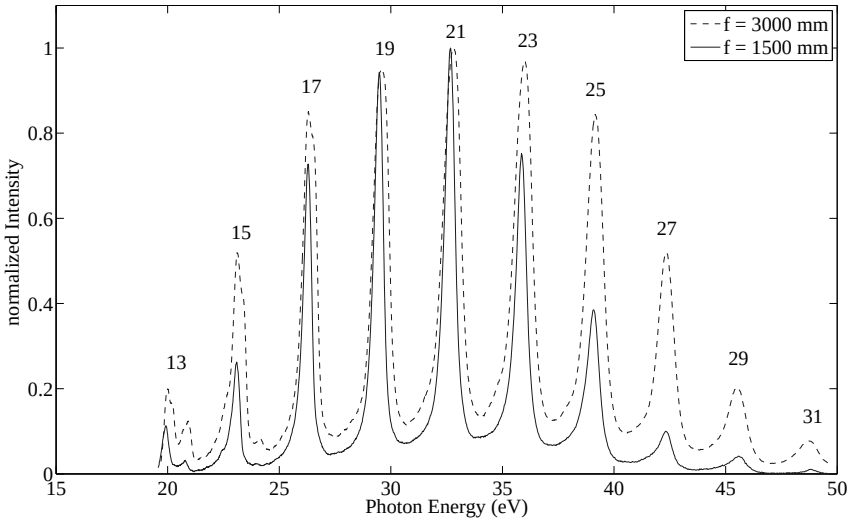

Figure 2.7: *Measured HHG spectrum for two different NIR beam focus geometries [Mit11]: f = 1.5 m (dashed line) and f = 3 m (solid line).*

2.4.2 Injection Beamline

After generating the XUV pulses, they are transported through a 12 m long vacuum beamline, injected coaxially to the electron beam, and focused into the undulator chamber. A detailed description of the design and the setup is given in Chapter 4, which is one of the two key points of this thesis. To control the transverse beam position, several diagnostics stations along the beamline are used to measure position and size of the beam. Two motorized mirror chambers allow to steer the beam. Thus, angle and position of the XUV beam at the undulator can be controlled with high precision. The transverse diagnostics setup will be discussed in detail in Chapter 5, the second key point of this thesis. One of the diagnostics stations is equipped with a streak camera in order to measure the arrival time of the XUV pulses. The streak camera is needed to ensure, that the arrival

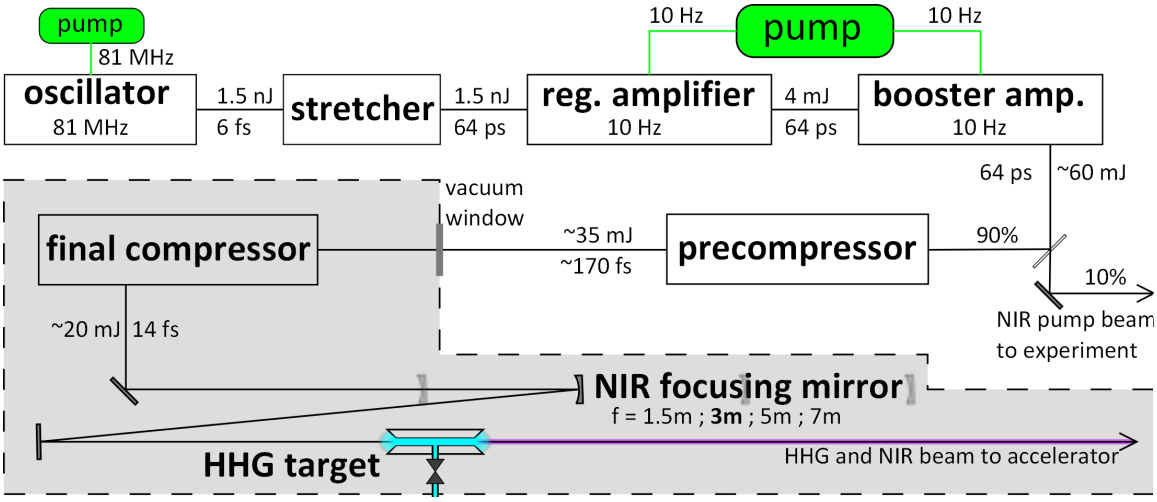

Figure 2.8: *Schematic layout of the sFLASH seed source. The NIR laser system consists of a Ti:sapphire oscillator, a pulse stretcher, a regenerative amplifier, a multi-pass amplifier (booster), and two compression stages. After the amplifier, the NIR pulses are split and 10 % of the pulse energy is sent to the experiment for pump-probe applications. The rest is used for HHG. The gray shaded area represents the in-vacuum part of the setup. After final compression of the pulses, different focusing geometries for the NIR beam into the HHG target can be realized. The HHG target consists of a capillary with a pulsed gas valve. The rms-values of the pulse durations and the pulse energies are indicated after each stage.*

time of the electron pulses with respect to the XUV pulses can be controlled with a precision below 1 ps. Detailed information about the longitudinal diagnostics can be found in [TAB+11, Tar11].

2.4.3 Undulator

The undulator system of the sFLASH experiment consists of four variable-gap undulators with an effective length of 10 m. Table 2.2 shows the main parameters of the undulators. The system is split into three 2 m long undulators (called U32) and one 4 m long undulator (called U33). The latter is a refurbished device from the PETRA II storage ring [BBH+95]. The 2 m long devices are similar to the undulators which were designed for the synchrotron radiation facility PETRA III [TBB+07]. The variable-gap undulators allow to fulfill the resonance condition for the FEL process for different electron beam energies[2]. Further information about the undulator system can be found in [DHRT+09, DHMR+09, TEM+10].

[2]Since the electron bunches are sent to the fixed-gap FLASH SASE undulators after passing the sFLASH undulators, they will generate FEL pulses for the user facility. The electron beam energy is therefore defined by the required wavelength at the SASE undulators.

	U32	U33
Min. gap [mm]	9.0	9.8
Period length [mm]	31.4	33
Number of poles	120	240
Length [m]	2	4
K value	2.72	3.03
Peak field [T]	1	1.07

Table 2.2: *Parameters of the two types of undulators for the sFLASH experiment.*

2.4.4 FEL Diagnostics

After the XUV pulses are amplified by the FEL, they are extracted from the electron beamline with an insertable mirror. A magnetic chicane is used to steer the electron beam around the mirror. A dedicated extraction beamline allows to send the FEL pulses either to a diagnostics branch, which contains an energy monitor and an XUV spectrometer ranging from 4 - 40 nm, or to the experimental station to perform pump-probe experiments with high temporal resolution.
The first mirror chamber holds three carbon-coated mirrors that deflect the beam by a total angle of 20 °. With a mirror size of 50x10 mm^2, the aperture for the beam is 2.9x10 mm^2. The chamber can be moved vertically to insert the mirrors into the electron beamline and horizontally to align the center of the first mirror to the FEL beam axis. In addition, it can be rotated to steer the FEL beam in the horizontal plane. The second mirror chamber consists of a pair of two carbon-coated mirrors, where each pair reflects the beam by a total angle of 20 °, one in the direction of the experimental hutch outside the accelerator tunnel, the other into the diagnostics branch. By horizontal movement of the chamber, the different beam directions are selected. Tilting the chamber around the incident axis allows to steer the beam in the vertical plane (to first order). Two different coating qualities on the mirrors, one with a degraded reflectivity, can be selected by vertical movement of the chamber. The coating with the lower reflectivity can be chosen if the FEL beam intensity exceeds the damage threshold of the spectrometer.
The energy monitor is located in front of the spectrometer and consists of several meshes which can be inserted into the FEL beam and three micro-channel plates (MCP). Scattered radiation from the meshes is detected by the MCPs at three different angles (0 °, 45 ° and 180 °). The two MCPs at 0 ° and 180 ° have a centric hole, so part of the FEL beam which is not scattered by the mesh can pass through the energy meter. The dynamic range of the energy monitor covers more than 7 orders of magnitude from sub-pJ

up to μJ energies. The calibration was done at one of the FLASH user beamlines at 13 nm wavelength. More information about the FEL beamline and the diagnostics can be found in [CAB+09, CAB+10].

2.4.5 Experimental Station

To perform first pump-probe experiments with the seeded FEL radiation, a new experimental station was installed adjacent to the FLASH tunnel. A fraction of each NIR laser pulse is sent through a 60 m long, length-stabilized laser transport beamline from the HHG laboratory to the experimental station. Here, it is used together with the seeded FEL pulses to perform NIR/XUV pump-probe experiments and to characterize the XUV pulses with high temporal resolution.

3 HHG Laser-Seeded FEL

An FEL operating in the direct laser-seeded mode is motivated by two arguments: The first one is the longitudinal coherence of seeded FEL pulses with respect to SASE FEL pulses. The second one is the final temporal resolution for timing experiments.
Since, in a SASE FEL, the start up of the FEL process originates from spontaneous emission, which is a stochastic process, the FEL radiation, too, is subject to stochastic fluctuations. This was theoretically predicted and also experimentally shown [STH+08]. The relevant parameter to describe the longitudinal coherence of an electromagnetic wave is the coherence time τ_{coh}. Theoretically, it is given by integrating the first-order correlation function of the electromagnetic field over all times [ST07]:

$$\tau_{coh} = \int \left| \frac{\langle E(t)E^*(t-\tau)\rangle}{\langle E^2(t)\rangle} \right|^2 d\tau.$$

It can be shown that for the case of a SASE FEL the coherence time scales approximately with the inverse FEL bandwidth σ_ω [SDR09]. If the electron bunch length is much longer than τ_{coh}, radiation pulses are amplified at statistically distributed longitudinal positions along the bunch without any correlation to each other. This leads to fluctuations of the temporal and the spectral profile of the pulses. Experiments, which need a well defined wavelength with a bandwidth smaller than the FEL bandwidth, would suffer from 100 % shot-to-shot intensity fluctuations [HK07]. Figure 3.1 shows two FEL spectra with and without seed laser.
Apart from the spectral and temporal fluctuation of the pulse structure, another important issue for pump-probe experiments is the arrival time stability of the pump pulse with respect to the probe pulse. Experiments, which have the possibility to measure the time delay between both pulses on a single-shot bases independently of the studied process, can sort their data [MCW+08]. Here, the temporal resolution is limited only by the pulse length of both pulses and by the error of the delay measurement. Other experiments could use the measured arrival time of the electron bunch in the undulator. In this case, the difficulty is to transport the signal to the user experiment, which might be some tens to hundred meter from the electron beam pick up.
At an FEL facility, the challenge is to synchronize external laser systems to the master

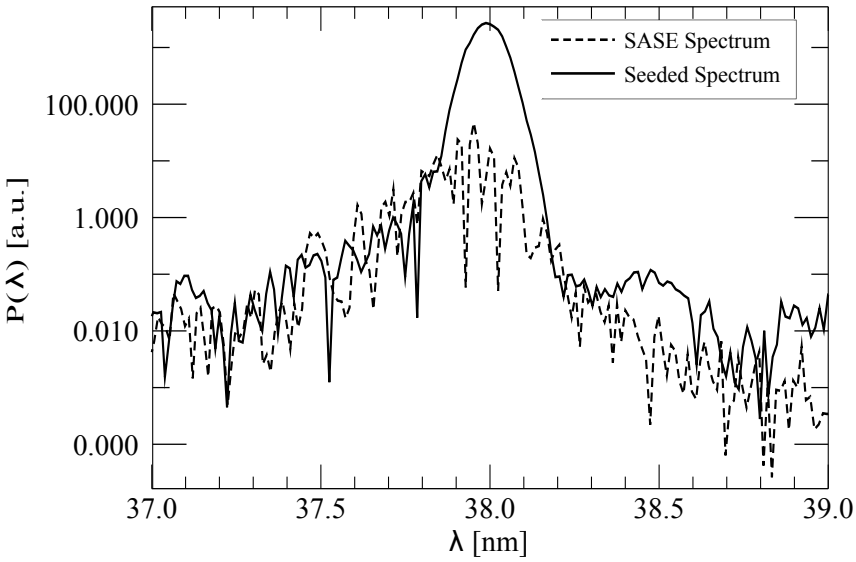

Figure 3.1: *Simulated single-shot FEL spectra after 6 m effective undulator length. Dashed: SASE; Solid: Seed laser at 38 nm with a peak power of 46 kW.*

oscillator of the RF system or to other timing signals of the machine with a temporal precision better than the FEL pulse length (typically between 30 - 100 fs). In addition, the arrival time of the electron bunches at the FEL undulator has to be stabilized with the same precision, which sets high demands on the RF regulation of the accelerator. At present-day FEL facilities, the achieved delay jitter for pump-probe pulses is of the order of 100 fs.

An ideal solution to further reduce the pulse-to-pulse fluctuations for a laser-pump FEL-probe experiment is to get the two pulses from the same source. Pulses from this source would be split. One is directly sent to the experiment and the other one used to drive the seed source for the FEL. In this case, the resolution is limited by the mechanical stability of the beamlines, which guide the two pulses to the respective end-station and by the length of the pulses.

For the XUV and soft X-ray spectral region, radiation from an HHG source is an ideal candidate as a seed laser for the FEL. The basic principles of this technology is discussed in the next Section, followed by a brief summary of the FEL seeding process.

3.1 High-Harmonic Generation

Three-Step Model

The first observation of high-harmonic generation (HHG) in rare gases was published in 1988 [FLL$^+$88] with the surprising result, that the harmonic spectrum showed a plateau of nearly constant intensities to high photon energies, which could not be explained with the available models at that time. In 1993, Corkum et al. [Cor93, LBI$^+$94] gave a semi-

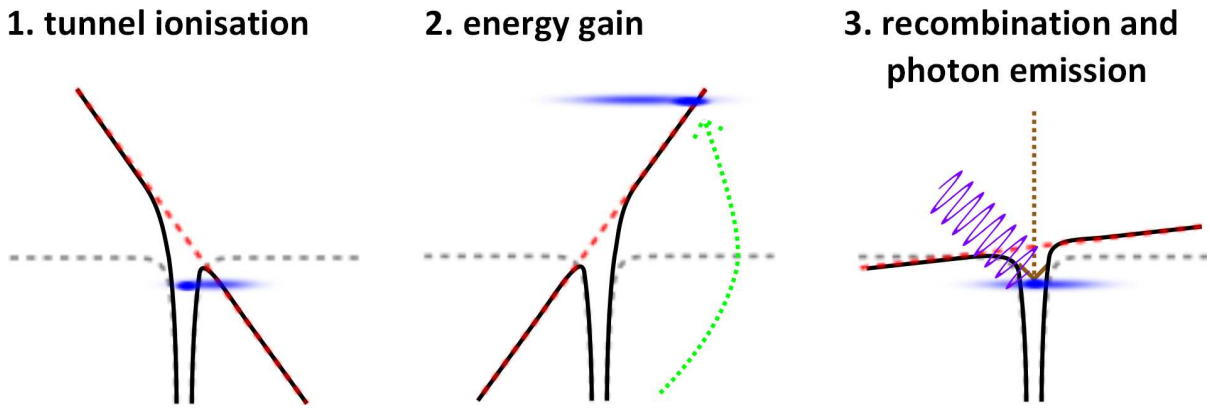

Figure 3.2: *Illustration of the semi-classical three-step model for high-harmonic generation. A strong laser field deforms the atomic potential allowing electrons to tunnel through the Coulomb barrier. Quasi-free electrons are then accelerated in the strong laser field and driven back to the core, after one half-cycle of the laser period. Here, they can recombine with the atom, which results in the emission of a high-energy photon.*

classical description of the HHG mechanism. Figure 3.2 illustrates the so-called three-step model. A strong laser field, with an intensity of the order of the Coulomb potential of an atom, bends the atomic potential. Thus, an electron has a sufficient probability to tunnel through the Coulomb barrier. This electron is accelerated by the laser field, and one half-cycle later it is driven back to the atom, where it can recombine resulting in the emission of a high-energy photon. The photon energy can be given by the kinetic energy E_c collected by the electron during the quasi-free path and by the ionization potential I_p of the atom. Since this process happens every half-cycle of the laser field, a comb of odd harmonics is generated over a wide spectral range. Due to the maximum achievable kinetic electron energy of about $E_c^{max} \approx 3.2 \cdot U_p$ [Cor93], the spectrum ends with a cutoff at $W_{cutoff} = I_p + E_c^{max}$. Here, U_p is the ponderomotive energy, which is given by

$$U_p = \frac{e^2 E^2}{4m\omega^2}$$

where e and m are the charge and the mass of the electron and ω and E are the frequency and the electric field amplitude of the laser pulse. Below the cutoff energy, two electron trajectories can result in the same photon energy, depending on the ionization time within one laser cycle. The two trajectories have different recombination times and path lengths, and are therefore called the long and the short trajectory.

Using a fully quantum mechanical approach [LBI+94, LSL95], one can derive phase information of the harmonic radiation for the long and the short trajectories, which do not only depend on the driving laser phase but also on the phase accumulated by the electron. Therefore, HHG radiation properties, like the divergence, can be deduced [HMS+09]:

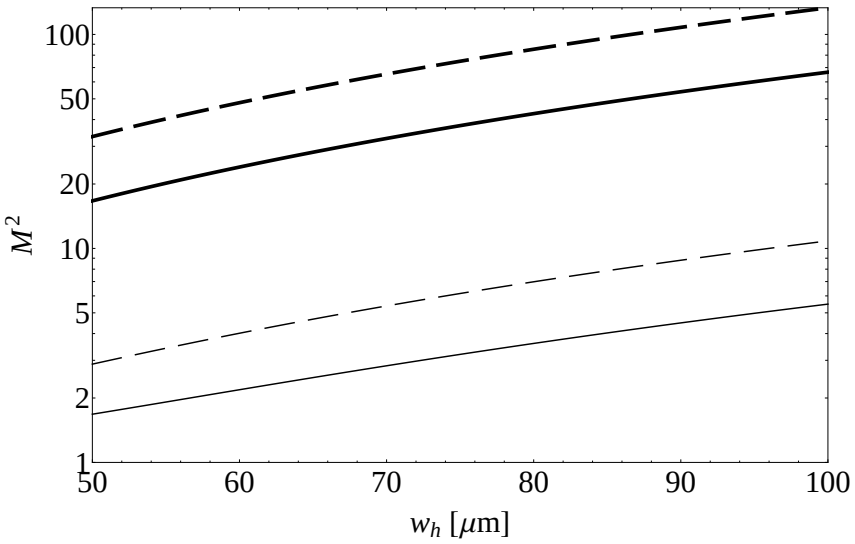

Figure 3.3: *Simulated beam quality factor M^2 of the 21st harmonic for the short (thin lines) and long (thick lines) trajectories and two different NIR intensities (solid: $1.5 \cdot 10^{14}$ W/cm^2, dashed: $3.0 \cdot 10^{14}$ W/cm^2) as a function of the HHG source size w_h .*

$$\theta_j = \frac{\lambda_h}{\pi w_h} \cdot \sqrt{1 + \alpha_j^2 I_0^2 \frac{w_h^4}{w_l^4}}. \tag{3.1}$$

Here, the subscript j indicates either the long (l) or the short (s) trajectories, λ_h and w_h are the wavelength and the beam waist size of the hth harmonic, w_l and I_0 are the beam waist size and the intensity of the drive laser and α_j is the phase-related coefficient for the long or short trajectory. If one multiplies Eq. (3.1) with w_h/λ_h, an estimate for the beam quality factor can be given (see also Eq. (C.6) in Appendix C):

$$M^2 = w_h \cdot \theta_j / \lambda_h$$

Figure 3.3 shows the calculated M^2 as a function of the harmonic beam size for the 21st harmonic of an 800 nm drive laser in Argon for both trajectories. The beam quality of the harmonic radiation will strongly decrease if the HHG process is dominated by the long trajectories. One has to test, whether radiation emitted with such a beam quality can be used for FEL seeding applications.

Phase Matching

In the previous paragraph, the microscopic single-atom process for HHG was described. To understand the macroscopic emission of radiation from HHG sources, the phenomenon of phase matching must be taken into account. Only if the phase difference $\delta\Phi_h$ between the phase of the hth harmonic field in the medium and the phase of the driving

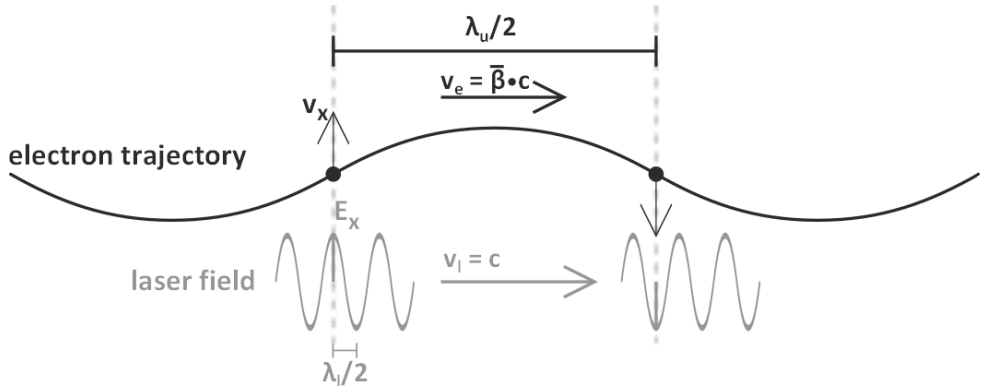

Figure 3.4: *Principle of laser-electron interaction. Electrons moving on a sinusoidal trajectory have a transverse velocity component v_x which gives the possibility to transfer energy with an external laser field E_x. If the slippage of the laser field with respect to the moving electron is $\lambda_l/2$ after a half undulator period, a continuous energy transfer takes place.*

laser pulse is minimized, constructive interference takes place and radiation in the hth harmonic is generated. This phase difference depends on the dispersion of the neutral medium and the free electrons, the focusing geometry, and the single-atom phase ($\propto \alpha_j$), mentioned above. Simulations and experiments show that it is possible to control the phase matching condition by changing several parameters, like laser intensity, focusing geometry, gas target geometry, gas density, and gas type, in order to tune the HHG properties [SLAL97, SDP+96]. For FEL seeding applications, a high photon number in a single harmonic with a low divergence and a spectral bandwidth of the order of the FEL bandwidth would be desirable.

3.2 Seeding Process

This Section gives a short theoretical introduction to the laser-electron interaction. The concept of high-gain FELs will be briefly summarized (based on reference [SDR09]), followed by a discussion of the requirements of the seed laser properties in order to overcome the noise of the FEL amplifier. More details can be found e.g. in [SDR09, ESY00].

3.2.1 Laser-Electron Interaction

The interaction of an electromagnetic wave of a laser field with electrons inside the periodic magnetic structure of an undulator is the fundamental process to explain the creation of FEL radiation. The motion of an ultra-relativistic electron traveling along the axis of a

planar undulator with a K-parameter defined in Eq. (2.1) can be approximated by

$$x(t) = \frac{K}{\gamma k_u} \sin(\omega_u t) \ , \qquad z(t) = \bar{v}_z t - \frac{K^2}{8\gamma^2 k_u} \sin 2\omega_u t, \tag{3.2}$$

where $k_u = 2\pi/\lambda_u$, $\omega_u = \bar{v}_z k_u$, the undulator period λ_u, and the average velocity of the electrons

$$\bar{v}_z = c \cdot \left(1 - \frac{1}{2\gamma^2}\left(1 + \frac{K^2}{2}\right)\right). \tag{3.3}$$

Writing the time derivative of the electron energy W_e

$$\frac{\partial W_e}{\partial t} = \vec{v} \cdot \vec{F} = -e v_x(t) E_x(t) \tag{3.4}$$

and assuming a plane electromagnetic wave E_x co-propagating with the electrons, one can see that an energy transfer from the electrons to the light field or vice verse is possible. Since the electrons are moving slightly below the speed of light and on a sinusoidal path, the electrons will lag behind the light wave. If the slippage is one optical wavelength λ_l in one undulator period λ_u, a steady energy transfer can be achieved. This is illustrated in Fig. 3.4. The time for an electron to travel one undulator period is $t = \lambda_u/\bar{v}_z$. For constant energy transfer, the light wave has to propagate a distance $\lambda_u + \lambda_l$ in the same time. Thus, it follows that

$$\frac{\lambda_u + \lambda_l}{c} = \frac{\lambda_u}{\bar{v}_z}.$$

Inserting Eq. (3.3) and solve the result for λ_l, gives the resonance condition for undulator radiation on axis

$$\lambda_l = \frac{\lambda_u}{2\gamma^2} \cdot \left(1 + \frac{K^2}{2}\right).$$

3.2.2 One-dimensional Theory of the High-Gain FEL

Discussing the high-gain FEL in the one-dimensional picture, one neglects the transverse variation of the bunch charge density and of the electromagnetic fields. In addition, the bunches are assumed to be very long, so the effects occurring at the head and the tail of the bunches can be neglected too. The theory describes the evolution of the electromagnetic field $E_x(z,t)$ and the current density $\tilde{j}_z(\psi, z) = j_0 + \tilde{j}_1(z)e^{i\psi}$ of the bunch along the undulator, with j_0 being the beam current, $\tilde{j}_1(z)$ the complex amplitude of the current modulation, and ψ the so-called ponderomotive phase[1]. The changes of the longitudinal phase space coordinates ψ and η for each particle is taken into account, where $\eta = (\gamma - \gamma_r)/\gamma_r$ is the relative energy deviation of a particle with energy γmc^2 relative to a

[1]The ponderomotive phase is related to the longitudinal position of the particle in the moving coordinate frame of the bunch.

particle with energy $\gamma_r mc^2$ which fulfills the resonant condition (2.2). The influence of the longitudinal space charge field $E_z(z,t)$ created by a modulation of the current density is considered as well. In the high-gain theory, the incident light wave is taken as the reference phase and a start phase ψ_n is assigned to each particle. For N particles in the bunch, one can derive a set of $2N+2$ coupled differential equations (for details see [SDR09]):

$$\frac{d\psi_n}{dz} = 2k_u\eta_n\,, \qquad n = 1...N \tag{3.5}$$

$$\frac{d\eta_n}{dz} = -\frac{e}{m_e c^2\gamma_r}\Re\left\{\left(\frac{\hat{K}\tilde{E}_x}{2\gamma_r} - \frac{i\mu_0 c^2}{\omega_l}\cdot\tilde{j}_1\right)\exp(i\psi_n)\right\} \tag{3.6}$$

$$\tilde{j}_1 = j_0\frac{2}{N}\sum_{n=1}^{N}\exp(-i\psi_n) \tag{3.7}$$

$$\frac{d\tilde{E}_x}{dz} = -\frac{\mu_0 c\hat{K}}{4\gamma_r}\cdot\tilde{j}_1 \tag{3.8}$$

Here, the modified undulator parameter

$$\hat{K} = K\cdot\left[J_0\left(\frac{K^2}{4+2K^2}\right) - J_1\left(\frac{K^2}{4+2K^2}\right)\right]$$

was used in order to consider the influence of the oscillatory term in the longitudinal motion of the particles in a planar undulator (see Eq. (3.2)). The $\sim$ indicates complex values. Since this set of equations describes a true many-body problem no analytical solution exists. Nevertheless, it can be used to numerically study the saturation process of an FEL amplifier, seeded by monochromatic light. To simulate the SASE process, the model has to be generalized. For details see [SDR09].

In order to analytically study the high-gain FEL process, a one-dimensional third-order differential equation can be formulated, which describes very well the exponential growth of the light field along the undulator. Nevertheless, the saturation process cannot be covered with this equation, which reads as follows:

$$\frac{\tilde{E}_x'''}{\Gamma^3} + 2i\frac{\eta}{\rho_{\mathrm{FEL}}}\frac{\tilde{E}_x''}{\Gamma^2} + \left(\frac{k_p^2}{\Gamma^2} - \left(\frac{\eta}{\rho_{\mathrm{FEL}}}\right)^2\right)\frac{\tilde{E}_x'}{\Gamma} - i\tilde{E}_x = 0 \tag{3.9}$$

The parameters in this equations are the gain parameter

$$\Gamma = \left[\frac{\mu_0\hat{K}^2 e^2 k_u n_e}{4\gamma_r^3 m_e}\right]^{1/3}, \tag{3.10}$$

the space charge parameter

$$k_p = \sqrt{\frac{2k_u\mu_0 e^2 c n_e}{\gamma_r m_e\omega_l}} \tag{3.11}$$

which depend on undulator properties and the particle density (number of particles per unit volume) n_e, and the so-called FEL parameter

$$\rho_{\mathrm{FEL}} = \frac{\Gamma}{2k_u} = \frac{1}{4\pi\sqrt{3}} \cdot \frac{\lambda_u}{L_{g0}}. \tag{3.12}$$

Here, the power gain length L_{g0} was introduced. It represents the length, at which the radiation power grows by a factor of e.
The easiest solution of Eq. (3.9) can be found if one assumes that $\eta = 0$ and $k_p = 0$, saying that the electrons are perfectly on resonance and space charge has no influence, which is in good approximation fulfilled at high energies and low electron density n_e. Inserting the ansatz $\tilde{E}_x = Ae^{\alpha z}$ in Eq. (3.9), one obtains

$$\alpha^3 = i\Gamma^3$$

with the solutions

$$\alpha_1 = (i + \sqrt{3})\Gamma/2\,, \quad \alpha_2 = (i - \sqrt{3})\Gamma/2\,, \quad \alpha_3 = -i\Gamma\,.$$

The solution for Eq. (3.9) can be written as

$$\tilde{E}_x(z) = \sum_j c_j \exp(\alpha_j z), \tag{3.13}$$

where the coefficients c_j can be computed by specifying the initial condition $\tilde{E}_x(0)$, $\tilde{E}'_x(0)$ and $\tilde{E}''_x(0)$. In the case of seeding, $\tilde{E}'_x(0) = \tilde{E}''_x(0) = 0$ and $\tilde{E}_x(0) = E_{\mathrm{in}}$ with E_{in} being the incident electric field of the seed pulse. Then, all three coefficients have the same value $c_j = E_{\mathrm{in}}/3$, and the field of the FEL pulse is

$$\tilde{E}_x(z) = \frac{E_{\mathrm{in}}}{3}\left[\exp((i + \sqrt{3})\Gamma z/2) + \exp((i - \sqrt{3})\Gamma z/2) + \exp(-i\Gamma z)\right].$$

For sufficiently large z, the electric field $\tilde{E}_x$ is dominated by the positive real part of α_1 which leads to an exponential growth. With that, the power of the light field is given as

$$P(z) \propto \frac{P_{\mathrm{in}}}{9}\exp(2\Re\{\alpha_1\}) = \frac{P_{\mathrm{in}}}{9}\exp(\sqrt{3}\Gamma z) \equiv \frac{P_{\mathrm{in}}}{9}\exp(z/L_{g0}) \tag{3.14}$$

with P_{in} being the power of the incident light wave at $z = 0$.

3.2.3 Comparision of Seeding and SASE

To compare the FEL performance of a seeded FEL with that of a SASE FEL using the one-dimensional FEL theory, one needs to make assumptions of the initial conditions for

the case of SASE. Here, $\tilde{E}'_x(0)$ is the non-vanishing term, assuming perfect resonance $\eta = 0$, and is given by the current-density modulation, stimulated by shot noise:

$$\tilde{E}'_x(0) = -\frac{\mu_0 c \hat{K}}{4\gamma_r} \tilde{j}_1.$$

With that, the amplitude of the coefficients $|c_j|$ can be calculated to be

$$|c_j| = \frac{1}{3\Gamma} \frac{\mu_0 c \hat{K}}{4\gamma_r} |\tilde{j}_1|.$$

Comparing this to the case of seeding, the equivalent input field is

$$E_{\text{equiv}} = \frac{\mu_0 c \hat{K}}{4\gamma_r \Gamma} |\tilde{j}_1| = \frac{\mu_0 c \hat{K}}{4\gamma_r \Gamma} \frac{\sqrt{e I_0 \Delta\omega}}{\sqrt{\pi} A_b}.$$

This term contains the absolute magnitude of the dc electron beam current I_0, the beam cross section A_b and the bandwidth $\Delta\omega$ of the FEL. Taking a typical parameter set for the sFLASH experiment listed in Table 3.1, the equivalent input field has a value of $E_{\text{equiv}} = 3.2\,\text{MV/m}$. The seed laser field needs to exceed this value in order to obtain a contrast larger than one. To reach this electric field, the minimum pulse energy for a pulse duration of 8 fs (rms) is $E_{\text{min}} = 14.2\,\text{pJ}$, assuming that the pulse is optimally overlapped with in electron bunch in the undulator.

3.2.4 Six-Dimensional Laser-Electron Overlap

In theory, the shape for laser and electron beam are often idealized and the overlap of both beams is assumed to be perfect. In reality, one can only match the properties of the seed laser pulse and the electron bunch in the six-dimensional phase space, namely in angle, position (each in two dimensions), time and frequency within certain tolerances. Therefore, a precise knowledge of the allowable imperfections of this overlap is mandatory. For the sFLASH parameters, a tolerance study was carried out [MAB+08a], which shows that the acceptable deviations for the angles and the transverse positions are 20 μrad and 35 μm, respectively. The allowed offset between laser pulse and electron bunch in the longitudinal dimension was calculated to be 30 fs. For this study, the beam distributions where still assumed to be ideal, meaning Gaussian distributions for the longitudinal and transverse coordinates for both beams. In addition, the beam size and the focusing geometry for the seed laser were not changed. Under the given focusing geometry a minimum seed pulse energy was given to be 1 nJ to reach the FEL saturation power. A more detailed discussion of the longitudinal tolerances with more realistic bunch distributions can be

found in [Tar11].
H tolerance analysis for the focusing geometry was performed by varying the Rayleigh length z_R of the seed laser and the longitudinal focus position z_w in the undulator. Still, the beam distributions are assumed to be Gaussian. The beam power was set to $P_{in} = 50\,kW$ corresponding to a pulse energy of 1 nJ at 8.4 fs (rms) pulse duration. Because the influence on the gain process was under study, the effective undulator length was limited to 6 m, such that the FEL can not reach into saturation. The time dependence was neglected for this simulation. With this, the electron bunch and the laser pulse are treated as infinitely long. Figure 3.5 shows the normalized output power as a function of the two parameters z_R and z_w. The optimum performance is achieved at a Rayleigh length of about $z_R = 1.4\,m$ focused at $z_w = 1.0\,m$ after the undulator entrance. The acceptable tolerance for the focus position is $\pm 0.5\,m$ for a Rayleigh length interval of 0.9 m to 2 m. For $z_R < 0.9\,m$ the performance drops relatively fast and the longitudinal focus position has to be adjusted more precisely. A larger Rayleigh length would relax the adjustment of the longitudinal focus position and also the tolerances for the transverse position at the cost of decreased output power.

parameter	**electron**	**photon**
beam energy	700 MeV	
energy spread (rms)	0.2 MeV	
norm. emittance	2 mm mrad	
beam size x/y(rms)	107/99 μm	
peak current	1.5 kA	
bunch length (rms)	80 μm	
seed wavelength		38 nm
beam power		50 kW
beam size x/y (rms)		68.5/68.5 μm
beam quality M^2		1
Rayleigh length		1.373 m
beam focus position		1.0 m

Table 3.1: *Electron and photon beam parameter used for the FEL simulation.*

3.2.5 Wavefront Tolerances

In order to quantify the allowed tolerances for the flatness of the mirrors in the seed laser beamline, the influence of wavefront distortions for the seeding process need to be studied.

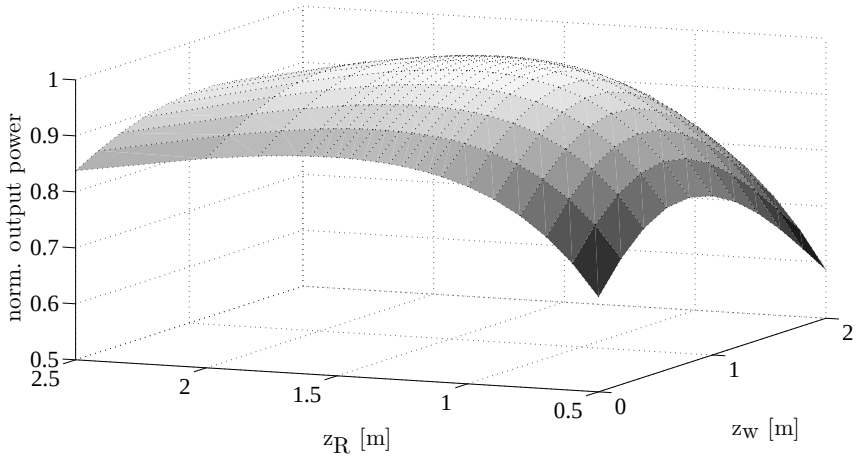

Figure 3.5: *Results of the tolerance study of the seed focus geometry.*

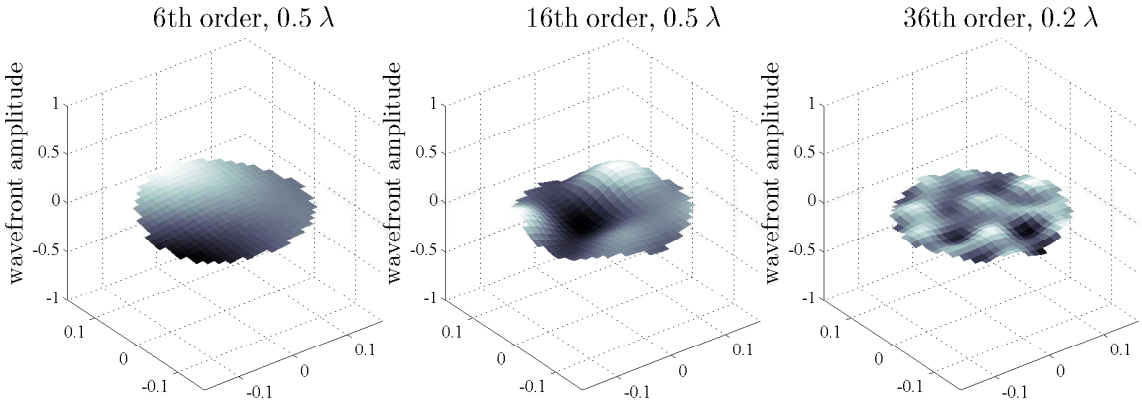

Figure 3.6: *Three exemplary wavefronts for the wavefront tolerance analysis.*

Therefore, the impact of a non-perfect wavefront for the FEL process was simulated. The FEL code GENESIS [Rei99], capable of three-dimensional time-dependent FEL simulations, together with tolerance capabilities of ZEMAX [ZEM] were used for that purpose. The influence of astigmatic wavefronts on the seeding process was studied by the diploma student Ulrich Hipp, who also developed the interface for ZEMAX to GENESIS [Hip11]. In his thesis, he concluded that the influence of the first order astigmatism has a weak impact compared to the effect of reduced laser-electron coupling due to large laser beam spots.

For the following studies the performance of the distorted wavefront simulation were compared to a beam with a flat wavefront at the undulator entrance. In other words, the beam waist was located at $z_w = 0\,\mathrm{m}$. The Rayleigh length was set to $z_R = 1{,}55\,\mathrm{m}$. The wavefront imperfections were modeled using Zernike polynomials up to different orders (6th, 16th, 26th and 36th) with varying amplitude ($\lambda/10$, $\lambda/4$, $\lambda/2$). For each order/amplitude-set 20 wavefronts were generated and used as an input for GENESIS. Figure 3.6 shows three

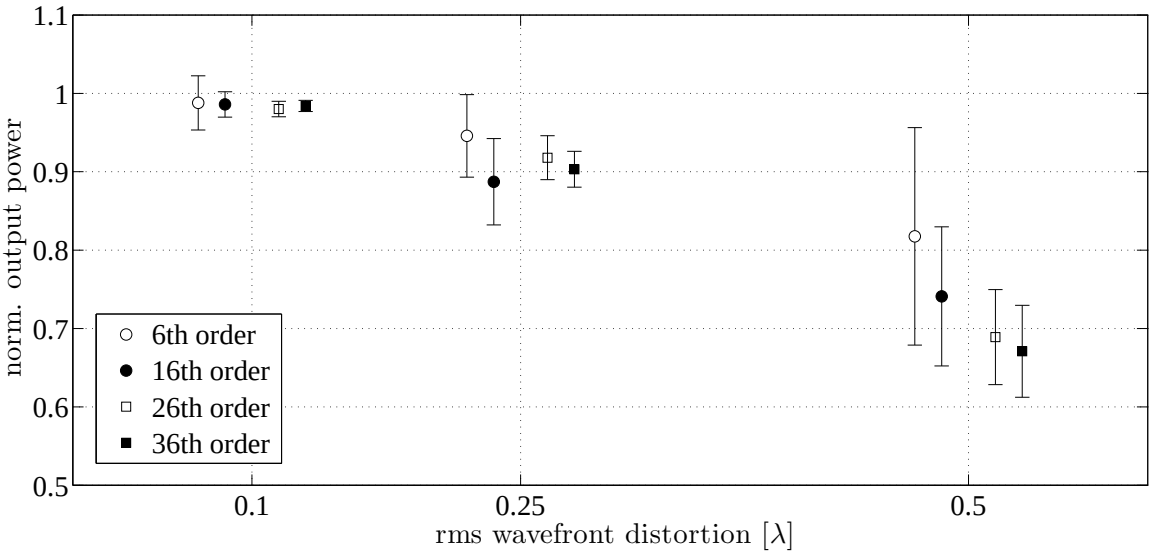

Figure 3.7: *Results of the tolerance study of the seed wavefront. For better legibility, the data points for each wavefront distortion are seperated around the nominal value at the dashed vertical lines.*

examples of generated wavefronts. The results of the analysis are shown in Fig. 3.7. One observes that for a wavefront distortion of $\lambda/10$ (rms) the FEL performance drops by about 3 % independently of the spatial frequency of the distortion. Important to mention is that for low-order distortions, there are cases, where the performance for seeding exceeds the reference case with a flat wavefront. If the wavefront error results in a beam which is focused near the center of the first undulator module at $z_{\mathrm{w}} = 1\,\mathrm{m}$, one gets closer to the optimum focusing condition discussed in the previous Section. For larger amplitudes of the distortions the FEL power drops by 10 % for $\lambda/4$ (rms) and 30 % for $\lambda/2$ (rms). Here, also a dependence on the included spatial frequencies can be seen. If one sets the tolerance for the FEL output power to 90 %, the allowable rms wavefront deformation amplitude must not exceed $\lambda/4$. For a more conservative approach one would set the wavefront tolerance to $\lambda/10$. In this case, the higher spatial frequencies have less impact on the seeding performance.

4 sFLASH Seed Beamline

4.1 Beamline Design

An injection beamline for a seeded FEL in the XUV spectral range sets high requirements for the design and the construction of the setup. In this context, the term "injection beamline" describes the beam path from the production point of the XUV radiation (here the HHG target) up to laser-electron interaction region in the undulator. The requirements for the beamline design are listed in the following itemization:

1. imaging the XUV source point at the center of the first undulator module
2. optimized XUV beam size in the undulator for maximum coupling to the electron beam
3. maximize the transmission of the XUV beam
4. XUV beam polarization has to be parallel to the undulator deflection plane
5. embedded in the existing FLASH infrastructure
6. external adjustment possibilities of the XUV beam in angle and position for the transverse laser-electron overlap
7. XUV beam position monitors
8. lowest possible wavefront distortions
9. XUV transport for the wavelengths 38 nm and 13 nm

For the sFLASH experiment, some compromises had to be found to fulfill all requirements simultaneously. Depending on the focusing strategy, the first two items in this list impose high demands on the controllability of the beam size and the beam position at the XUV source. In Section 4.1.2, this will be discussed in more detail. Point three to five in the list

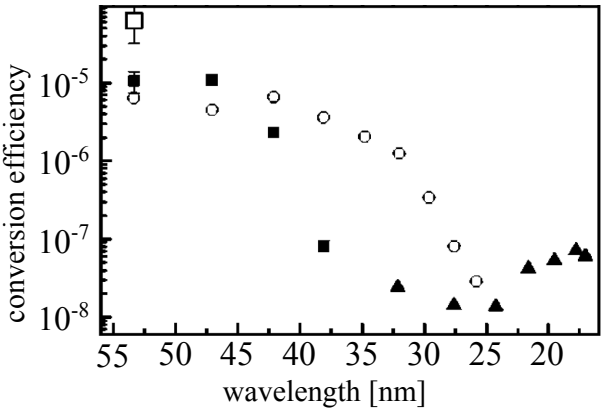

Figure 4.1: *HHG conversion efficiencies obtained in xenon (solid squares), argon (open circles), and neon (solid triangles). The open squares show the result with a larger NIR laser spot size. Taken from [HKM+02].*

are basically restricted by the existing infrastructure of the FLASH facility as discussed in Section 4.1.1. The transmission of the beamline is given by the reflectivity and the number of the reflective elements, assuming no clipping of the beam by the beamline aperture. Since the maximum reflectivity for XUV optics is of the order of 70 % for grazing angles[1] larger than 10 °, one has to keep the number of mirrors as small as possible. The possibility of steering and measuring the XUV beam within the undulator is essential in order to control the transverse laser-electron overlap along the first few gain-lengths of the FEL. In Chapter 3.2.5, the influence of wavefront distortions of the XUV radiation on the seeding process was discussed. A wavefront distortion larger than $\lambda/4$ (rms) would decrease the FEL performance by more than 10 %. This defines the demands on the tolerances of the surface quality for the XUV optics and could result in the development of an adaptive optic for the XUV spectral range. The last item of this list was given for several reasons. Besides the scientific interest in experiments at these wavelengths, there were some technical arguments to choose them: Firstly, it is known that the conversion efficiency for the HHG with the planed target geometry is higher for larger wavelengths (see Fig. 4.1 from [HKM+02]). In that sense, one expects to get enough seed power at the undulator taking the beamline transmission into account. Once, seeding is demonstrated at 38 nm, one has the option to test seeding at shorter wavelength, without opening the vacuum system to exchange the beamline optics in the FLASH tunnel. Secondly, the short-wavelength option is needed for the operation of sFLASH in parallel with the FLASH SASE mode. Since FLASH operates typically at beam energies between 0.7 GeV and 1.2 GeV, the sFLASH undulators would not have been able to fulfill the resonance condition for the higher wavelengths due to their minimum gap size. The wavelength of 13 nm would always allow to operate sFLASH, even at maximum beam energy. Thirdly, at 38 and 13 nm highly reflective multilayer coatings are available, which are used for the XUV focusing mirrors.

[1] Here, the angle is always measured from the reflective surface not from the surface normal, following the convention of X-ray optics.

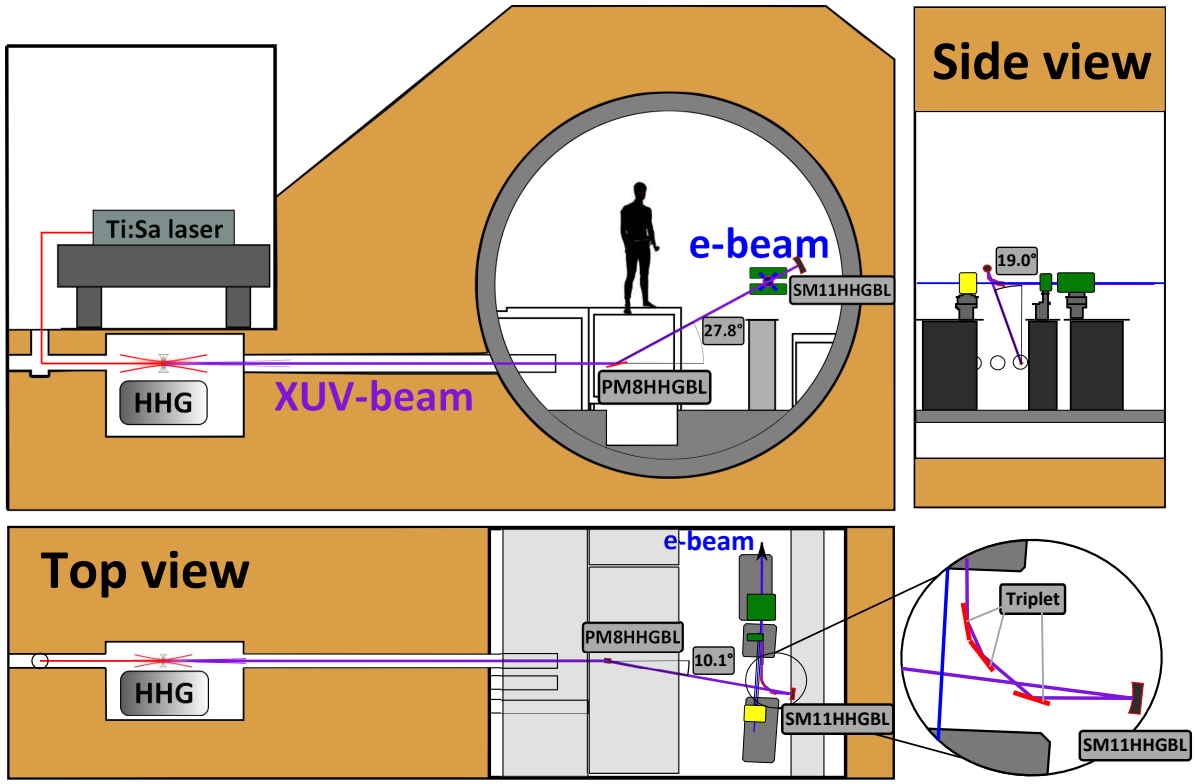

Figure 4.2: *Views of the FLASH tunnel, showing the HHG seed beamline. The first plane mirror (labeled PM8HHGBL) reflects the beam towards the electron beamline followed by a spherical mirror (SM11HHGBL) used to focus the beam into the first undulator (not shown). A plane mirror triplet (shown in the lower right detail) reflects the beam in the direction of the electron beam axis.*

4.1.1 Basic Layout

A general layout of the sFLASH setup was presented in Section 2.4. Figure 4.2 shows more detailed views of the injection beamline area. The HHG source is located in a pit below the ground level with a direct line-of-sight through a sheath tube into the accelerator tunnel. Here, the beam has to be transported about 1.2 m upwards and then bent by 90 ° to send it in the direction of the electron beam.

In general, a periscope with two mirrors tilted by 90 ° would be sufficient to bring the beam on the electron beam axis. The main aspect, why such a periscope would not work for this application, is the fact that the polarization of the beam on one of the mirrors is always p-polarized. Due to the fact that the Brewster angle for XUV radiation at 38 nm is about 54 ° measured from the surface[2], the reflectivity for the p-polarized beam is smaller than 5% at 45 °. Replacing the single mirror by a doublet, a triplet, or more mirrors,

[2]The refraction index for materials in the XUV wavelength region is lower than 1. For that reason the Brewster angle is larger than 45 ° with respect to the surface!

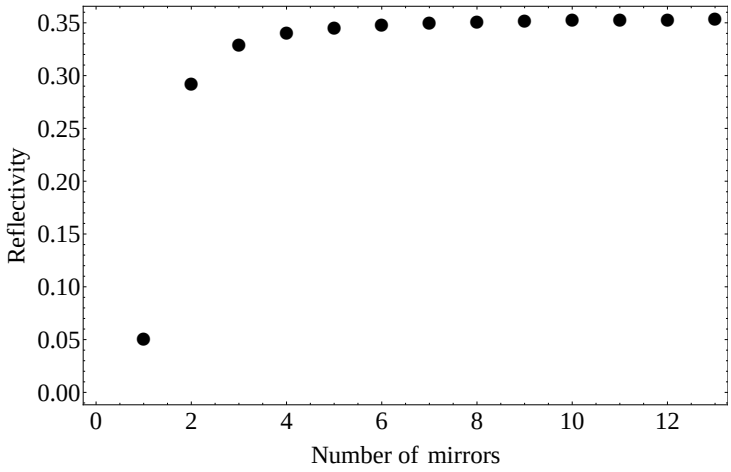

Figure 4.3: *Reflectivity as a function of the number of mirrors used to bend a p-polarized XUV (38 nm) beam by 90° in total for a typical XUV coating material B_4C. Data taken from [HGD93].*

would allow a total bending angle of 90° with a reflectivity up to about 35 %. Figure 4.3 illustrates that the reflectivity for such a system does not depend on the number of mirrors for more than four mirrors. Therefore, depending on the space availability, one would use a system of three to five mirrors.
For sFLASH, a total amount of five mirrors in the injection beamline is used. One flat mirror at an incident angle of 13.9° reflects the beam upwards (labeled with *PM8HHGBL* in Fig. 4.2) where the beam hits a spherical multilayer mirror (*SM11HHGBL*) nearly at normal incidence. Afterward, it is reflected by 84° using a triplet of flat mirrors. The side view in Fig. 4.2 shows that the first mirror (*PM8HHGBL*) has also a yaw angle of 19°. This allows to decrease the bending angle for the triplet.

4.1.2 Beam Focusing

In Chapter 3, the dependencies of the transverse beam properties on the seeding process were discussed. In order to experimentally achieve the optimum condition for the XUV beam focusing into the undulator, the beam parameters are controlled either by changing the XUV source parameters or by manipulating the beam within the transport beamline using defocusing and focusing mirrors.
To reduce the total number of reflective elements, it was decided to include only one focusing element in the injection beamline with the possibility to change the focal length of this element by exchanging the mirror. With that, the possibility to set the focal point at different positions along the undulator is given (see Fig. 4.4). The drawback is that it is not possible to change the beam size in the undulator while maintaining the focus position in the center of the undulator. Thus, one sets high demands on the development of the HHG source, since the optimum focus size in the undulator is determined by the HHG source point.

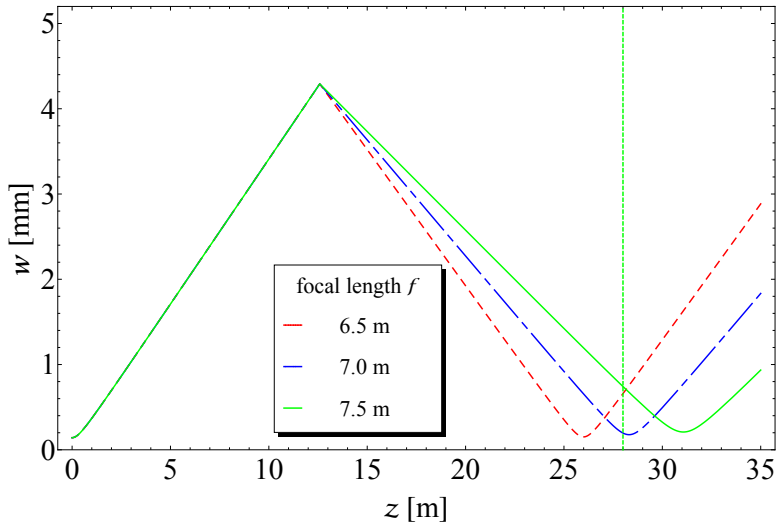

Figure 4.4: *XUV beam size w along the injection beamline for different focal lengths f. The vertical line indicates the center position of the first undulator module at $z = 28\,\mathrm{m}$ (image point). The zero position represents the center of the HHG target chamber.*

To define the optimum source parameters for the given setup and for the required beam parameters at the undulator, a simple model using the Gaussian beam propagation algorithm (see Appendix C.3) was used. The focal length of the mirror can be estimated by geometric optics. For the given object length $g = 12.59\,\mathrm{m}$ and image length $b = 15.41\,\mathrm{m}$, the focal length is $f \approx 7\,\mathrm{m}$. Other input parameters for the model are the beamline element positions (HHG waist position z_w^{HHG}, the position of the focal mirror z_{mirror} and the undulator position z_{Und}), the XUV source size w_0^{HHG} and the beam quality factor M^2 (see Appendix C).
Figure 4.5 determines graphically the optimum source parameters for three different M^2 values. The solid lines represent all possible combinations of z_w^{HHG} and w_0^{HHG} for which the beam waist is located at the center of the first undulator module. The dashed lines give the parameters which create the appropriate spot size of $170\,\mu\mathrm{m}$. The geometrical solution is indicated by the black dot. For the case of a diffraction-limited beam, the wave nature of the beam is still visible. For a two or three times diffraction-limited beam the geometrical approximation can be used.

4.1.3 Beam Polarization Analysis

Since the sFLASH undulator deflects the electron beam horizontally, only the electric field component of the XUV beam parallel to this deflection plane will couple to the electron beam. In order to predict the performance of the injection beamline in terms of the polarization and transmission of the incoming XUV beam, a simulation was performed using the optical design software ZEMAX [ZEM]. The model includes the exact beamline geometry as well as the data for the XUV mirror coatings. Table 4.1 lists the different coatings for the plane mirror and the spherical mirror substrates. The reflectivity data

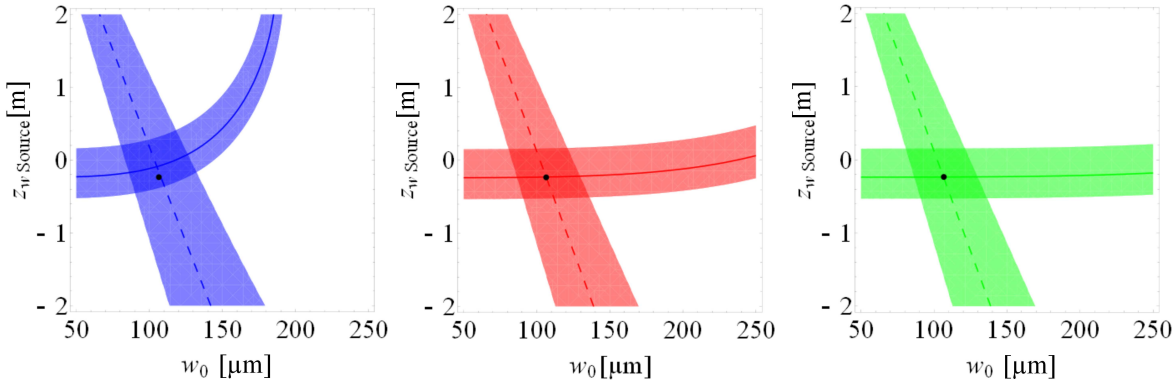

(a) (b) (c)

Figure 4.5: *Parameter space for the HHG source position z_w^{HHG} and the HHG source size w_0^{HHG} for different M^2 values. The solid line represents all values (z_w^{HHG},w_0^{HHG}) for which the source is imaged at $z = 28\,m$. The dashed line represents all values (z_w^{HHG},w_0^{HHG}) for which the focus size in the undulator equals 170 µm. The intersection of both lines marks the optimum parameter set. The shaded areas represent the tolerances band for the focusing tolerances calculated in 3.2.5. The black dots represent the solution using geometrical optics. (a) $M^2 = 1$; (b) $M^2 = 4$; and, (c) $M^2 = 9$.*

and the absolute phase change for the different coatings for s- and p-polarized beams are shown in Appendix B.

substrate type	**size**	**coating material**	**thickness**
plane (for 38 nm)	25x100 mm^2	Ti/B_4C	7.5 nm/40 nm
plane (for 13 nm)	25x100 mm^2	Mo/B_4C	47.5 nm/2.5 nm
spherical (for 38 nm)	25.4 mm	15 layers Sc/Si + B_4C	d = 19.68 nm, $\gamma = 0.38$
spherical (for 13 nm)	25.4 mm	40 layers Mo/Si + B_4C	d = 7.09 nm, $\gamma = 0.43$

Table 4.1: *Coating data for the beamline mirrors. The plane mirror substrates are coated with a single layer. The spherical substrates used at normal incidence are coated with multilayer coatings where d is the layer periodicity and γ the ratio of the thicknesses of each element within one period. All mirrors have a protection coating of B_4C.*

The XUV beam at the HHG source is linearly polarized. In order to find the theoretically best input polarization for the beamline, the angle of this linear polarized beam was varied at the entrance of the injection beamline from $-\pi$ to π where 0 means horizontal polarization. The electric field component parallel (E_x) and perpendicular (E_y) to the deflecting plane of the undulator, as well as the phase differences between these components were calculated and are plotted in Fig. 4.6. In addition, the transmission of the intensity

is shown in this figure. If the phase difference is zero, the beam is linearly polarized. This situation is achieved with an input polarization angle of -4.6 ° and -94.6 °. In the first case, the electric field components parallel to the deflection plane of the undulator is close to its maximum value of about 45 % with respect to the input field amplitude, while it is below 20 % for a polarization of -94.6 °.

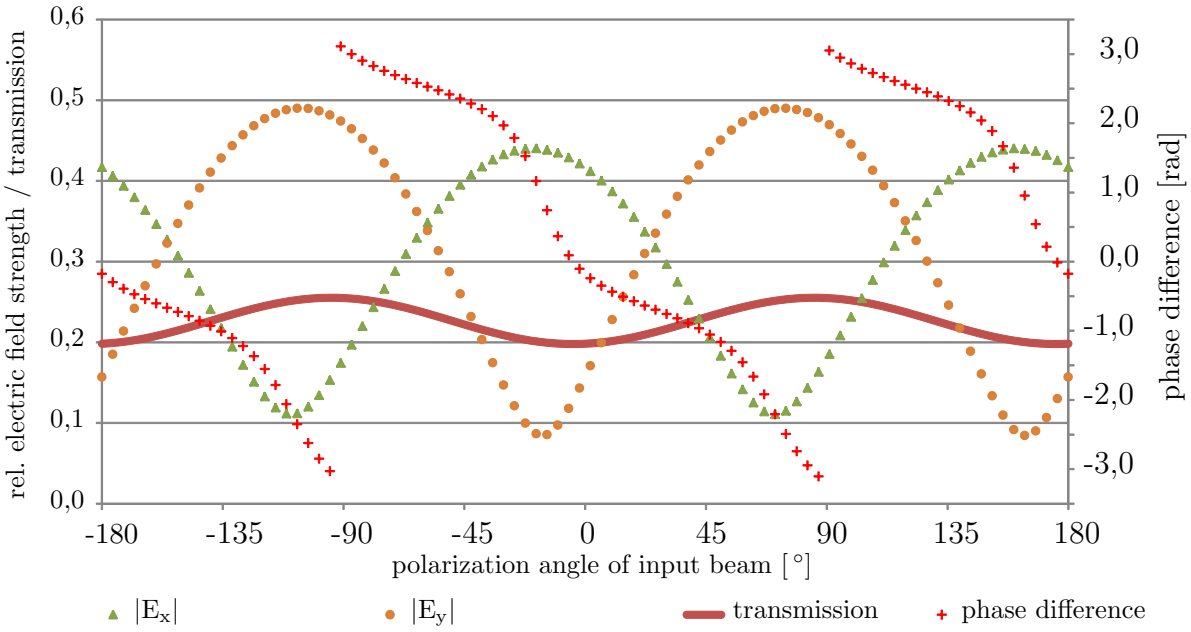

Figure 4.6: *Injection beamline transmission, electric field strength, and phase difference of both electric field components parallel (E_x) and perpendicular (E_y) to the deflection plane of the undulator at the end of the beamline relative to the field at the beginning of the beamline.*

4.1.4 Beam Steering Concept

To achieve the transverse overlap between the electron beam and the photon beam, different strategies can be followed. Either one sets the electron beam on its reference orbit and then aligns the photon beam to this orbit, or one adjusts the electron orbit to a given position defined by the laser beam. In either way, the laser beam orbit in angle and position has to be fine-tuned. For that, at least two mirrors of the injection beamline have to be remotely movable in two, preferable orthogonal, dimensions. For the sFLASH beamline, this is realized in the following way. The first mirror *PM8HHGBL* is able to be pitched and yawed, which will change the angle of the outgoing beam, resulting in a change of the beam position at the focal mirror *SM12HHGBL*. A shift of this mirror in the transverse directions, on the one hand, can maintain the emission point on the mirror, on the other hand can be used to change the angle of the reflected beam. These four degrees of freedom are sufficient to control beam angle and position along the undulator. Due to technical

reasons (for explanation see Appendix E) the focal mirror can additionally be tilted. The last three mirrors (triplet) *PM12HHGBL1*, *PM12HHGBL2* and *PM12HHGBL3* are stationary.

In order to define the required positioning accuracy for each degree of freedom, a ray-trace model was used to simulate the beam response for each mirror movement. Based on the tolerances for the transverse overlap (35 μm, 20 μrad) discussed in chapter 3.2.4 the adjustment tolerances were calculated. Table 4.2 lists the results of this calculation for both mirrors.

Mirror	**Pitch [μrad]**	**Yaw [μrad]**	**x [μm]**	**y [μm]**
PM8HHGBL	1.0	2.0	-	-
SM12HHGBL	0.65	0.65	10	10

Table 4.2: *Required angle and position accuracy for movable mirrors in the sFLASH injection beamline.*

5 Transverse Beam Diagnostics

In order to control the transverse overlap of laser and electron beam within the required tolerances (see Section 3.2.4), position and angle of each beam have to measured with a precision smaller than these tolerances. As discussed in Chapter 3, the transverse overlap has to be maintained along the first few gain lengths of the FEL. Besides the transverse position of both beams, the beam sizes are important to achieve an effective coupling. Therefore, the longitudinal focus position and the focus spot size of the XUV beam, as well as the beam size of the electron beam along the undulator has to be determined. Preferably such measurements should be done parasitically.

Several different diagnostic techniques to measure transverse electron or photon beam properties are available. Those, which are compatible with the ultra-high vacuum (UHV) conditions required for these beams, will be briefly summarized in this chapter.

A direct, but fully destructive, way to measure transverse beam profiles and positions is to insert a pixel detector inside the beam and extract the transverse beam information shot-by-shot. The resolution is simply given by the distance from pixel to pixel. An indirect method is to insert a material into the beam path which produces a signal (preferably) proportional to the beam intensity and observe this signal, again with a pixel detector. Here, a single shot measurement of the full transverse beam profile is possible, although the interaction process of the beam with the material should be known. For XUV photon beams, such methods are usually fully destructive if using solids like phosphor or fluorescence screens since the beam is absorbed by the material. By using gas for the interaction, almost fully non-destructive measurements can be done. Highly relativistic electron beams can penetrate through solid screens, but usually the beam quality is degraded afterwards, and the beam cannot be used for FEL application, which makes the measurement fully destructive. Less destructive, but without single-shot capability, is the usage of wire scanners, which can be used for electron and photon beams. This method allows only to measure projections of the beam profiles.

Since it is technically not possible to insert a screen or a wire scanner directly inside the undulator of an FEL, one has to measure the beam in front and between the undulator modules, and estimate the beam size inside the undulator using an appropriate model.

Figure 5.2 schematically shows an overview of the injection beamline and its diagnostic stations for the sFLASH project. The XUV beam and the electron beam diagnostics are separately discussed in the following sections. A good overview of detector methods, not only for high energy photons, but ionizing radiation in general, can be found in [Leo94].

5.1 XUV Photon Diagnostics

For XUV photons, there is a set of different detector methods available to measure the beam properties. Most of them are destructive methods, since the detector has to be put directly into the beam to extract the full information of the beam profiles. Non-destructive methods, like gas-monitor detectors or wire scanners only absorb or scatter a tiny fraction of the beam energy, but, as mentioned before, they can only measure projections of the beam profile.

5.1.1 Phosphor and Scintillator Screens

Scintillators and phosphors are used to convert the energy of ionizing particles, like high-energy photons or electrons, into visible light. In combination with other detectors, they allow an indirect measurement of the beam profile. Commonly used types of scintillator materials are organic crystals, organic liquids, plastics, inorganic crystals, gases, and glasses. The physical process of absorption and re-emission of energy, known as luminescence, is divided into the rapid or instantaneous emission of light (fluorescence) of the order of 10^{-8} s and the delayed processes (phosphorescence) ranging from a few microseconds to several hours. For imaging applications of recurring short-pulsed beams, one is usually interested in fluorescence materials.
A widely used material [MRBZ$^+$00] for electron and photon beam diagnostic in particle accelerators is cerium-doped yttrium aluminum garnet (Ce:YAG, $Y_3Al_5O_{12}$: Ce), an inorganic crystal with a decay constant between 60 and 70 ns and a maximum emission wavelength at around 550 nm, well suited for detection with standard light imaging sensors[MRBZ$^+$01, MKZ00]. It is compatible for ultrahigh-vacuum applications and is mechanically robust.

5.1.2 Semiconductors

Semiconductor materials are used for the direct conversion of light energy into measurable currents, since the band structure in the semiconductor allows the direct excitation

of an electron from the valence band into the conduction band if the irradiated photon energy exceeds the band gap. Commonly used semiconductor materials for photon detection are silicon, germanium, and indium gallium arsenide (InGaAs). Each photodiode, charge-coupled device (CCD) sensors, complementary metal oxide semiconductor (CMOS) sensors, or detectors using photocathodes are based on this basic principle of photon detection, allowing a wide range of applications. With that, a wavelength range from the infrared to the hard X-ray regime can be covered by these detectors.

5.1.3 Photomultiplier

A photomultiplier (PMT) consists of a photocathode, several electrodes called dynodes, and an anode. Each consecutive dynode has a higher positive voltage than the previous one. If a photon with sufficient energy hits the cathode electrons are emitted by the photoelectric effect. These electrons are accelerated to the first dynode, where secondary emission causes a multiplication of the incidence electrons by a factor of about ten. These electrons are in turn accelerated to the second dynode and so on. After several stages, a multiplication of one million or higher can be reached resulting in an easy detectable signal at the anode. All components need to be mounted in an evacuated tube (usually glass). In combination with a scintillator, this device can be used for all kinds of particle detection.

5.1.4 Micro-Channel Plates

Like PMT, micro-channel plates (MCP) use the effect of secondary emission to amplify an incident electron by several orders of magnitude. Here, multiplication takes place in small channels (10^4 to 10^7) build into an about 2 mm thin slab of a highly resistive material with typical channel diameters of 10 - 100 μm per channel [Wiz79]. Due to the high density of multiplication channels, this device offers a much higher spatial resolution compared to the PMT. Electrons and ions, as well as photons with energies exceeding the work function of the slab material, can be detected with MCPs. Special coatings are used to increase the efficiency for certain photon wavelengths. Typically, the detection efficiency for XUV photons is of the order of 10 % and the open area ratio (ratio between channel to interchannel area) is typically about 60 % [SiG]. A single MCP allows amplification factors up to 10000. By placing two or three plates in series (configurations called Chevron and Z-stack, respectively) a total gain of 10^{10} is possible.
MCPs are used e.g. in image intensifiers, where the incident photons are amplified in an MCP and the emitted electrons are accelerated to a scintillator screen. The fluorescence

can be viewed by a standard CCD sensor or by eye.

5.1.5 Gas-Monitor Detectors

In so-called gas-monitor detectors, an XUV beam travels through a thin atmosphere of rare gas atoms (10^{11} atoms/cm^3), which are ionized by the XUV photons. A homogeneous electric field collects the electrons and ions at respective detectors [RGK$^+$03]. With that, it is possible to get a position and intensity information of the XUV beam [TFH$^+$08]. Using the same principle, a so-called ionization profile monitor was used to measure the beam position and the projected beam profile on-line [MSM$^+$11].

5.2 Electron Beam Diagnostics

5.2.1 Optical Transition Radiation Screens

Optical transition radiation (OTR) was theoretically predicted in 1945 [GF45]. Whenever a charged particle crosses a boundary of two media with different dielectric constants, the electric field carried by the electron has to be reorganized [Git92]. During that process, electromagnetic waves are emitted from the boundary in forward and backward direction. In the case of an ultra-relativistic electron and a material with a dielectric constant $|\epsilon| > 1$, the angular and spectral single-particle intensity distribution is given by

$$\frac{d^2I}{d\omega d\Omega} = \frac{e^2\beta^2}{4\pi^2 c} \cdot \frac{\sin^2\theta}{(1-\beta\cos\theta)^2},$$

where $\beta = v/c$, v is the electron velocity and θ emission angle of the radiation with respect to the incident particle direction. The maximum intensity is radiated at an angle $\theta_m = 1/\gamma$. The electric field is linearly polarized in the plane containing the normal of the interface and the direction of emission. For an electron bunch of N particles the incoherent emission of radiation scales directly with N. The radiation is incoherent, as long as the longitudinal structures of the bunch are longer than the observed radiation wavelength. If these structures are shorter than that, the radiation is emitted coherently (COTR) and scales with $N^2 \cdot F(\omega)$, where $F(\omega)$ is the longitudinal form factor of the bunch (see [DH08] for further information).

Optical transition radiation in the visible spectral range is a widely used technique at particle accelerators for transverse beam diagnostics. As long as there are no short-scale structures in the bunch distribution, imaging OTR to a CCD detector gives single-shot information about the transverse profile of the particle beam. With the development

of high-brightness low-emittance electron beams for high-gain FELs, the appearance of COTR became a serious problem for beam diagnostics based on OTR [WS11] because the intensity distribution does not reflect the charge distribution in the transverse plane anymore. In fact, if the transition radiation is coherently radiated, the profiles are dominated by interference effects and thus useless for beam profiling [WS11]. Investigations are underway to overcome the problems of COTR for beam diagnostics by using transition radiation at much shorter wavelength in the VUV and XUV spectral region [LSKP+11].

5.2.2 Fluorescence Screens

As already discussed in the previous section, fluorescence screens are useful to convert energy from ionizing particles into visible light. Contrary to XUV photons, high energy electrons have a much longer penetration depth. Therefore, they will travel almost unaffected through a thin crystal leaving a florescence light channel which can be imaged by a camera. Depending on the geometry and the thickness of the crystal, this limits the resolution and could lead to a systematic offset of the beam distribution. For high-brightness electron beams, saturation of the light yield from a scintillator crystal was observed [MRBZ+01], making this screen useless for measuring the exact beam profiles. On top of that, the fluorescence screen can also emit coherent transition radiation, as discussed before, which would make a measurement of the fluorescence more difficult [YBG+11].

5.2.3 Wire Scanners

Since many years, wire scanners have been a standard diagnostic tool for all kinds of particle beams in circular and linear accelerators [Min04]. By moving a thin wire through the particle beam and detecting scattered particles or radiation, projections of the transverse beam profile can be measured. The advantage over screen methods is that wire scanners are almost non-destructive. The resolution of the wire scanner is limited by the thickness of the wire and the detector geometry to typically a few μm. For electron machines, secondary particles are usually detected with scintillators and PMT. The signal strength is assumed to be proportional to the number of scattered particles. Typical wire diameters are of the order of a few, up to several tens of micrometers. The wire material is often carbon or tungsten due to the good thermal and mechanical properties of these elements [Frö06].

5.2.4 Beam Position Monitors

The, maybe, most important diagnostic tools for charged particle accelerators are beam position monitors (BPM), which measure the centroid of the charge distribution of individual bunches. Since it is possible to build these devices in a fully non-invasive way, they are extensively used in circular and linear accelerators. The signal pickup is done by an arrangement of electromagnetic antennas or by a resonant device. A general overview of BPM technology can be found in [Wen11].

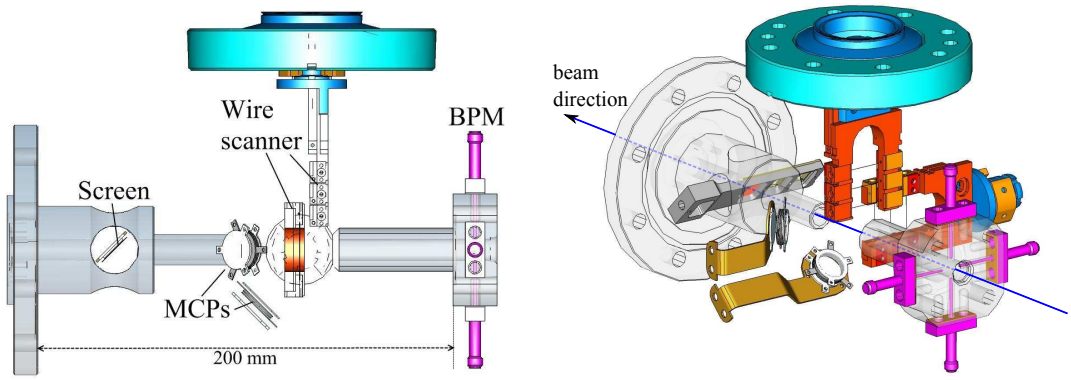

(a) Side view. Beam direction is right to left.

(b) 3D model view.

Figure 5.1: *Layout of the undulator diagnostic unit for sFLASH. In beam direction, it contains of a button type beam position monitor (BPM), a horizontal and a vertical wire scanner, and a set of three screens (aluminum-coated silicon, Ce:YAG, aluminum) on a movable frame. Each wire scanner folk is equipped with three wires; tungsten with 50 µm and 10 µm diameter, and carbon with 10 µm diameter. Each unit contains two MCPs for detection of photoelectrons. Such a unit is located in front of each sFLASH undulator module.*

5.3 sFLASH XUV and Electron Beam Monitors

Photon Diagnostics

For sFLASH, compact diagnostic units were build combining different types of measurement techniques. The first XUV beam profile monitor is placed about eight meters from the HHG source directly where the XUV beam enters the accelerator tunnel (*7HHGBL* in Fig. 5.2). A 30x40 mm^2 Ce:YAG screen with a thickness of 100 µm can be moved at 45 ° into the beam axis. The fluorescence is observed at 90 ° with respect to the beam axis. A lens of 50 mm focal length images the screen on a one-megapixel EMCCD[1] camera giving a resolution of 36.35 µm/pixel. In order to protect the CCD against the high-power NIR radiation of the laser beam from the HHG source and to make measurements of the fluorescence possible two bandpass filters (BG39[2]) are placed in front of the lens. One filter can be remotely moved out giving the possibility to measure also the NIR beam. This beam monitor is used for initial alignment of the XUV beam to the injection beamline before starting the transverse overlap adjustment. It also gives the possibility to measure the XUV beam size, however at this location the beam contains a wide range of photon wavelengths. Therefore, the measured beam size does not reflect the 21st harmonic of the

[1] EMCCD: electron-multiplying charge-coupled device

[2] each filter attenuates the NIR light by 5 orders. Transmission data can be found in [Sch]

HHG beam but also all the neighboring harmonics. To block wavelength below 80 nm, a thin aluminum foil (thickness 200 nm) can be inserted in front of the screen. Note, that also the 21st harmonic will be attenuated by about 50 % (see Appendix B).
Three XUV beam profile monitors using Ce:YAG screens are placed in front of the undulator modules (*1SFUND1*, *1SFUND2*, *1SFUND3* in Fig. 5.2). The setup is similar to the one described above. Here, the screen size is 10x14 mm^2. The imaging optics contains an aspherical lens[3] ($f_{\text{nominal}} = 80\,\text{mm}$) and one objective lens[4] ($f = 75\,\text{mm}$) resulting in a magnification of $m = 0.94$. The resolution of the setup is limited by the thickness $d = 100\,\mu\text{m}$ of the crystal and the acceptance angle $\theta_c = 30\,^\circ$ of the imaging optics. Using the relation [MRBZ+00]

$$\sigma_f \approx \frac{d}{n} \cdot \tan\left(\frac{\theta_c}{2}\right) \tag{5.1}$$

the resolution is 14.6 μm. In addition to the screens, the units *1SFUND1*, *1SFUND2* are equipped with horizontal and vertical wire scanners and two MCPs[5]. The scanner mechanics and electronics were originally designed for the FLASH undulator system [HBC+08] (Zeuthen Type). For each scanner, three different wires can be selected: Tungsten with a diameter of 50 μm, 10 μm, or carbon with 10 μm wire diameter. The MCPs are used to detect photoelectrons emitted by the wire, while the wire is crossing the XUV beam. With that, the horizontal and vertical projection of the XUV beam profiles can be measured. A technical layout of the geometry is given in Fig. 5.1. New detection schemes and geometries for the XUV beam detection are under study by Eugen Hass [Has11] in order to optimize the detection geometry of the MCP detectors. The goal is to reduce to signal produced by the electron beam while the signal from the XUV beam is maximized. In this case, an XUV beam profile measurements would be possible without disturbing the electron beam operation.

Electron Diagnostics

The electron beam profile and position can be measured at various locations along the seeding section, as illustrated in Fig. 5.2, using two types of beam position monitors (button type and stripline type), silicon screens producing optical transition radiation, and wire scanners. The specifications for all these monitors are slightly different. Table 5.1 lists the parameters for each station [NW04][HBF+03]. For emittance measurements, a total number of eight screens stations are available equipped with different types of screens and optics [Ack11].

[3] Zörk Macroscope Type 1 (MCS/1)
[4] Pentax Model B7514C
[5] Hamamatsu F4655-1 [Ham]

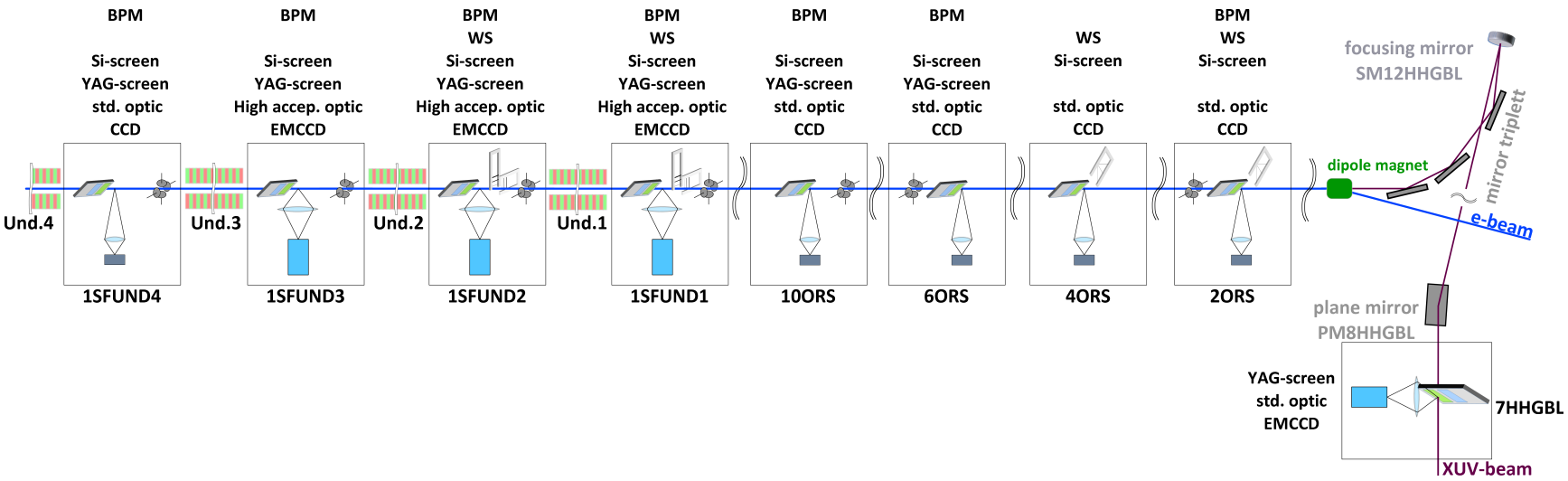

Figure 5.2: *Schematic of injection beamline diagnostics. Beam direction is from right to left. The XUV beam enters the accelerator tunnel at the position 7HHGBL, where the transverse profile can be measured on a Ce:YAG screen. Reflected coaxially to the electron beam line, it is combined with the electron beam at the last dipole magnet of the energy collimator. Eight diagnostic stations (names according to the FLASH nomenclature; e.g. 6ORS: station located 6 m after the beginning of section ORS) along the beam pipe give the possibility to measure transverse electron and XUV beam properties.*

The wire scanners are read out using the beam loss monitor system for the sFLASH undulator [KKM+11] which uses a scintillator-based detection scheme for the created secondary particles. The signal of the PMT is assumed to be proportional to the beam intensity intercepted by the wire.

	Screen stations			Wire scanner	BPM
	screen types	**Optics**	**Filters**		
2ORS	polished Si and	three magnifications:	three filters:	MDI type	strip line
4ORS	Ag-coated Si	1; 0.38; 0.25	40 %; 25 %; 10 %	MDI type	none
6ORS	YAG:Ce crystal	two magnifications:	five filters:	none	strip line
10ORS	Ag-coated Si	0.15; 0.65	BG39; 50 %; 10 %;	none	strip line
			1 %; 0,01 %		
1SFUND1			five filters:	Zeuthen type	strip line
1SFUND2	YAG:Ce crystal	one magnification:	BG39; 50 %; 10 %;	Zeuthen type	button
1SFUND3	Ag-coated Si	0.94	1 %; 0.01 %	none	button
1SFUND4				none	button

Table 5.1: *Available hardware for electron beam size and position monitoring in the seeding section of FLASH. The screen stations are equipped with different type of screen. The optics to image the screen on the CCD allows to select different magnifications and different filters. For the stations 2ORS and 4ORS, eight different filter combinations can be chosen with the three transmission filters (transmission in %). For all other stations only one filter can be used at a time. Two types of wire scanners are in use. The Zeuthen type has two individual wire folks in horizontal and vertical direction. The MDI type has only one folk mounted at* 45 ° *which contains three wires to measure horizontal, vertical projections and the projection under* 45 °.

6 Measurements

6.1 XUV Beam Characterization

As discussed in Chapter 3, the tolerances for the focusing and the transverse alignment of the XUV beam are crucial for the seeding project. Therefore, a detailed characterization of the seed beam properties is necessary. In addition to the XUV beam characterization in the HHG laboratory, the transverse beam properties are studied using the diagnostics installed in the injection beamline. Measurements of the beam divergence stability, pointing stability, intensity stability, and beam quality are shown in the following sections.

6.1.1 Technical Details of the Measurement

Different measurements of the XUV beam were performed with and without the aluminum foil in the injection beamline. It was observed that the beam intensity decreases significantly when the aluminum foil is inserted, since wavelengths above 80 nm are efficiently blocked. The remaining harmonic content is reduced by a factor of about two (see transmission curve in Appendix B). For investigations of the beam size, the foil was always inserted. To determine the beam center position or to measure the transverse beam stability, the foil was removed. The electron beam was switched off and the dark current was dumped in the FLASH energy collimator by reducing the field gradients of the last accelerating modules. This was necessary because the electron beam and even the dark current from the accelerator produces too much background signal on the Ce:YAG screen. To suppress the signal of the NIR laser, two bandpass filters (BG39 [Sch]) were inserted in front of the CCD chip.

6.1.2 Data Acquisition, Image Processing, and Analysis Algorithm

For each beam profile measurement, the camera settings were adjusted in order to get a sufficient signal-to-noise ratio. Usually, the camera gain was set to maximum and the vertical and horizontal pixel binning was set to 2x2. The exposure time was increased until the beam was clearly observable on the camera image. Typically, the values varied from a few hundred milliseconds to several seconds, depending on the beam size on the screen. Figure 6.1(a) shows a typical raw image of the beam profile. By closing the gas nozzle of the HHG target, the XUV beam was switched off and a series of background pictures were taken. After switching the XUV beam on, typically ten consecutive images were saved. Each image was processed and analyzed in the following way:

1. subtract background
2. apply median filter to suppress hot pixels
3. identify signal region of interest
4. set region of noise[1] to zero
5. apply a 2-dimensional Gaussian fit to estimate beam tilt angle
6. rotate image by beam tilt angle
7. calculate rms beam width

Figure 6.1 exemplarily shows the image processing algorithm for one beam profile.

[1] inverse of the region of interest

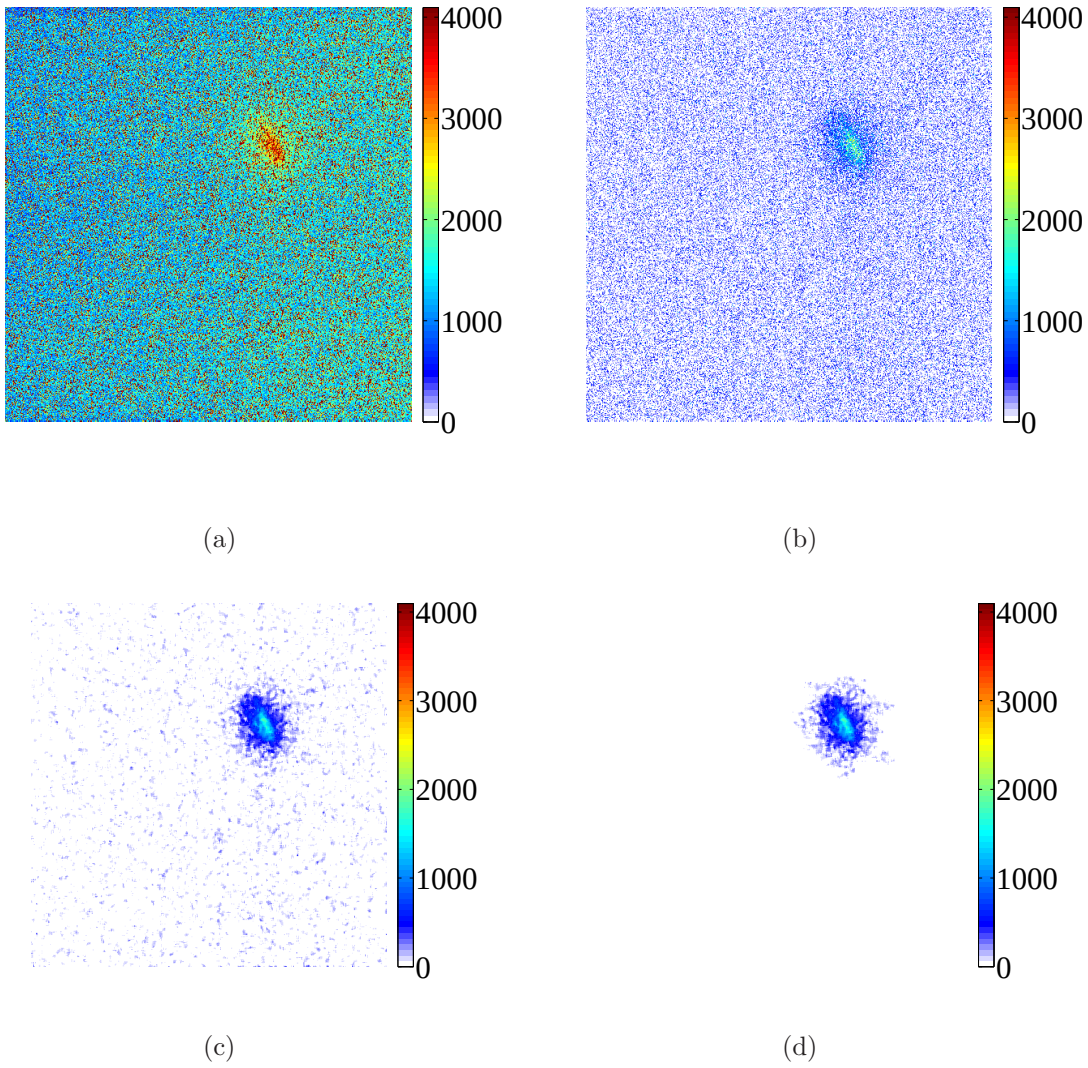

Figure 6.1: *Example of the image processing algorithm to extract the beam information from the raw data: (a) raw image; (b) mean background image subtracted; (c) image after applying a median filter [5x5]; and, (d) final image after determination of the region of interest.*

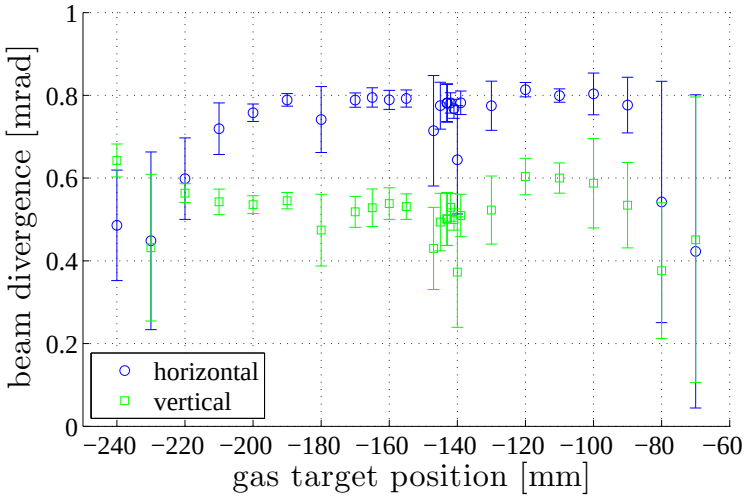

Figure 6.2: *Divergence of XUV beam measured for different gas target positions of the HHG source relative to the NIR laser focus.*

6.1.3 Beam Divergence

During the commissioning of the HHG source, several parameter scans were performed to optimize the XUV source characteristics. One important parameter is the position of the gas target relative to the longitudinal focus position of the NIR drive laser [SLAL97, SDP+96]. For the scan, the XUV beam size was measured on the screen *7HHGBL* and at the diagnostic section in the laser laboratory. The beam intensity was additionally measured at the energy monitor of the FEL diagnostic station (see Section 2.4). Figure 6.2 shows the measured divergence as a function of the gas target position. The NIR laser focus was located at $z = -140\,\text{mm}$ with a Rayleigh length of $z_{R,x} = (105 \pm 4)\,\text{mm}$ and $z_{R,y} = (73 \pm 5)\,\text{mm}$ [Mit11]. Six corresponding profiles are shown in Fig. 6.3. It can be seen that the beam shape changes for different target positions from a nearly round beam at $z = -220\text{mm}$ to an elliptical beam at positions $z > -200\,\text{mm}$. The independent measurement in the HHG diagnostics section of the laser laboratory gives an upper limit[2] of the divergence along the narrow and the wide semi-axis for the 21st harmonic of $\theta_{\text{narrow}} < (0.56 \pm 0.01)\,\text{mrad}$ and $\theta_{\text{wide}} < (0.84 \pm 0.03)\,\text{mrad}$, respectively [Mit11]. This is consistent with the measurements shown here. The maximum pulse energy of the 21st harmonic was measured at the position $z = (195 \pm 10)\,\text{mm}$. For seeding, the HHG source was optimized by measuring the energy of the 21st harmonic on the spectrometer in the HHG diagnostic branch [Mit11]. For this HHG target configuration, the optimum z-position of the target was found to be at $z = (210 \pm 5)\,\text{mm}$.

[2]The exact value is unknown, because the curvature of the mirrors which reflects the HHG beam into the diagnostic branch of the laboratory was unknown. For details see [Mit11]

6.1.4 Beam Stability

The shot-to-shot angular stability of the XUV beam was measured at the screen monitor *7HHGBL* without aluminum foil[3] after the HHG source was optimized for seeding operation. For that, 2000 consecutive laser beam profiles were recorded and analyzed. The centroid of each profile was determined. The results are plotted in Fig. 6.4 showing the distribution of the centroids for each profile in a histogram with a bin size of 0.1 mm. Taking the projections along the indicated coordinate system (ξ/η), one can obtain the width of the distribution. Together with the distance d from the source point to the screen the angular beam stability can be determined to be

$$\Delta\theta_\eta = (17.3 \pm 0.2)\,\mu\text{rad} \qquad \text{and}$$
$$\Delta\theta_\xi = (76.9 \pm 0.9)\,\mu\text{rad}.$$

The same data was used to estimate the beam divergence stability. Again, one has to point out that the profiles contain all wavelengths of the HHG spectrum. Thus, the value of the divergence, as determined here, cannot be used as a characteristic number for the seed beam. Figure 6.5 shows histograms of the determined beam width in x- and y-direction. The resulting beam divergences are

$$\theta_x = (0.445 \pm 0.006)\,\text{mrad}\,(\text{rms}) \qquad \text{and}$$
$$\theta_y = (0.490 \pm 0.022)\,\text{mrad}\,(\text{rms}).$$

[3]Without aluminum foil the CCD exposure time could be set to the minimum value of 75 μs to measure single-shot profiles.

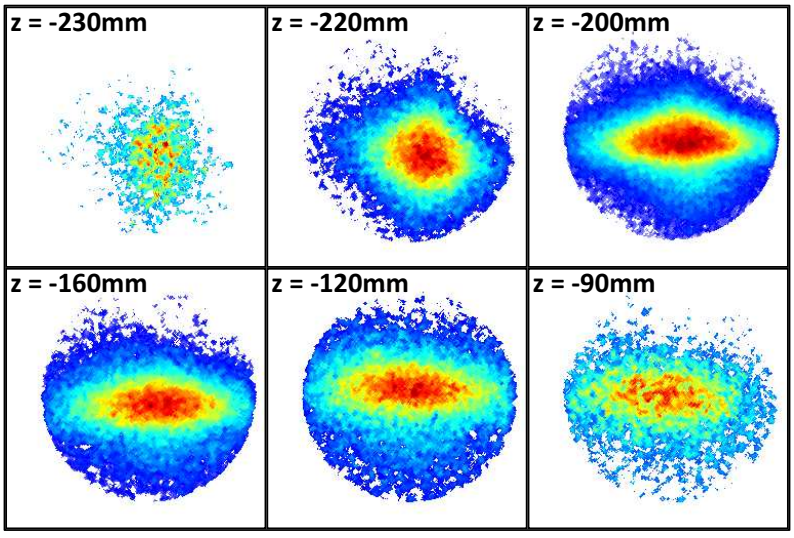

Figure 6.3: *Measured beam profiles for different z-positions of the gas target. The laser focus was at $z = -140\,mm$.*

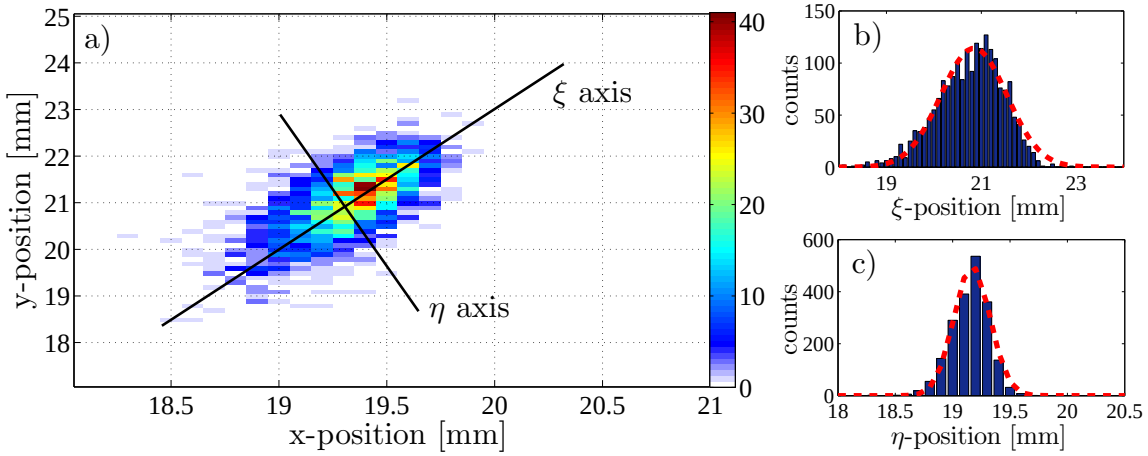

Figure 6.4: *Beam jitter analysis. a) shows a two dimensional histogram of the centers of 2000 single shot beam profiles. In b) and c) the projection along the indicated axis ξ and η are plotted.*

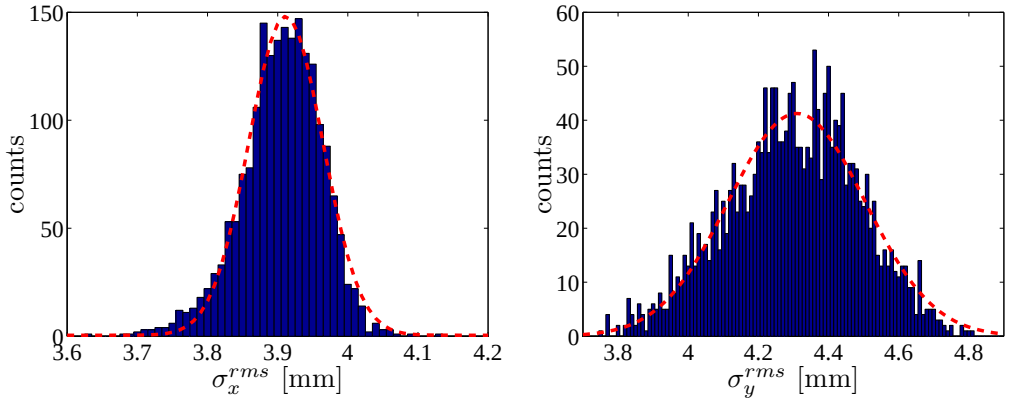

Figure 6.5: *Histograms of the rms beam width in x- and y-direction.*

The relative intensity stability of the HHG output beam was measured by integrating over all pixel values of the CCD. This measurement was done without aluminum filter, such that all harmonic orders are measured. The results for two measurement periods are plotted in Fig. 6.6. The stability of the HHG source during that time was about (40±5) % (rms), which can be related to a larger fluctuations of the NIR pulse energy of about 10 % (rms). Under optimum conditions (5 % (rms) NIR pulse energy stability) the intensity fluctuation of the 21st harmonic was about 25 % (rms) [Mit11].

Discussion

The measurements of the transverse beam stability show that the shot-to-shot pointing jitter for the narrow and wide semi-axis of the beam is about 4 % and 15 % of the rms beam divergence, respectively. For those measurements which integrate over tens to hundreds of shots, this will lead to an apparent broadening of all beam profiles which are measured

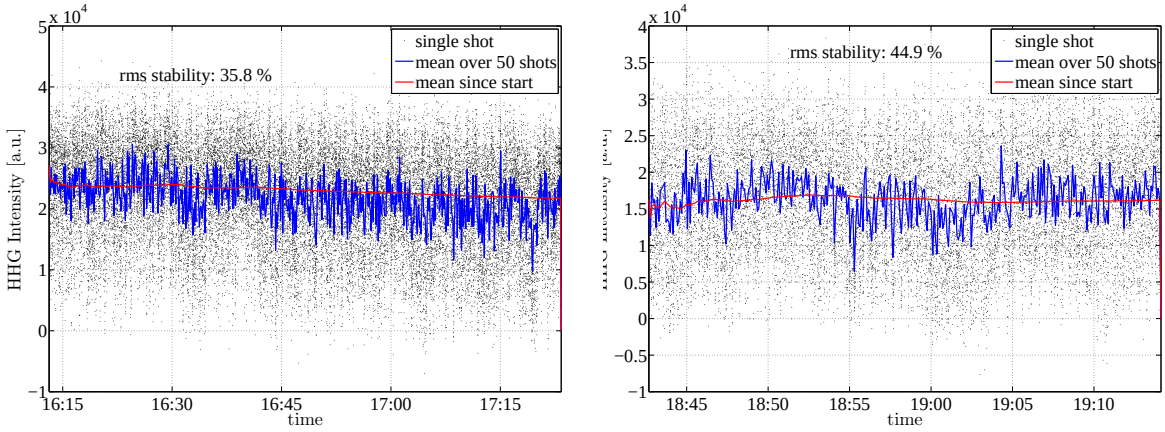

(a) Measurement at 11.04.2011 over about one hour (b) Measurement at 11.04.2011 over half an hour

Figure 6.6: *Relative HHG output stability measured with the screen station* 7HHGBL.

in the near-field. Therefore, one can expect a systematical error for the width of the measured beam profiles. In addition, the pointing jitter will cause a degradation of the efficiency for the seeding process. This will be discussed in the following Chapter.

6.1.5 Beam Focus Characterization

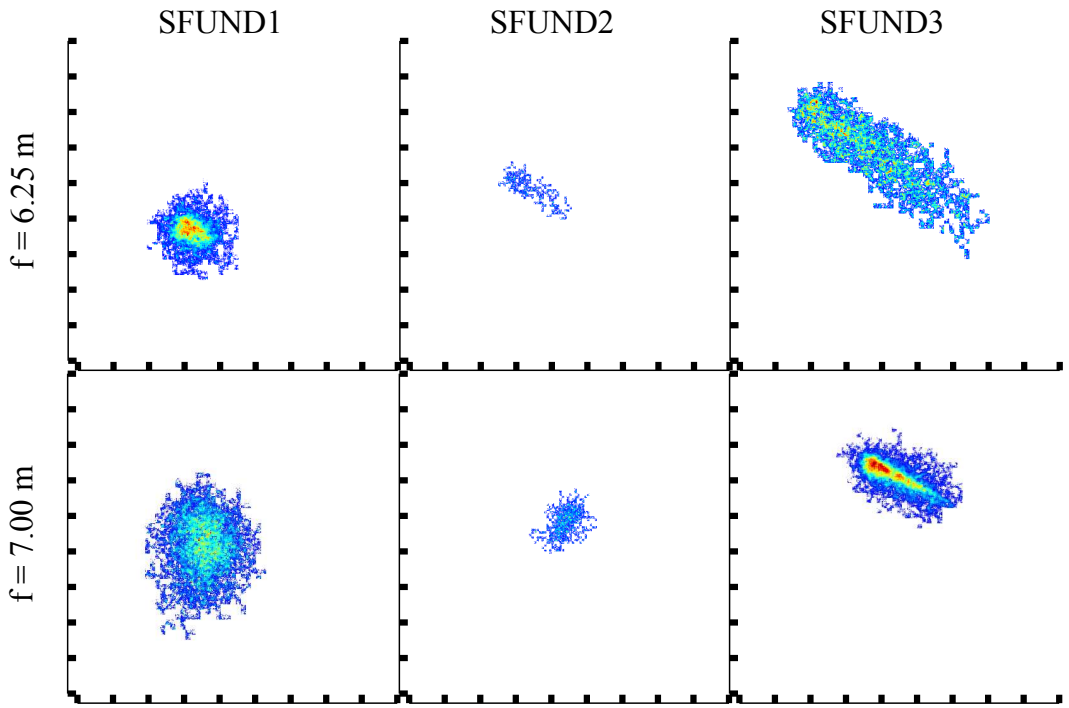

Figure 6.7: *Measured beam profiles at different screen locations for two different focal lengths.*

In order to determine the longitudinal focus position of the XUV beam along the sFLASH undulator system, as well as the size of the beam waist, transverse beam profiles were measured at the diagnostic units *7HHGBL*, *1SFUND1*, *1SFUND2*, and *1SFUND3* using the Ce:YAG screens. For two focal lengths in the injection beamline, the profiles were measured and analyzed[4]. Figure 6.7 shows the processed beam profiles at the different measurement locations for both focal lengths. The integration time varied between 0.3 and 8 s depending on the beam size.

The size of the beam waist and the longitudinal waist position is calculated by fitting a global Gaussian beam model $w(z, f)$ to the data, as discussed in Appendix C.3. Free parameters in the model are the waist size w_0, waist location z_w and beam quality factor M^2. The fits are applied separately for the two orthogonal axis of the beam profiles. It turns out that for fixed focal length in the model of $f_1 = 6.25\,\mathrm{m}$ and $f_2 = 7.00\,\mathrm{m}$, respectively, the error in each parameter is larger the 100 % or the parameter values are unphysical. Therefore, the focal length is, in a first step, fitted separately for each data set. Table 6.1 gives the results for the fitted focal lengths, which significantly differ from the nominal values by up to 13%. The values are larger than the nominal values, expect for f_y^{long}, which is within the errors close to the specified value. The reason for

[4]The third focal length of $f_3 = 8.5\,\mathrm{m}$ could not be used for this study, since the signal of the XUV beam with inserted aluminum filter was too low for reliable measurements.

this differences has to be studied in detail. Most likely, the mirror mount of the focusing mirrors (see Fig. E.4 in Appendix E) changes the mirror surface due to mechanical stress. This hypothesis will be tested, as soon as the mirror mount can be dismounted during the next shutdown (see Chapter 8). Using the fitted focal length and applying again the

	measured [m]	**nominal [m]**
f_x^{short}	7.06 ± 0.10	6.25 ± 0.06
f_y^{short}	6.70 ± 0.06	6.25 ± 0.06
f_x^{long}	7.82 ± 0.02	7.00 ± 0.07
f_y^{long}	7.16 ± 0.15	7.00 ± 0.07

Table 6.1: *Estimated focal lengths in sFLASH injection beamline.*

global Gaussian beam model to the data, the beam parameters can be extracted from the fit. Figure 6.8 shows the data of each focal length together with the fitted global Gaussian model. Table 6.2 lists the results for the beam waist and position, as well as the beam quality factor for each beam axis. For the mirror with short focal length, the longitudinal position of the horizontal (x) beam waist is located at the entrance of the undulator and for the vertical (y) beam waist 35 cm after the center of the first undulator module. The Rayleigh lengths of the beam are

$$z_R^x = (1.06 \pm 0.57)\,\text{m} \qquad \text{and}$$
$$z_R^y = (0.84 \pm 0.51)\,\text{m}.$$

	w_0^x [μm]	z_w^x [m]	M_x^2	w_0^y [μm]	z_w^y [m]	M_y^2
f_x^{short}	409±98	0.24±0.28	13.1±3.1			
f_y^{short}				651±187	-1.23±0.21	41.9±8.1
f_x^{long}	524±125	4.63±0.45	13.1±3.1			
f_y^{long}				755±216	1.06±0.29	41.9±8.1

Table 6.2: *Results of XUV beam parameter determination. w_0^x and w_0^y are the beam waist sizes of the narrow and wide semi-axis of the beam profiles. z_w^x and z_w^y are the longitudinal distances of the beam waist with respect to the center of the first undulator module (positive values in beam propagation direction).*

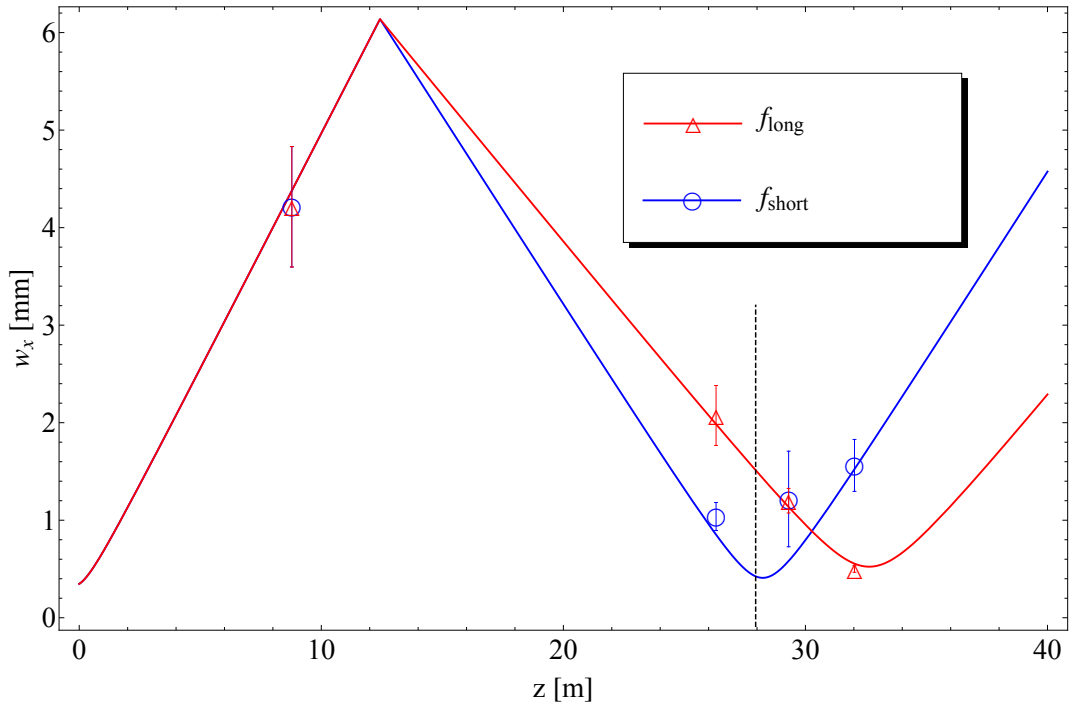

(a) horizontal data

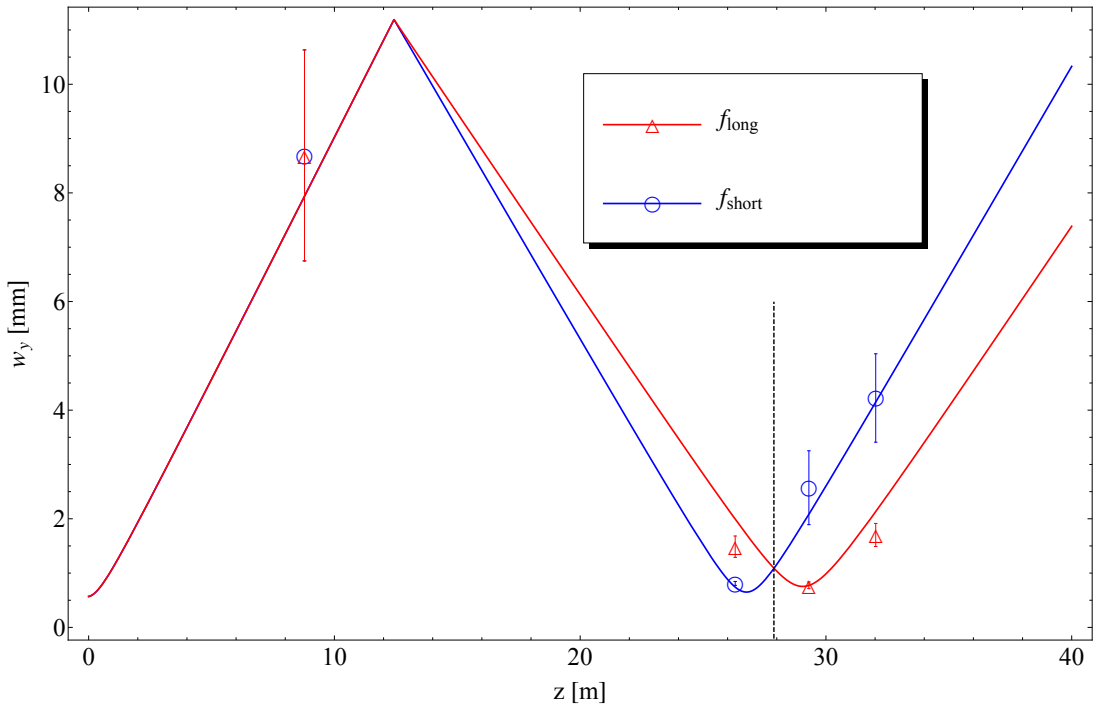

(b) vertical data

Figure 6.8: *Measured XUV beam sizes along the sFLASH injection beamline into the undulator. The solid lines show the fitted global Gaussian model for each focal length (open cycles f_{short}, open triangles f_{long}). The dashed line indicates the center of the first undulator module.*

Discussion

The results of the beam focus characterization reveal that the XUV beam shows astigmatism and asymmetries in divergence and beam waist (see Appendix C.2). The reason for such asymmetries could either be the initial beam parameters at the HHG target or changes of the beam in the transport system. The transverse beam properties of the HHG source were supposed to be measured in the HHG diagnostic branch. A wavefront measurement [Hip11] and a beam focus characterization were done [Mit11]. Problematic with the interpretation of the results are unknown changes of the beam due to mirror deformations of the extraction beamline to the diagnostic branch (for details see[Mit11]). Therefore, the source parameters could not be measured with an adequate accuracy and consequently the source for the measured beam asymmetries in the undulator is difficult to identify. If the measured parameters are back-propagated to the target position at $z = 0\,\mathrm{m}$, the following beam waist parameters are obtained:

$$
\begin{aligned}
w^{x}_{0\,\mathrm{Source}} &= (327 \pm 80)\,\mu\mathrm{m} \\
w^{y}_{0\,\mathrm{Source}} &= (566 \pm 168)\,\mu\mathrm{m} \\
z^{x}_{w\,\mathrm{Source}} &= (-239 \pm 184)\,\mathrm{mm} \\
z^{y}_{w\,\mathrm{Source}} &= (-66 \pm 165)\,\mathrm{mm}.
\end{aligned}
$$

Compared to the values of the NIR laser beam waist ($w^{x}_{0\,\mathrm{NIR}} = (173 \pm 2)\,\mu\mathrm{m}$ and $w^{y}_{0\,\mathrm{NIR}} = (186 \pm 4)\,\mu\mathrm{m}$ [Mit11]) the calculated beam sizes at the target are unphysical even under consideration of the errors, since the HHG beam cannot exceed the beam size of the NIR laser beam. It is most likely that the beam quality parameter M^2 significantly increases during the propagation caused by an imperfect surface flatness of the mirrors or by aberration or diffraction at apertures. For example, an increase of M^2 by a factor of three or four would immediately change the estimated beam sizes at the target position to physically possible values. If the estimated values $w_{0\,\mathrm{Source}}$ are scaled with the measured values of the NIR laser $w_{0\,\mathrm{NIR}}$, a lower limit for the increase of the M^2 for each beam axis can be calculated to 1.9 and 3.1, respectively.

The absolute values of the calculated beam waist sizes at the undulator are at least a factor of three larger than the electron beam size. On the one hand, this relaxes the relative positioning of both beams for the transverse overlap. On the other hand, the coupling for the seeding process is rather ineffective. The following discussion estimates the expected contrast between the seed pulse and the shot noise of the electron beam.

For the measured beam size and pulse energy one can estimate the peak electric field strength of the seed beam. Assuming a Gaussian shape in transverse and longitudinal

dimensions, the peak electric field is given by

$$\hat{E} = 2\sqrt{\frac{0.94 \cdot \mathcal{E}}{c\,\epsilon_0\,\pi\,w_0^x\,w_0^y\,\tau}}$$

where $\mathcal{E}$ is the pulse energy and τ the FWHM of the pulse duration. The factor 0.94 arise from the assumption of a Gaussian pulse shape. The pulse energy of the 21st harmonic at the HHG source was measured with different detectors and at different locations. The values range from 0.23 nJ to about 15 nJ. The difficulty for an absolute pulse energy measurement of a single harmonic is that the HHG beam contains a range of harmonics which are differently reflected by the mirrors to the spectrometer. Therefore, one has to make assumptions on the energy distribution for the harmonic content of the beam. For details of the measurements see [Mit11]. The pulse duration of the HHG beam was not measured. Direct measurements at other HHG sources have shown that the HHG pulse duration is slightly below the duration of the drive laser [SFK+11]. Theoretical predictions and numerical studies of HHG [SLAL97] estimate the pulse durations of the harmonics to be about a factor of two shorter than for the NIR drive laser which was measured to be $\tau_{\mathrm{NIR}} = (32.9 \pm 0.2)\,\mathrm{fs}$ (FWHM). For this discussion a ratio of two between NIR and XUV pulse duration is assumed. Taking the theoretical transmission of the injection beamline of 20 % (see Fig. 4.6) into account the peak electric field strength ranges from 2.2 to 18.0 MV/m.

In Chapter 3, the equivalent electric field due to shot noise of the electron beam was calculated to be 3.2 MV/m. In the best case, one exceeds the shot noise level of the FEL by a factor of 5.6 which should be observable in the FEL spectrum. In the worst case, it is questionable if an increase of the spectral intensity could be detected. In this case, a more detailed analysis of the spectra need to be done. For example, one could search for a reproducible spike in the spectrum of which spectral width is comparable with the bandwidth of the 21st harmonic of the HHG source. The reproducibility of such peaks would be impaired by the different jitter sources for seeding, namely the intensity jitter of the source, the arrival time jitter of seed pulse with respect to the electrons, and the transverse overlap jitter. A discussion of the stability for seeding is given in chapter 7.

6.2 Transverse Overlap Measurements

The strategy to set up the transverse laser-electron overlap is to use the optical laser beam axis as a reference orbit. After the undulator and the undulator vacuum chamber were aligned by the DESY survey group [5], an optical alignment laser beam was centered at the vacuum chamber. The beam position at each diagnostic station between the undulator modules was measured and saved as a reference position. Afterwards, the electron beam orbit was adjusted to these reference positions. While the variable-gap undulators are set to the nominal K-value for the spectral overlap, the electron beam orbit is stabilized by the slow orbit feedback of the machine [Pra09]. The positions of the XUV beam and the electron beam in front and after the first undulator module (stations *SFUND1* and *SFUND2*) are both measured with the scintillator screens. With that, a systematic offset due to possible displacements of the different screen (OTR and Ce:YAG) positions can be excluded. In addition, the OTR screens show fluctuating COTR signals when the electron beam is optimized for lasing conditions. In this case, a determination of the beam center position is practically impossible. Figure 6.9 shows a sequence of OTR-screen- and Ce:YAG-screen-measurements at station *SFUND1*. The shot-to-shot COTR fluctuations due to a microbunching instability [WS11] are clearly visible.

Figure 6.10 shows the profiles of both beams and at both screen stations as a super-

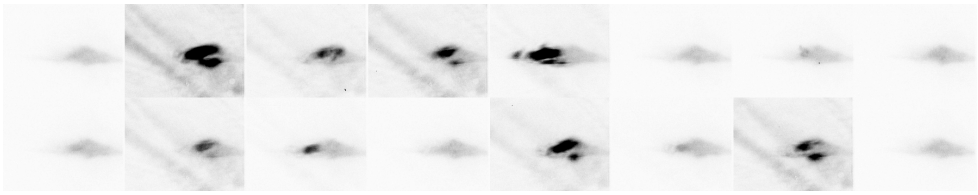

(a)

(b)

Figure 6.9: *Sequence of successive electron beam profiles produced by an OTR screen (a) and by a Ce:YAG screen (b) at station SFUND1. The beam compression was optimized for seeding conditions.*

[5] The alignment was done, such that the field of the undulator and the center of the vacuum chamber coincide with each other.

position. Projections of the electron- and XUV-beam-profiles in horizontal and vertical direction are plotted in Fig. 6.11. Qualitatively the profiles overlap very well. In order to quantify the overlap, one has to choose an appropriate method to define respective centers of the beam profiles. Either one takes the centroid x_0 of the distribution, the maximum position of the projection (Max), the maximum of the two-dimensional profile ($\mathrm{Max_{2D}}$), or the mean value μ_{Gauss} of a Gaussian fit. Other definitions for the beam center might be possible, but are not considered here. Table 6.3 lists the beam position and the offset between both beams for each of these methods. During the optimization procedure for the transverse overlap, the mean value of the Gaussian fit was used as a measure for the beam center. With these values, the position- and angle-offsets of both beams at the center of the undulator can be calculated to be:

$$\begin{aligned}
\Delta x_c &= (0 \pm 24)\,\mu\mathrm{m} \\
\Delta y_c &= (86 \pm 35)\,\mu\mathrm{m} \\
\Delta x_c' &= (25 \pm 16)\,\mu\mathrm{rad} \\
\Delta y_c' &= (35 \pm 23)\,\mu\mathrm{rad}.
\end{aligned}$$

The results show that the transverse laser-electron overlap (with the chosen definition for the beam center) could be adjusted close to the defined tolerance values for angle and position. Due to the fact that the beam width of the seed beam was three times larger than expected, it was decided to stop the optimization procedure of the transverse overlap at that point. Since no clear signal for seeding could be detected, it can not be guaranteed that the determination of the beam center using a Gaussian fit is appropriate.

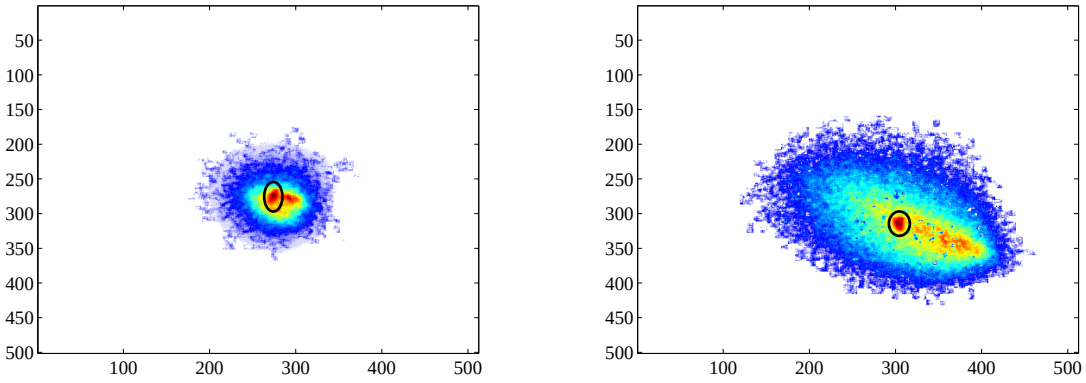

(a) SFUND1 (b) SFUND2

Figure 6.10: *Superimposed beam profiles of XUV and electron beam after adjusting the transverse overlap. The black mask indicates the position of the electron beam. Scaling in CCD pixel.*

	SFUND1		SFUND2	
	x	y	x	y
$\mu^{\mathrm{el}}_{\mathrm{Gauss}}$	344±17	610±4	-672±15	485±4
$\mu^{\mathrm{HH}}_{\mathrm{Gauss}}$	382±19	644±8	-710±38	623±70
$\Delta_{x,y}$	38±25	34±9	-38±41	138±70
$\mathrm{Max}^{\mathrm{el}}$	311±44	570±7	-745±37	525±18
$\mathrm{Max}^{\mathrm{HH}}$	301±41	604±73	-398±129	692±171
$\Delta_{x,y}$	-10±60	34±73	347±134	167±172
$\mathrm{Max}^{\mathrm{el}}_{\mathrm{2D}}$	219±15	571±11	-715±54	512±12
$\mathrm{Max}^{\mathrm{HH}}_{\mathrm{2D}}$	237±36	633±130	-230±57	1547±194
$\Delta_{x,y}$	18±39	62±130	485±79	1037±194
x^{el}_0	279±3	587±16	-973±3	764±11
x^{HH}_0	303±2	637±9	-849±62	605±32
$\Delta_{x,y}$	24±4	50±18	124±62	-159±34

Table 6.3: *Horizontal and vertical beam position of XUV and electron beam in μm at diagnostic station* SFUND1 *and* SFUND2 *for different determination methods. μ_{Gauss}: mean value of Gaussian fit. Max: Maximum of the projected beam profile. Max_{2D}: Maximum of the beam profile. x_0: centroid of the projected beam profile.*

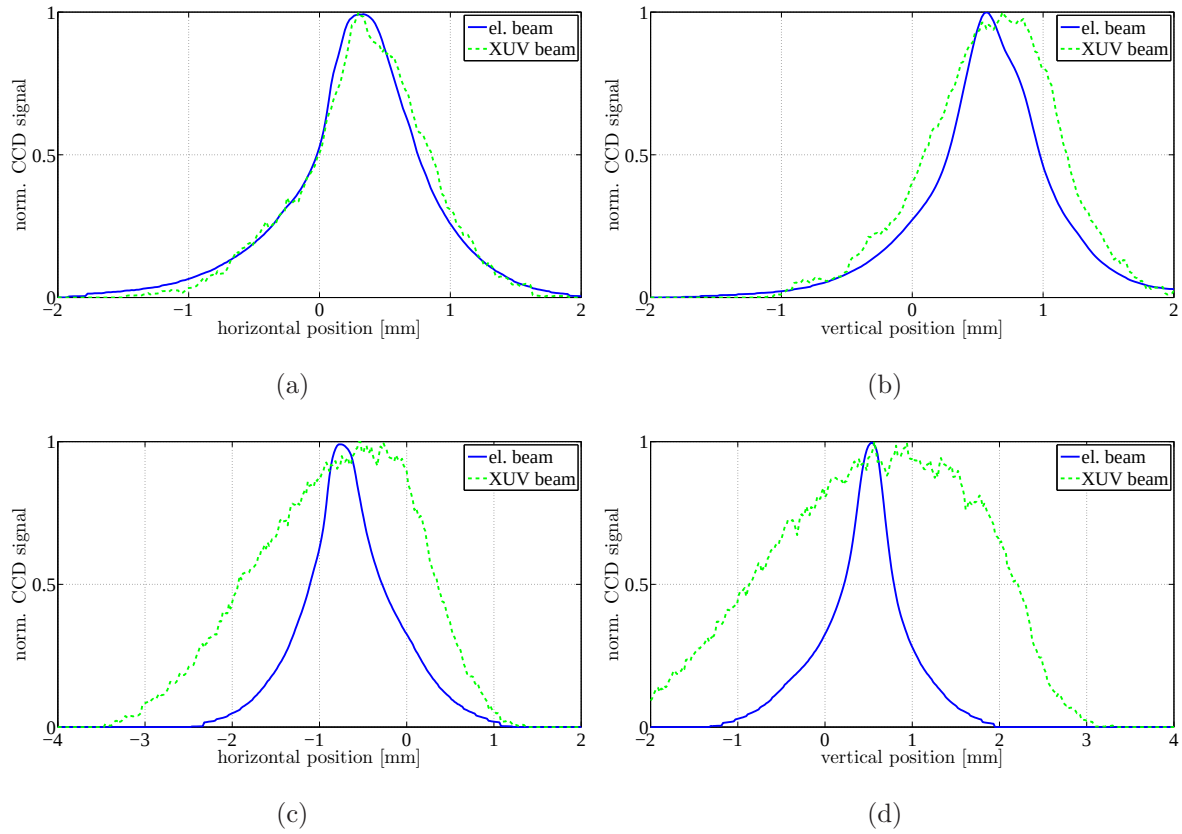

Figure 6.11: *Projections of beam profiles of electron and XUV beam measured at station: (a) SFUND1 horizontal; (b) SFUND1 vertical; (c) SFUND2 horizontal; and, (d) SFUND2 vertical.*

7 Seeding Diagnostics

The measurements of the transverse overlap and the focusing of the seed laser (see Chapter 6.1.5) showed that the maximum signal-to-noise ratio for the seeding process can be expected to be less than 6. Since the electron- and the XUV-beam-properties will vary along the longitudinal coordinate of the bunch, one can expect that the signal-to-noise ratio is also a function of the longitudinal position of the XUV pulse within the electron bunch. A detailed discussion on the impact of varying slice emittance or slice energy spread of the electron beam for the seeding process is given in [Tar11]. Under idealized conditions, the expected signal-to-noise ratio for the FEL pulse energies $\mathcal{E}$ is $\mathcal{E}_{seeded}/\mathcal{E}_{SASE}$ = 80 [MAB$^+$08a]. In this case, the spectral power of the seeded part of the FEL pulse would exceed the SASE noise by about three orders of magnitude. Such a signal could be easily detected by either an energy monitor or by analyzing the spectra. With the present XUV beam focusing, the signal-to-noise ratio will be reduced by at least two orders of magnitude in the spectral domain. This makes a detection of the seed signal by simply measuring the FEL pulse energy not applicable. More realistic is to identify the seed signal by spectrally resolving the FEL radiation. The identification has to be done in real-time in order to optimize the signal by tuning the transverse, the spectral, and the temporal overlap. This chapter describes the procedure of the data acquisition and the analysis of the data. A short discussion on the jitter problem for the laser-electron overlap is given in Appendix D because this has a major impact on the data acquisition time. For example, if the probability for the overlap is only in the per mille range due to large jitter in every dimension, the acquisition time for one time delay scan over a few ps would exceed one machine shift of eight hours.

7.1 Operating Procedure

Before starting the seeding experiment, the sFLASH FEL amplifier is set up using the SASE FEL mode. Starting with a standard machine setup for SASE in the FLASH main undulator, the accelerator parameters like accelerator RF settings, quadrupole currents,

electron-gun parameters etc. remain fixed. Only the electron beam orbit in the sFLASH undulator will be tuned in order to maximize the SASE output signal. The undulator gaps are initially set for resonance at 38.5 nm, based on the magnetic calibration of the undulators and the electron beam energy. By analyzing the statistics of the SASE pulse energy, the number of longitudinal laser modes M can be estimated according to the so-called gamma distribution

$$p_M(u) = \frac{M^M u^{M-1}}{\Gamma(M)} e^{-Mu} \tag{7.1}$$

where $u = \mathcal{E}_{bw}/\langle\mathcal{E}\rangle$ is the normalized pulse energy, $\langle\mathcal{E}\rangle$ the average energy over many FEL pulses, M the number of longitudinal modes, and Γ the gamma function. Figure 7.1 shows a typical distribution measured during sFLASH operation. The exact wavelength is adjusted later, after measuring the HHG spectrum at the FEL diagnostic spectrometer. Once the spectral overlap is established, the transverse electron beam position before and after the first undulator module is measured. The beam position of the seed-laser is adjusted using the mirrors of the injection beamline. Finally, the arrival times of the electron bunches and the laser pulses are measured using a streak camera with a precision of about 600 fs [Tar11]. The relative arrival time difference is adjusted by changing the delay of the trigger for the laser oscillator. The minimum step size for the electronic delay is 46 fs due to the limited resolution of the digital-to-analog converter of 14 bit.
To find the six-dimensional overlap, the time delay for the laser is slightly increased which separates both pulses in time by about 2 ps (enough, to clearly identify the pulses with the streak camera). Afterwards, the delay is increased in steps of 50 fs in order to scan the relative arrival time of laser pulses and electron bunches. At each time step, a series of FEL spectra is recorded. The full scan range is typically 4 to 6 ps. Using this scan procedure, a NIR laser-electron interaction in a short electromagnetic undulator could be demonstrated (for details see [Tar11]), which proves that the measurement of the relative arrival times does not show a systematic offset.

7.2 On-line Signal Detection

To identify the effect of the seeding in the FEL spectra, a series of tests is performed which analyze the statistic of the spectra on-line. These tests compare FEL spectra recorded during time delay scans with SASE spectra when the seed beam is switched off. Therefore, a data set of SASE spectra is recorded for reference (typically 2000 shots). A two-sided Kolmogorov-Smirnov test [SW09] compares the statistics of the FEL spectra with the one of the SASE spectra. If the overlap of seed laser and electron beam is established, a change of the FEL statistics can be expected. In terms of the statistical hypothesis

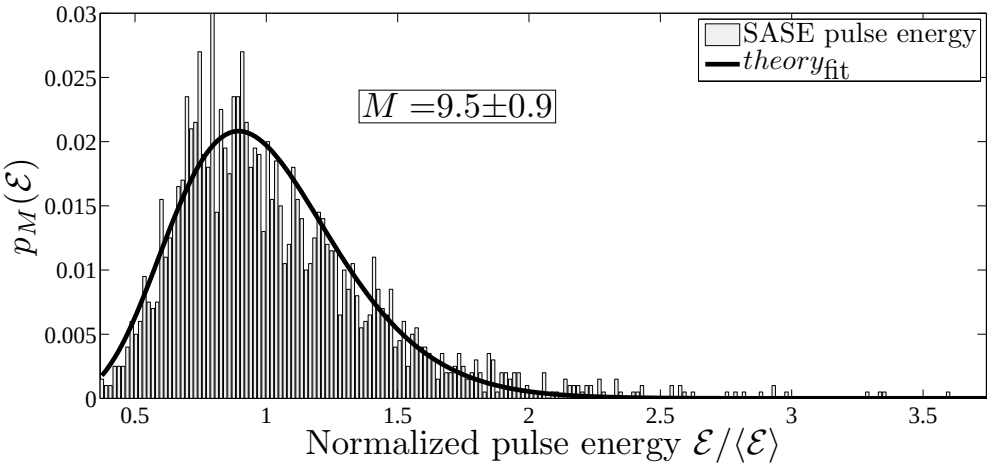

Figure 7.1: *SASE energy distribution of 2000 pulses recorded during a time delay scan for finding the laser-electron overlap. The theoretical gamma distribution is fitted to the data (solid line) with the number of longitudinal modes M as a free parameter.*

testing, the null hypothesis is that the measured statistics corresponds to the reference SASE distribution. The significance level, at which this hypothesis is rejected, has been typically set to 0.001.

Another test calculates the pulse energy $\mathcal{E}_{bw}$ of the measured FEL spectra within the bandwidth of the seed laser. If this energy exceeds a certain value $\mathcal{E}_0$, it is counted as an event. If $p(\mathcal{E}_{bw} > \mathcal{E}_0)$ is the single-shot probability for such an event to occur, then the probability that one observes a number of k events in N single-shot spectral measurements is given by the binomial distribution:

$$P(k, N, p(\mathcal{E}_{bw} > \mathcal{E}_0)) = \binom{N}{k} p^k (1-p)^{N-k}.$$

The probability $p(\mathcal{E}_{bw} > \mathcal{E}_0)$ can be calculated from the theoretical distribution (7.1) inferred from the SASE reference statistics to be

$$p(\mathcal{E}_{bw} > \mathcal{E}_0) = \int_{\mathcal{E}_0/\langle\mathcal{E}\rangle}^{\infty} u \cdot \frac{M^M u^{M-1}}{\Gamma(M)} e^{-Mu}\, du.$$

Figure 7.2 shows exemplarily the theoretical SASE energy distribution for $M = 7$ and the corresponding probabilities $P_{SASE}(N_{cand})$ to find N_{cand} pulses with $\mathcal{E}_{bw}/\langle\mathcal{E}\rangle > 1.88$ in $N = 500$ spectra. The absolute value of $\mathcal{E}_0$ is arbitrarily defined by choosing the condition $p(\mathcal{E}_{bw} > \mathcal{E}_0) = 5\,\%$. With this, it is only dependent on the number of longitudinal modes M. In this example, the probability to measure 30 pulses with a normalized energy larger than 1.88 out of 500 SASE shots is 4.56 %.

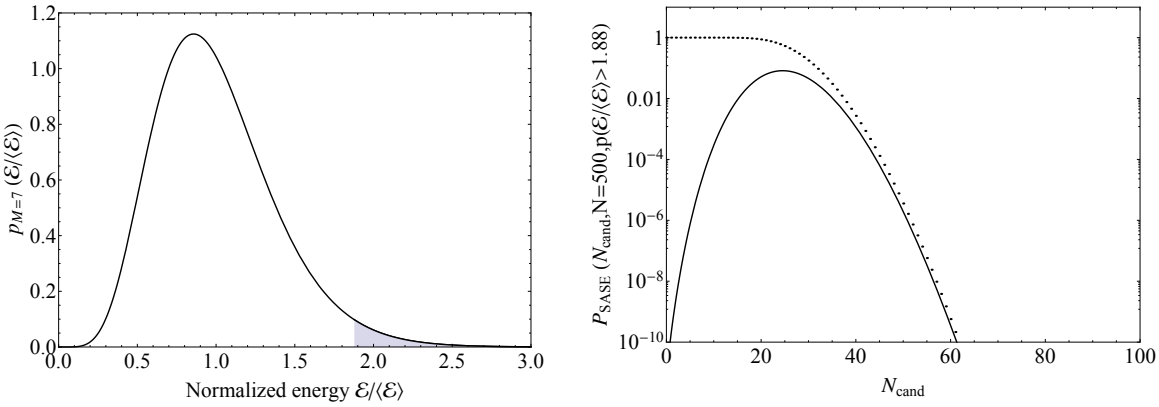

(a) (b)

Figure 7.2: *(a) shows the normalized energy distribution for SASE pulses for $M = 7$ longitudinal modes. The shaded area represents a 5 % probability and defines the value $\mathcal{E}_0$ (here 1.88) above which pulses are counted as seed candidates. (b) plots the probability to find N_{cand} pulses out of $N = 500$ SASE shots which exceed the normalized energy by a factor of 1.88. The dotted line represents the probability to measure a larger number of pulses than N_{cand}.*

Acquisition Filters

To prevent changes of the statistical distribution due to machine fluctuations, spectra are only recorded if several machine parameters are within a certain filter range (e.g. signals from bunch compression monitor, beam energy monitor, charge monitors, arrival time monitors and beam position monitors). The SASE reference data are recorded using such machine parameter filter, too. Figure 7.3 shows measurements of different machine parameters recorded before a time delay scan. Usually, a filter range of $\pm 2.6\,\sigma$[1] was used which increased the acquisition time by roughly a factor of 2. On the one hand, all of the single-shot measurements should be taken at exactly the same conditions, what calls for a small filter range. On the other hand, when the range is too small then the time needed to perform the scan becomes too long. Therefore, the choice of filter range is, for practical reasons, a compromise, which allows to accomplish the time scan within one hour or less. In general, one should use individual ranges for each machine parameter, depending on its sensitivity to the SASE performance.

For each time step, at least 300 FEL spectra are recorded. This is motivated by the changing probability for the laser-electron overlap due to the different sources of fluctuations in each dimension, namely the longitudinal and transverse jitter of both pulses and the fluctuation in pulse energy. Using an idealized model for the transverse and the longitudinal overlap, an estimate for the expected frequency to exceed a certain value for the

[1] σ one standard deviation of data set

overlap probability can be calculated. With the measured values for the transverse and longitudinal jitter, this frequency was calculated to be about 15 % (see Appendix D). The fluctuations of the seed pulse energy were not considered here. The seed laser is switched on and off every 50 spectra which would give a clear evidence for seeding if the change in signal is directly correlated with the presence of the seed laser. A direct correlation of the FEL output with the seed laser intensity would be desirable, but is not possible so far (see Chapter 8).

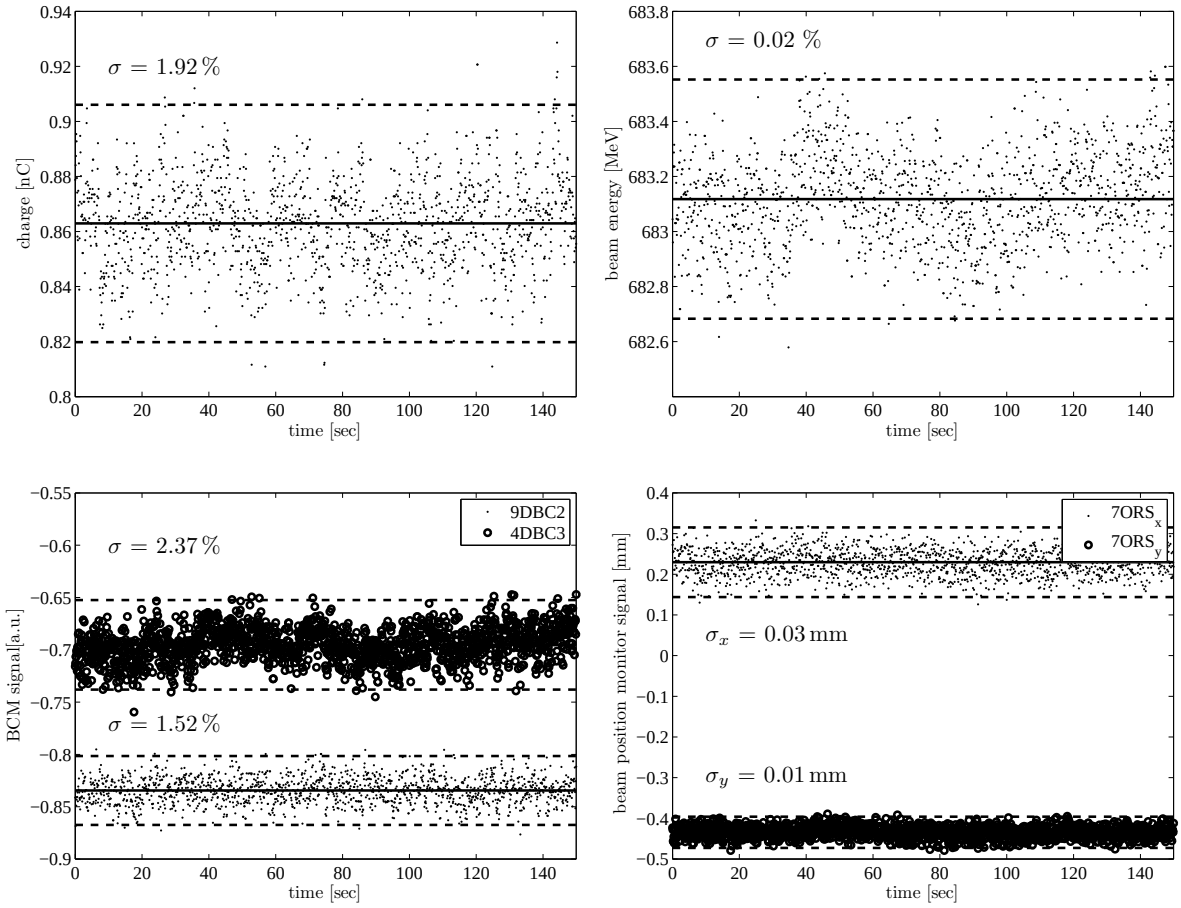

Figure 7.3: *Machine parameters recorded before a time delay scan to find the temporal overlap. The mean values (solid line) and the* $\pm\, 2.6\,\sigma$ *bands (dashed lines) of the data are indicated. Upper left: electron bunch charge, upper right: electron beam energy, lower left: bunch compression monitor signals, lower right: beam position at 7ORS (see Fig. 5.2*

Results of Time Delay Scans

After commissioning of all hardware and software for the data acquisition of the FEL spectra, two shifts of about 8 hours were used for time delay scans. The results of the on-line data analysis tool for the first and second shift block are plotted in Fig. 7.4(a)

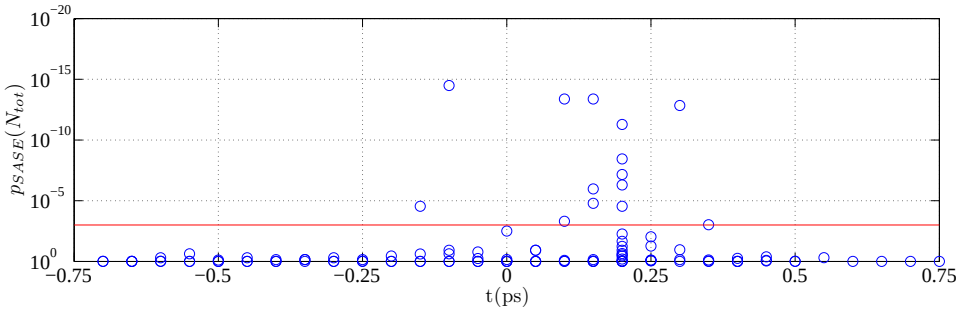

(a) shift block March 26th/27th

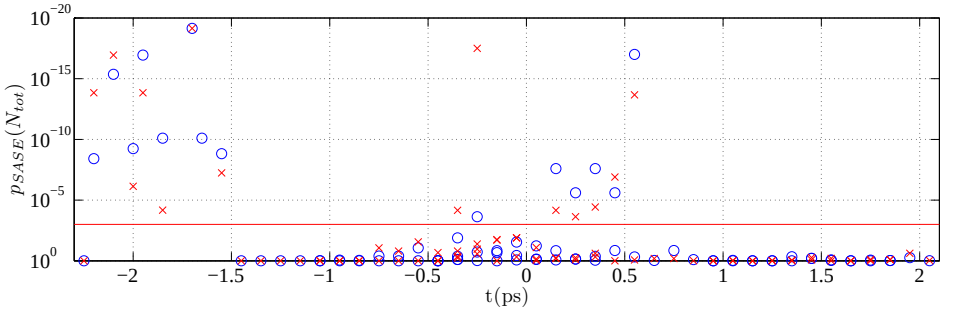

(b) shift block April 8th/9th

Figure 7.4: *Results of the on-line analysis tool for two shift periods. The probability that the number of spectra exceeding a critical energy which is generated by SASE is plotted against the time delay. The temporal overlap is expected to be at* $t = 0 \pm 1\,ps$*. During the second shift block (b) the seed laser was switched on (open cycles) and off (crosses) after recording 50 spectra.*

and Fig. 7.4(b), respectively. They show the probability $P_{SASE}(N_{tot})$ that the number of spectra exceeding a certain energy is generated by SASE. During the first shift block there were a few events for which the probability dropped below the critical probability defined by a confidence bound of 99.9 %. In order to verify that such events are really produced by the seeding process, the laser was switched on and off after recording 50 spectra during the second shift block. It can be seen, that there are again several events falling below the critical probability, but they can not be correlated with the presence of the seed pulse. Therefore, one has to conclude that these events where created by machine fluctuations, which where not covered by the machine filter algorithm, resulting in a change of the SASE statistics.

7.3 Offline Data Analysis

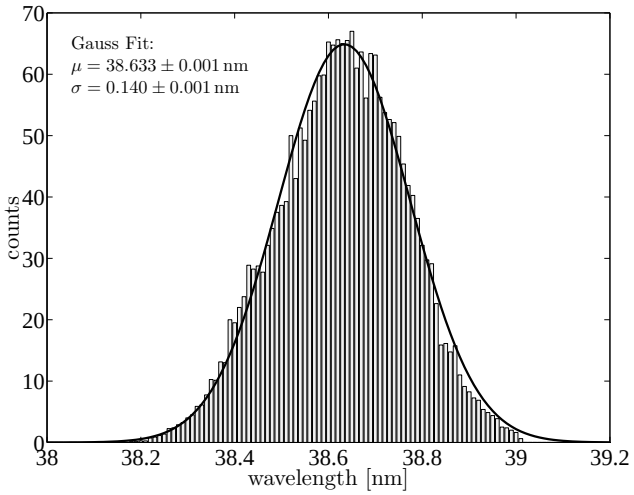

Figure 7.5: *Result of the peak counting algorithm.*

The tool for on-line data analysis uses the absolute values of the FEL spectra. Therefore, pulses with a low energy compared to the average over many pulses ($\mathcal{E}/\langle\mathcal{E}\rangle < 1$) will not be visible in the analysis results since only those pulses which exceed a critical energy will be counted. In order to find an evidence for seeding, it might be interesting to analyze the FEL spectra which have a rather low energy compared to the average energy $\langle\mathcal{E}\rangle$. Therefore, the spectra were analyzed in the following way. First, the ratio of the maximum I_{max} to the mean value I_{mean} of the spectrum was calculated. If this ratio was larger than a certain value, the wavelength of this maximum was determined. Afterwards, all wavelength values were plotted in a histogram with a bin width of 0.05 nm. Using this procedure histograms for all FEL spectra for each time delay scan were generated. For SASE spectra the values should be normal-distributed with the mean value at the resonance wavelength and a width comparable to the bandwidth of the FEL. If seeding occurs, the distribution should be changed only at the seed wavelength. Figure 7.5 shows a distribution generated with experimental SASE data. Figure 7.6 exemplarily shows the results of one time delay scan performed during the first shift block on March 26th and 27th, 2011. The central wavelength of the seed laser is indicated by a dashed vertical line. The reference distribution (SASE) with a Gaussian fit is plotted in comparison to the distribution recorded at each time delay. At the time delays $t = -0.45$ ps to $t = -0.30$ ps an increase of the number of peaks at $\lambda = 38.58$ nm is visible, but simultaneously the number of peaks at lower wavelengths decreases. Such drift of the complete spectrum could be correlated with machine parameters, as can be seen in Fig. 7.7 and Fig. 7.8. Here, the first moment of the wavelength distribution $\langle\lambda\rangle$ is plotted against several machine parameter values (averaged over all shots per delay time) for all delay times. It shows that

the changes in the first moment are correlated with the orbit, the beam energy, and the pyro-detector signal of the bunch compression monitor.
At the time delay at $t = 0.30\,\mathrm{ps}$, again, an increase of the number of peaks can be seen at the seed wavelength. In addition, the rest of the distribution qualitatively fits the reference distribution. Such a signature indicates that the FEL spectrum might be effected for a few shots due to the presents of the seed laser. Nevertheless, such signal could not be reproduced during the second shift block. The evaluation of the data of the second shift block does not show any significant increase of the number of peaks at the seed wavelength. There is a clear correlation between the center wavelength and the electron beam energy, the bunch compression monitor signal of the second bunch compressor, as well as the beam orbit (see Fig. 7.8). During that shift, the compression feedback system was used to stabilize the bunch compression at the first bunch compressor (see *9DBC2* in Fig. 7.8). The system acts on the phase of the first accelerating module and compensates changes in the electron gun. Usually, the changes in the setpoint for the phase are below $0.05\,^\circ$. During that shift, a periodic drift in the gun section caused the feedback to change the phase setpoint by more than $0.4\,^\circ$. Thus, the arrival time of the electron bunches at the following accelerating modules was changed which resulted in a changed compression in the second bunch compressor and a different final beam energy.

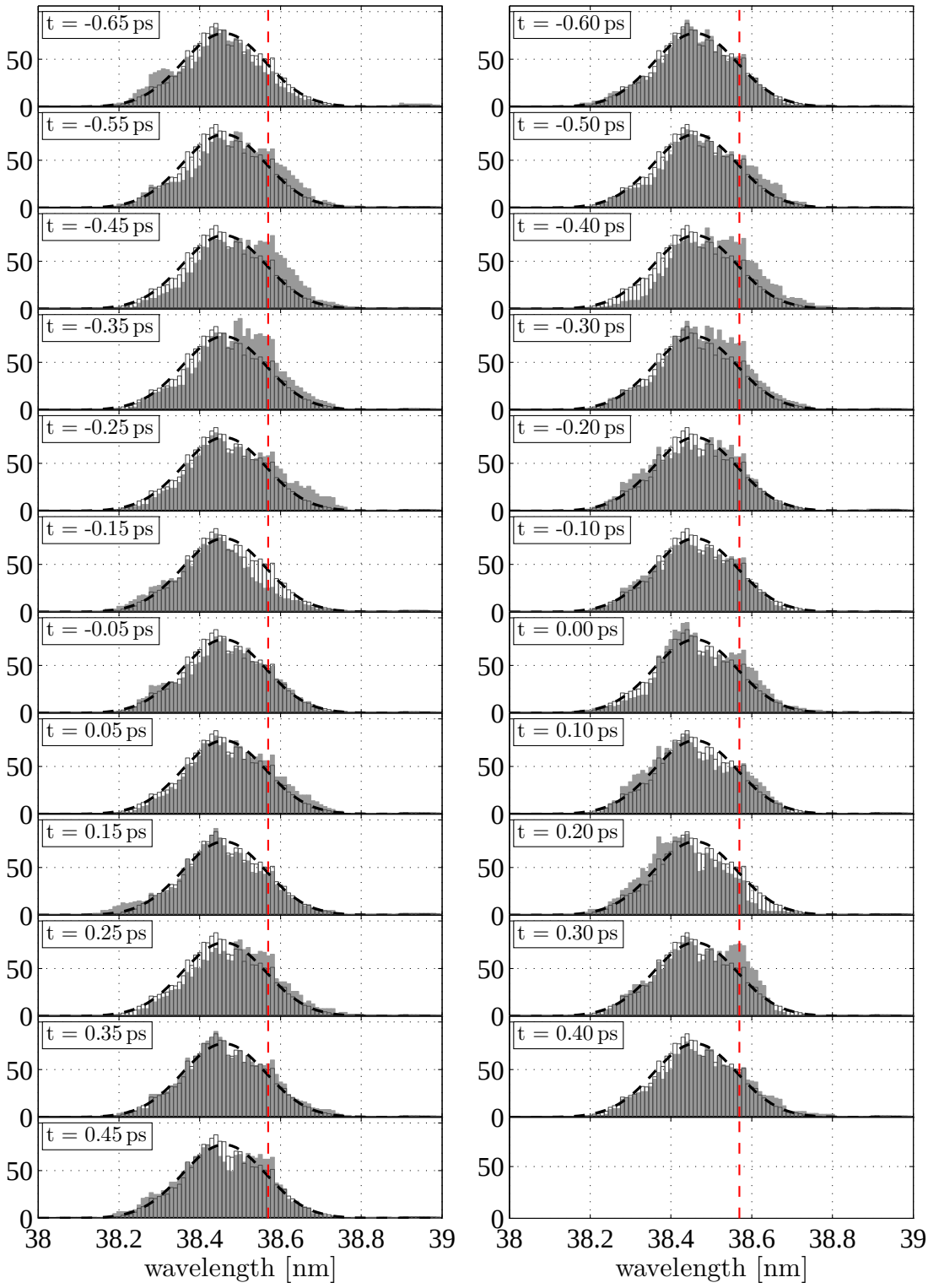

Figure 7.6: *Results of one time delay scan from the first shift block (March 2011). The dashed vertical line indicates the central wavelength of the seed laser. The reference SASE distribution and a Gaussian fit to it is plotted with open bars and a dashed line, respectively. The distribution for each time delay is plotted with gray bars.*

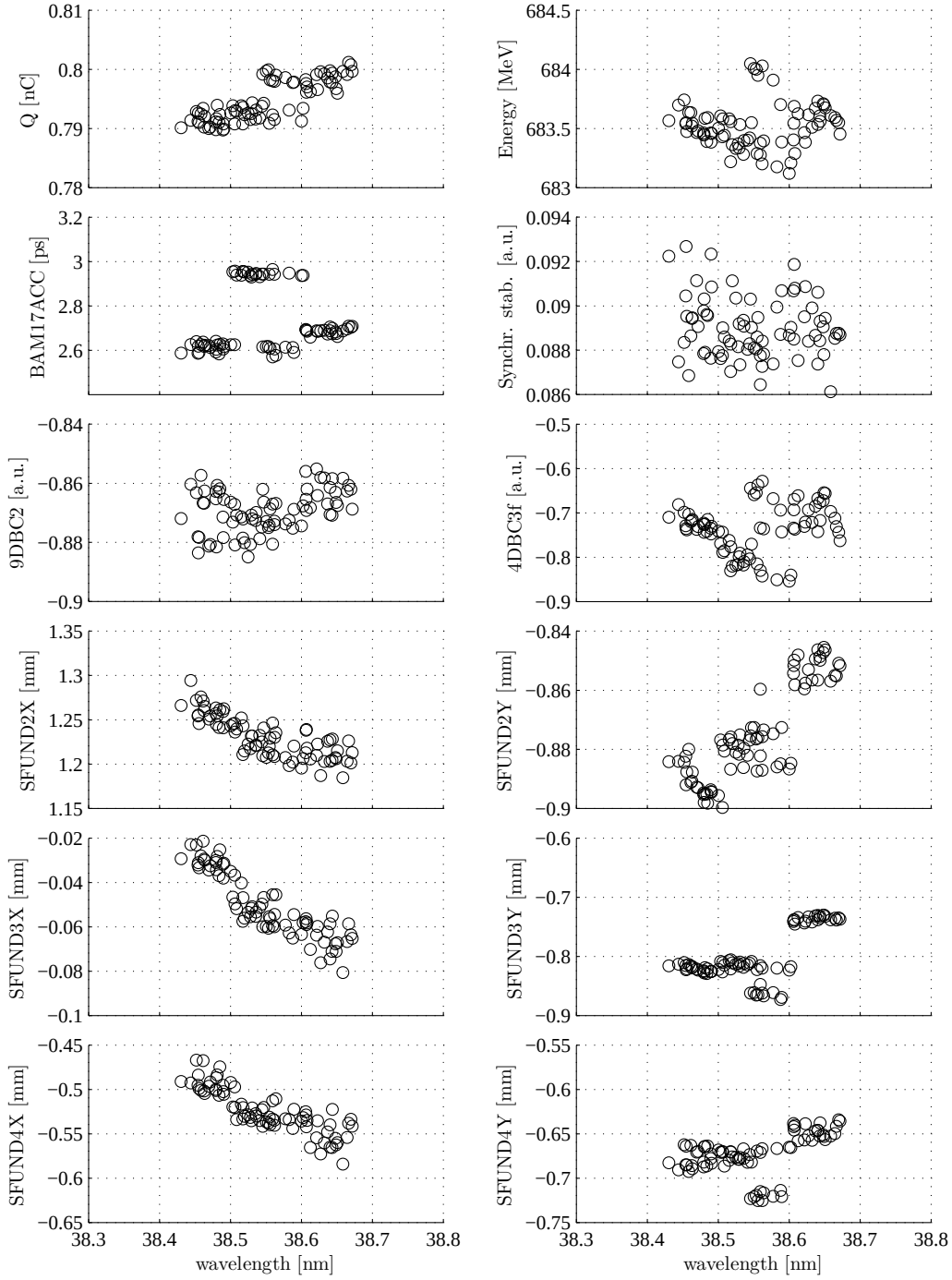

Figure 7.7: *Correlation of the first moment $\langle\lambda\rangle$ of the wavelength distribution with different machine values during the first shift block (March 2011). Q: Bunch charge measured at 7ORS. Energy: Beam energy measured at the energy collimator. BAM17ACC: Beam arrival time after last accelerating module. Synchr. stab.: ADC signal of the synchronization system for the seed laser. 9DBC2/4DBC3f: signal of bunch compression monitor after the first and second bunch compressors. SFUND2-SFUND4: Horizontal and vertical beam position at three consecutive beam position monitors.*

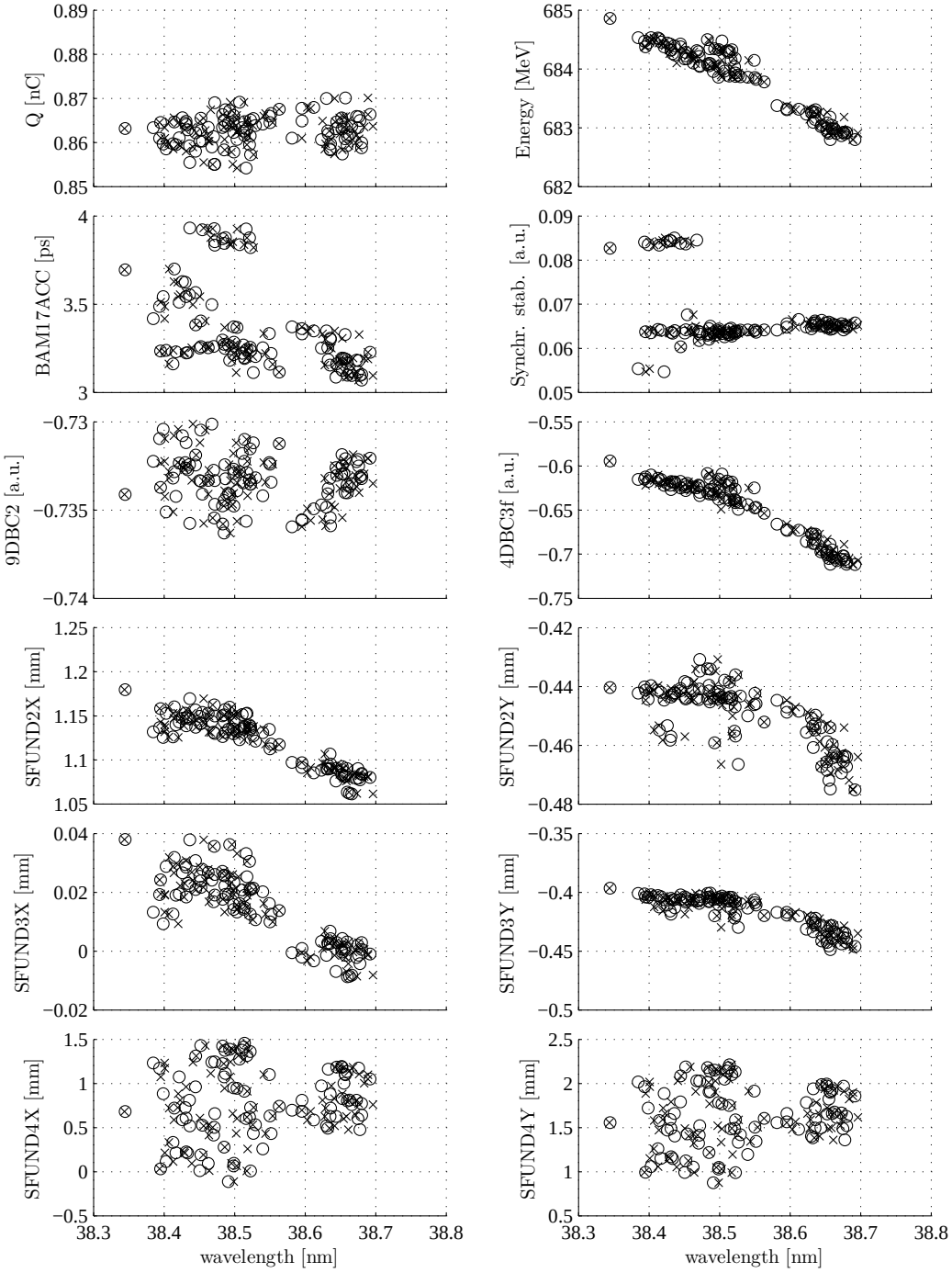

Figure 7.8: *Correlation of the first moment $\langle\lambda\rangle$ of the wavelength distribution with different machine values during the second shift block (April 2011). Q: Bunch charge measured at 7ORS. Energy: Beam energy measured at the energy collimator. BAM17ACC: Beam arrival time after last accelerating module. Synchr. stab.: ADC signal of the synchronization system for the seed laser. 9DBC2/4DBC3f: signal of bunch compression monitor after the first and second bunch compressors. SFUND2-SFUND4: Horizontal and vertical beam position at three consecutive beam position monitors.*

8 Conclusion and Outlook

Free-electron lasers producing extreme ultraviolet, soft- and hard-X-ray pulses with a peak brilliance of up to 10^{34} photons/(s mm^2 mrad^2 0.1 % bandwidth) and pulse durations of the order of tens of femtoseconds open new possibilities for a broad range of scientific applications. In order to study and control the dynamics of molecules and atoms on a femtosecond time scale, optical laser pulses need to be synchronized with FEL pulses at the same time scale. In addition, the FEL pulse characteristics, such as pulse intensity or time structure, preferably should be stable. Due to the nature of the SASE FEL process, the temporal coherence is poor and the temporal pulse structure, respectively, changes from shot-to-shot. One solution to improve the coherence of the FEL is to set up a direct laser-seeded FEL. Simultaneously, the FEL pulses are intrinsically synchronized with optical laser pulses of the seed laser system. For the XUV wavelength region, the external seed laser can be produced by high-harmonic generation of infrared laser pulses.

A test experiment of such direct HHG-seeded FEL was installed at FLASH in 2010 to test the feasibility for HHG-seeding at wavelengths below 40 nm. One challenge, beside others within this project, was the injection beamline for the seed laser and the diagnostics to measure and control the spatial overlap between seed laser and electron beam. Therefore, tolerance analysis for the dependency of the focusing and the wavefront irregularities of the XUV beam on the FEL process were performed. The results show, that an rms wavefront distortion of $\lambda/4$ ($\lambda = 38$ nm) leads to a degradation of the seeded FEL performance of 10 %.

A dedicated transport system for the XUV beam from the HHG source into the undulator was designed and set up. It consists of two mirror chambers, each accommodating remotely selectable mirrors suitable for 38 nm and 13 nm (two different coatings on one substrate). In the first chamber, a single plane mirror substrate reflects the beam to the focusing mirrors. The second mirror chamber contains a set of six focal mirrors with two different multi-layer coatings and three different focal lengths, and a triplet of three plane mirror substrates, needed to reflect the XUV beam coaxial to the electron beam axis. The focal mirrors can be remotely selected and adjusted in angle and position in order to align the photon beam through the undulator vacuum chamber. The required position-

ing accuracy was defined by the allowable mismatch of the transverse overlap of electron and photon beam which was calculated to be 35 μm and 22 μrad in position and angle. Therefore, the reproducibility of each mirror angle has to be below 2 μrad.

For the measurement of the transverse overlap of electron and photon beam, several diagnostic stations were designed and set up in the undulator section. These allow beam profile and position measurements using screen and wire scanner methods. The resolution with both methods is better that 15 μm and is limited by the high acceptance optics and the wire thickness respectively.

The photon beam profiles along the injection beamline and along the undulator were measured in order to determine the longitudinal focus position of the XUV beam. It was observed that the beam sizes of the XUV beam were larger than expected. In addition, the XUV beam shows waist size and divergence asymmetries, as well as astigmatism. The longitudinal positions of the astigmatic beam waists were measured to be (23 ± 21) cm in front of the undulator entrance and (24 ± 28) cm after the center of the first undulator module, respectively. The astigmatic behavior can be explained by a deformation of the focusing mirror resulting in different focal lengths along in different optical planes. The divergence and the beam waist asymmetries are most likely direct properties of the HHG source. The characterization of the transverse beam parameters at the HHG source is still under investigation.

The injection beamline and the diagnostic stations were successfully commissioned and used to set the laser-electron overlap close to the required tolerances. For the determination of the beam centers, the mean value of a Gaussian fit of the beam profiles was used. It was shown that for different determination methods of the beam center, the absolute values differ significantly from each other.

During first studies for seeded FEL operation, several time delay scans were performed in order to find the six-dimensional laser-electron overlap. The on-line analysis of the FEL spectra has not shown any clear evidence for seeding. During post analysis of the data, some of the delay scans show a change of the spectral distribution. Most of these changes could be correlated to machine parameters of the accelerator. One of the spectral distributions shows an increase of the signal at the wavelength of the seed laser. Since it was not possible to correlate this signal with the presence of the seed laser pulses, one needs to be careful with the interpretation. It can not be excluded that such fluctuations are caused by changes of the electron beam properties.

The measurements of the transverse beam size of the XUV beam show that the transverse laser-electron coupling is not optimal due to the large XUV beam size compared to the electron beam. In combination with a low seed pulse energy, this will cause an effective seed beam power which is on the same order than the shot noise power of the electron beam. With this, the signal-to-noise ratio might be too low for a direct identification of

seeding.

Several improvements on the sFLASH setup are foreseen. An XUV photo diode in the undulator section is supposed to measure the absolute seed pulse energy. With this, it will be possible to measure the absolute transmission of the injection beam line. An MCP will be installed close to the last injection mirror. This allows to detect photo electrons emitted from the mirror surface. The MCP signal is going to be used as an on-line pulse energy monitor for the seed laser and can be used to directly correlate the seeded FEL signal with the seed pulse energy. Currently, an option for using a focusing mirror with variable focal length is studied. By applying a force on the back side of the mirror substrate, the curvature of the mirror is reduced and therefore the focal length is increased. Such a mirror would allow to optimize the longitudinal beam waist position. The XUV beam quality or, in other words, the wavefront of the XUV beam cannot be controlled. In order to do that, one would need to develop an adaptive mirror capable to correct wavefront distortions of XUV beams with sufficient accuracy.

For the upcoming upgrade of the FLASH facility, namely FLASH II [FBA+11], an additional undulator beamline will be installed parallel to the existing FLASH I SASE undulator. For the new FEL beamline, a seeding option is foreseen using an HHG source based on quasi-phase matching [WYD+11]. A new injection beamline has to be set up, capable to effectively transport a wide range of wavelengths from 40 to 10 nm. For the focusing into the undulator, an adaptive optic would be desirable in order to precisely adjust the focus along the undulator and to correct for possible beam distortions from the HHG source.

A Abbreviations

Abbreviation	Definition
ACC	accelerator module
BC	bunch compressor
BLM	beam loss monitor
BPM	beam position monitor
CCD	charge-coupled device
CMOS	complementary metal oxide semiconductor
COTR	coherent optical transition radiation
CPA	chirped pulse amplification
EEHG	echo enabled harmonic generation
EMCCD	electron multiplying charged-coupled device
ESASE	enhanced self-amplified spontaneous emission
FEL	free-electron laser
FELO	free-electron laser oscillator
FLASH	free-electron laser in Hamburg
FWHM	full width half maximum
HGHG	high gain harmonic generation
HHG	high-harmonic generation
LCLS	Linear Coherent Light Source
LINAC	linear accelerator
MCP	multi channel plate
Nd:YAG	neodymium-doped yttrium aluminum garnet
NIR	near infrared
OTR	optical transition radiation
ORS	optical replica synthesizer
PETRA	Positron Elektron Tandem Ring Anlage
PMT	photomultiplier
RF	radio frequency
rms	root mean square
SASE	self-amplified spontaneous emission
SCSS	Spring-8 Compact SASE Source
Ti:sapphire	titanium-doped sapphire
UV	ultraviolet
VUV	vacuum ultraviolet
XFEL	X-ray free-electron laser
XUV	extreme ultraviolet

Table A.1: *Abbreviations used within this thesis.*

B Reflectivity Data

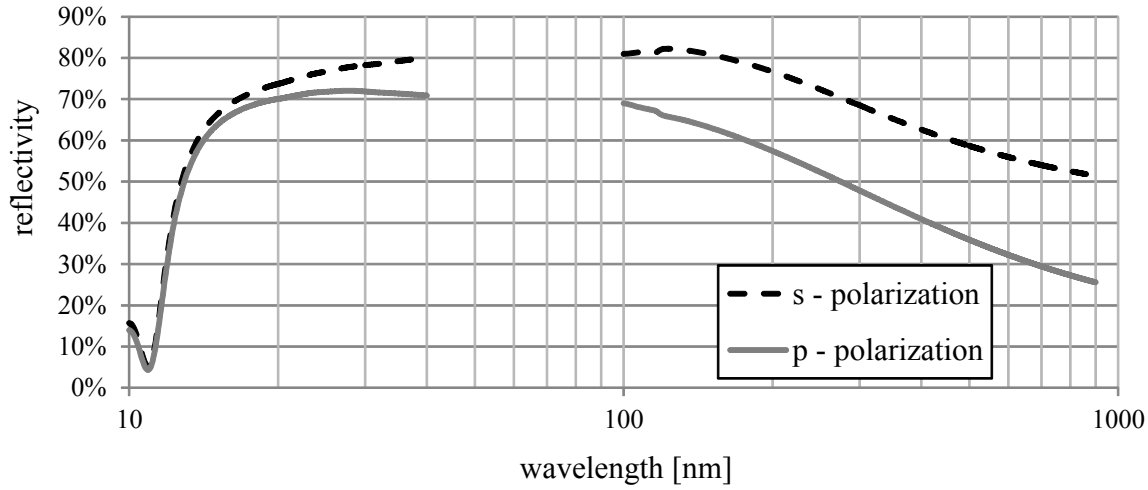

(a) reflectivity data

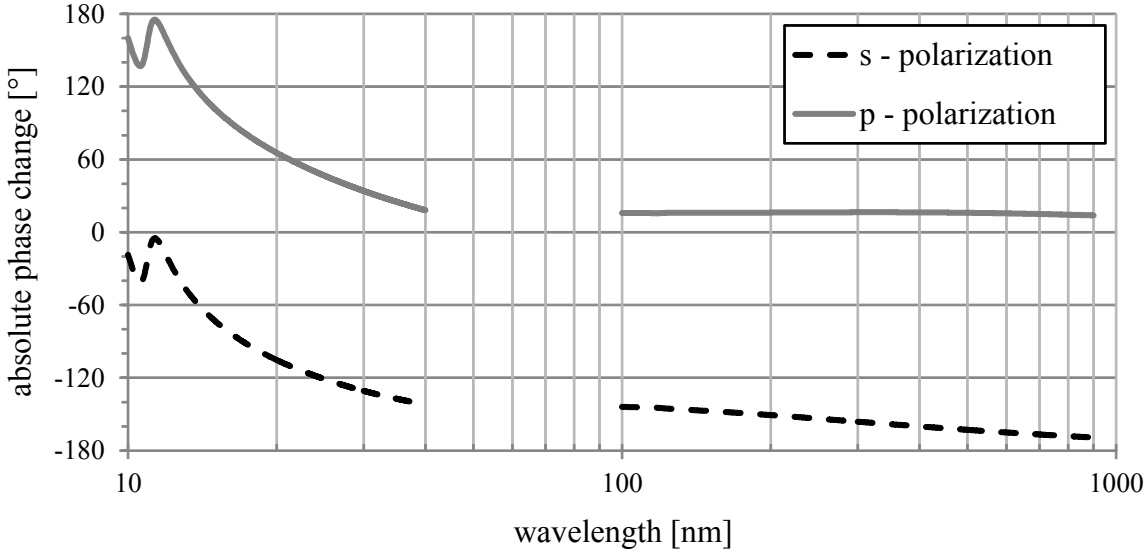

(b) phase data

Figure B.1: *Reflectivity (a) and absolute phase (b) of Ti/B_4C coating for s- and p-polarized beams. Curves generated with IMD [Win98].*

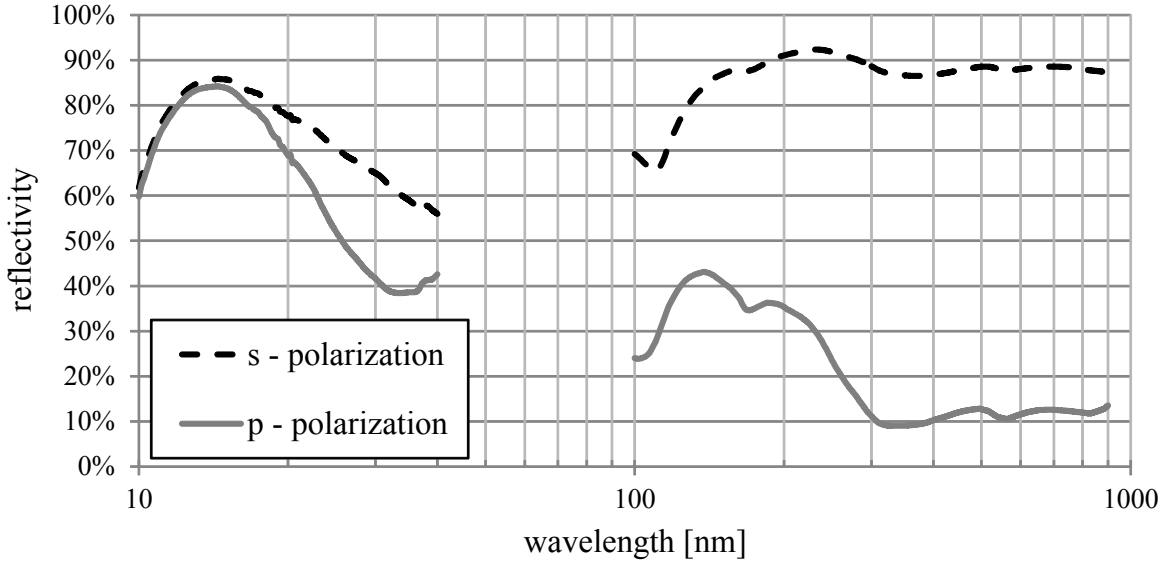

(a) reflectivity data

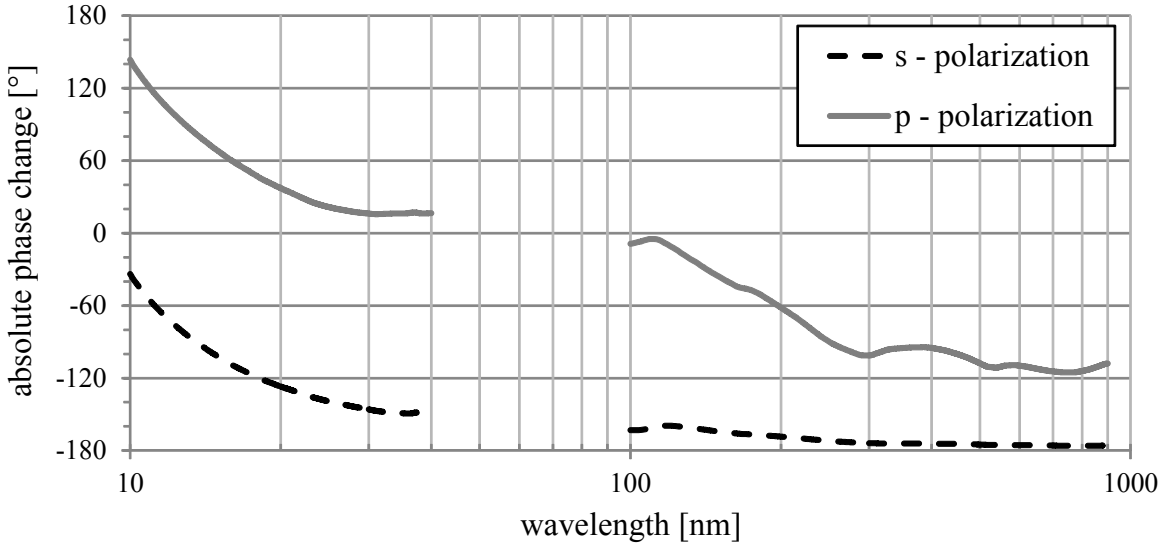

(b) phase data

Figure B.2: *Reflectivity (a) and absolute phase (b) of Mo/B_4C coating for s- and p-polarized beams. Curves generated with IMD [Win98].*

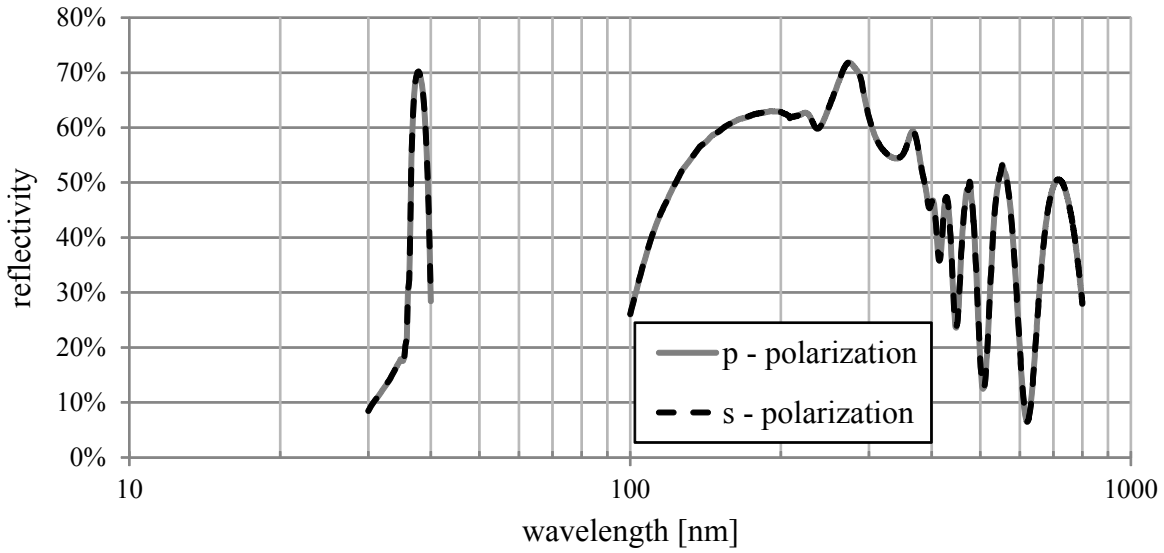

(a) reflectivity data

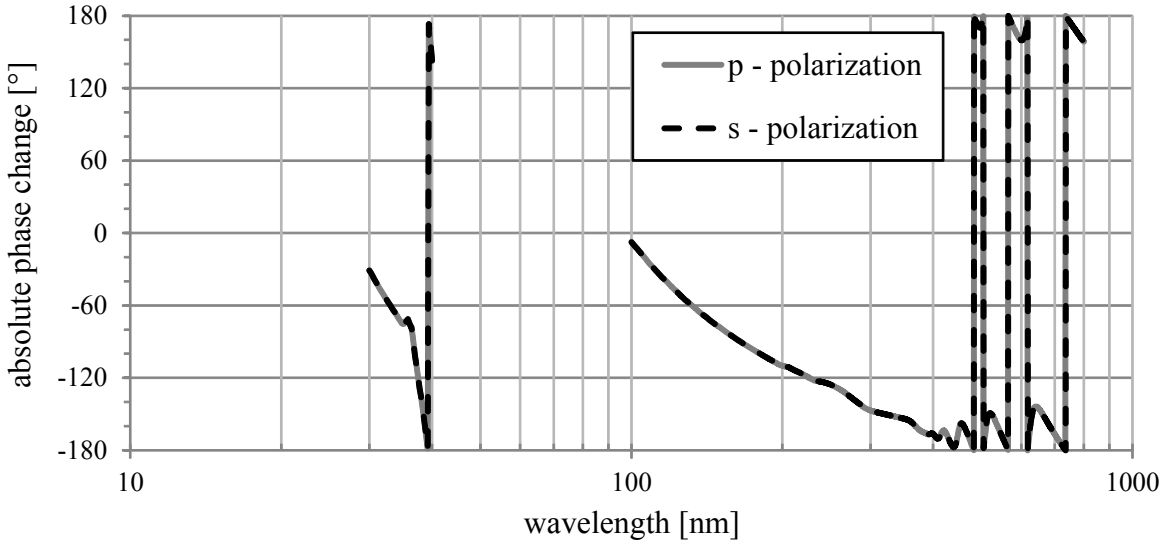

(b) phase data

Figure B.3: *Reflectivity (a) and absolute phase (b) of Sc/Si multi-layer coating for s- and p-polarized beams. Curves generated with IMD [Win98].*

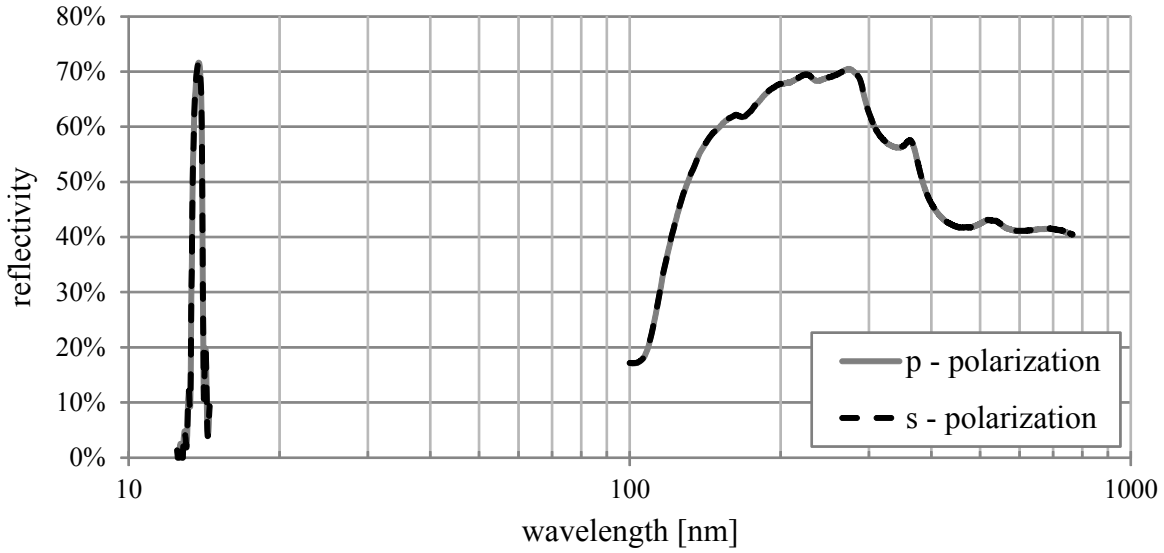

(a) reflectivity data

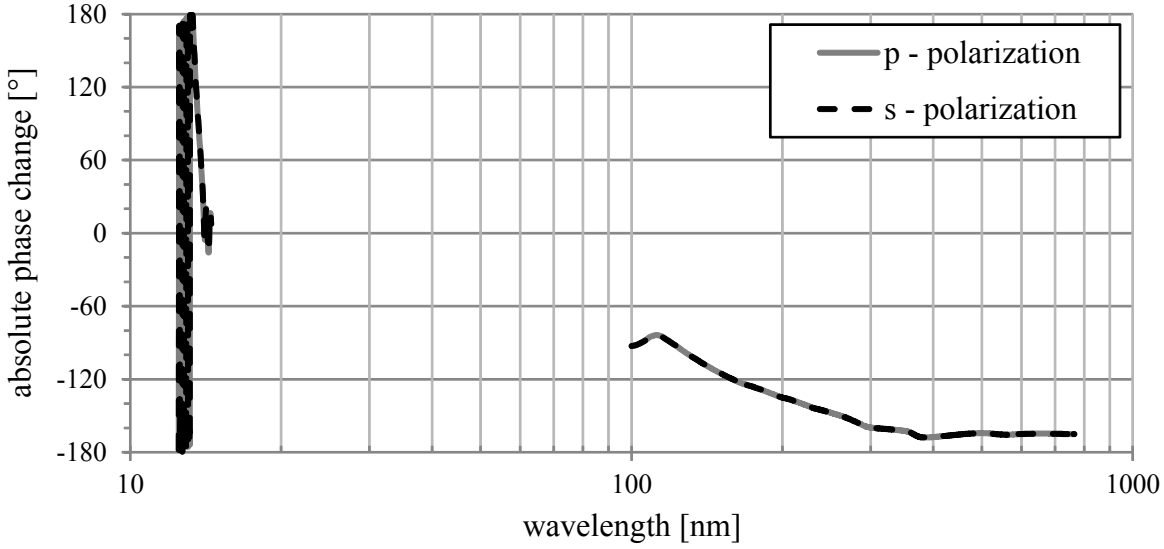

(b) phase data

Figure B.4: *Reflectivity (a) and absolute phase (b) of Mo/Si multi-layer coating for s- and p-polarized beams. Curves generated with IMD [Win98].*

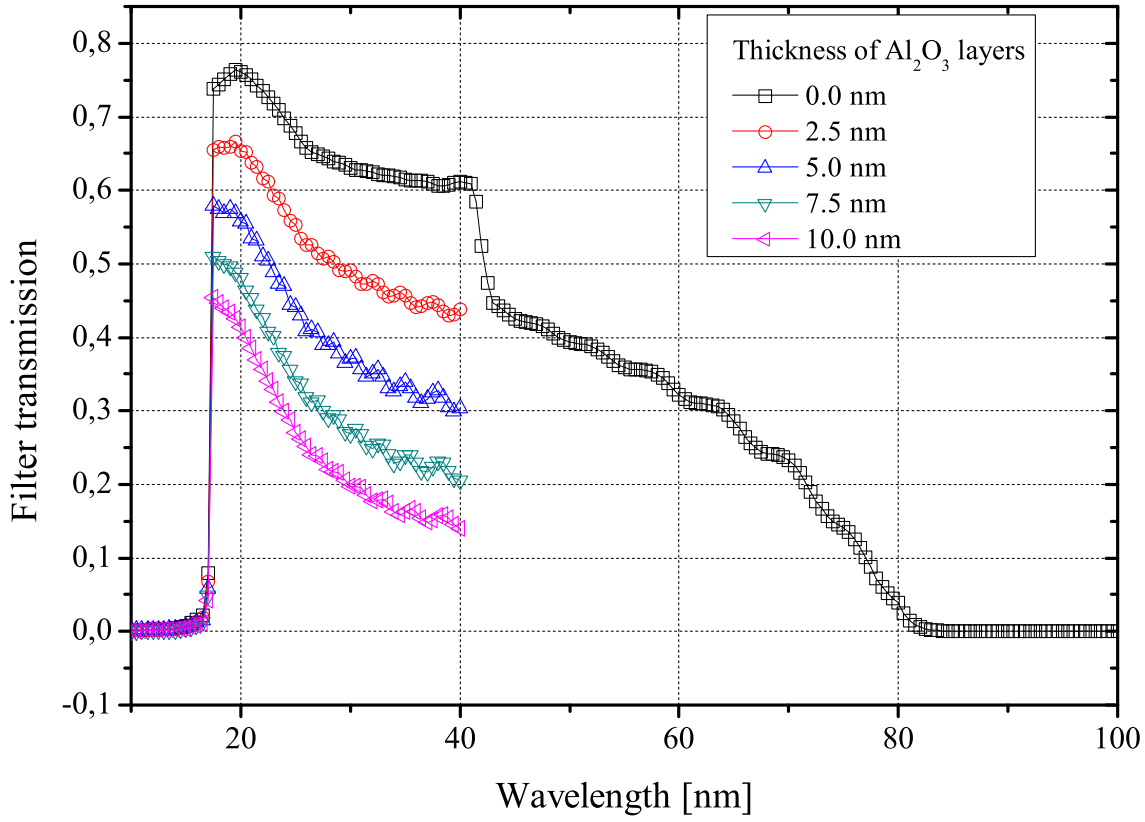

Figure B.5: *Theoretical transmission of 200 nm thick aluminum filter with layers of Al_2O_3 on both sides. Curves generated with IMD [Win98].*

C Gaussian Beams and Higher Order Transverse Modes

C.1 Gaussian Beam Propagation

The propagation of laser beams can be modeled, using the complex q-parameter, which is a result of the solution of the paraxial wave equation [KL66] and describes the evolution of the phase front of an idealized laser beam with wavelength λ along the propagation axis z:

$$q(z) = \frac{1}{R(z)} - i\frac{\lambda}{\pi w(z)}. \tag{C.1}$$

The wave front curvature $1/R$ and the beam size w can be easily calculated from that. The point, where the wave front curvature is zero, is called beam waist w_0. Other commonly used parameters are the Rayleigh length z_R and the far-field divergence θ of the beam, defined by

$$z_R = \frac{\pi w_0^2}{\lambda} \tag{C.2}$$

$$\theta = \lim_{z\to\infty} \frac{w(z)}{z} = \frac{\lambda}{\pi w_0}. \tag{C.3}$$

Consequently, the beam size along the z-axis evolves with

$$w(z) = w_0\sqrt{1 + \frac{(z - z_w)^2}{z_R^2}} \tag{C.4}$$

The propagation law for the q-parameter is given by

$$q_{out} = \frac{Aq_{in} + B}{Cq_{in} + D}, \tag{C.5}$$

where A, B, C and D are the matrix elements of the ray matrices for optical elements [KL66]. Thus, one can model the beam size along arbitrary optical systems. Laser beams containing more than the fundamental Gaussian laser mode, can be modeled using

the M^2-model [Joh98]. It gives a measure of the ability to focus a laser beam and can by defined by the so-called beam parameter product:

$$W_0 \cdot \Theta = M^2 \frac{\lambda}{\pi} \tag{C.6}$$

The uppercase letter W_0 and Θ indicates the real beam parameters and are M times larger than they would be for a perfect Gaussian beam (also called embedded Gaussian beam). With this definition, the Rayleigh length is independent of M^2. Equation C.4 then reads

$$w(z) = M \cdot w_0 \sqrt{1 + \frac{(z - z_w)^2}{z_R^2}} \tag{C.7}$$

In the ideal case of a diffraction-limited beam, M^2 equals one. For measuring the beam quality, one has to measure the far-field divergence Θ and the beam size at the waist W_0. This is discussed in detail in [Joh98].

C.2 Beam Asymmetries for Multimode Beams

For Gaussian laser beams there are two types of beam asymmetries, an asymmetric waist diameter $w_x \neq w_y$ and astigmatism $z_{wx} \neq z_{wy}$. For multimode beams with $M^2 > 1$, the asymmetry of the far-field divergence $M_x^2 \neq M_y^2$ has to be considered. Figure C.1 illustrates the different forms of beam asymmetries and shows the wavefront shape at different locations along the propagation axis. For a full characterization of the beam one has to determine all six parameters. This beam model assumes that the two propagation planes X and Y are fixed in space. The model starts to fail if one deals with laser beams that have general astigmatism [AK69]. Here, the beam ellipses rotate along the propagation axis. Such beams are generated in non-orthogonal optical systems with tilted focal elements having different tilt angles.

C.3 Global Beam Propagation Model

To determine the XUV beam parameters in the sFLASH undulator section only a limited number of screens at fixed positions along the beamline are available. In addition the screen in the injection beamline and the screens in the undulator section are separated by one focal element. Therefore, equation C.7 can not be used as the function of merit. Using a piecewise definition of the beam size along z for the space in front and after the lens, one can use the focal length f of the lens as a free parameter of the beam propagation model.

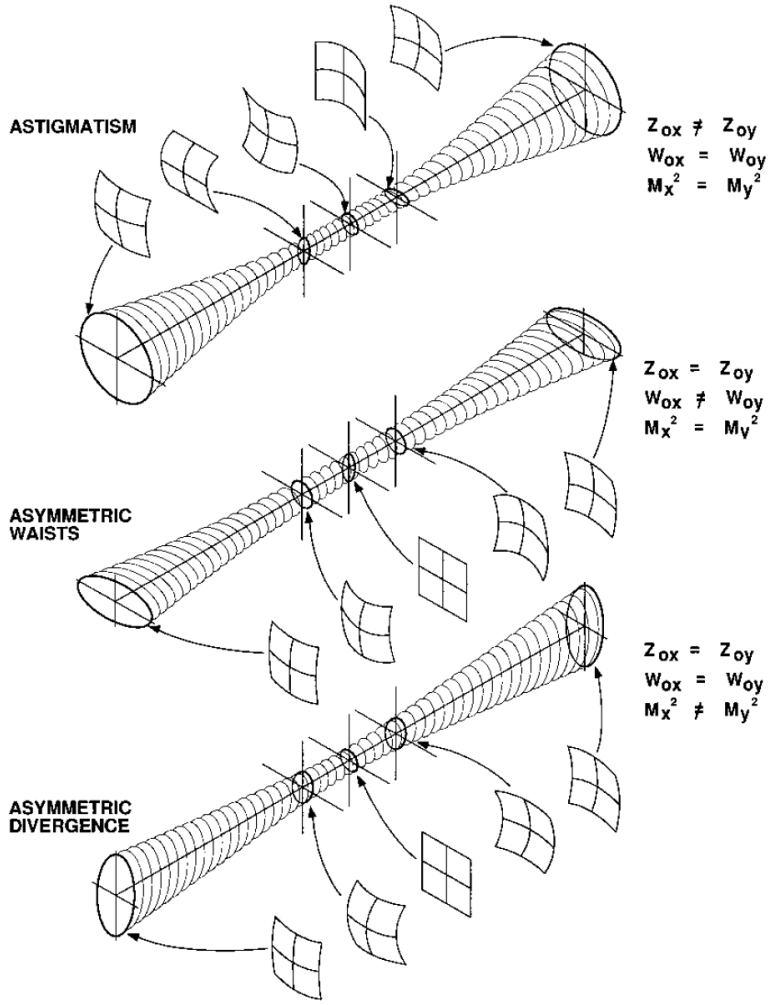

Figure C.1: *Forms of beam asymmetries for multimode laser beams. Taken from [Joh98]*

Here, one assumes that the lens does not change the beam quality factor M^2. With that, the model for the beam size of the laser beam is given by

$$q(z) = \begin{cases} \mathcal{M}_{\text{drift}}(z) \cdot q_0 & z < z_f \\ \mathcal{M}_{\text{drift}}(z) \cdot \mathcal{M}_{\text{lens}} \cdot \mathcal{M}_{\text{drift}}(z_f) & z > z_f, \end{cases} \tag{C.8}$$

where $\mathcal{M}_{\text{drift}}(d)$ and $\mathcal{M}_{\text{lens}}$ is the ray matrices for a drift space of length d and a thin lens of focal length f, respectively. The beam size is calculate by resolving C.1 to

$$w(z) = \sqrt{-\frac{\lambda}{\pi \operatorname{Im}\left(\frac{1}{q}\right)}}. \tag{C.9}$$

D Probability Estimation for Laser-Electron Overlap

In order to estimate the fluctuation of the probability of the six-dimensional laser-electron overlap, caused by fluctuations of the relative arrival time of laser pulses and electron bunches, as well as the transverse beam jitter, the following model is used. The shape of the electron bunch and the laser pulse is assumed to be Gaussian in all dimensions with (σ_t^e, σ_λ^e, σ_x^e, $\sigma_{x'}^e$, σ_y^e, $\sigma_{y'}^e$) and (σ_t^l, σ_λ^l, σ_x^l, $\sigma_{x'}^l$, σ_y^l, $\sigma_{y'}^l$) being the width in the spacial, temporal, and spectral domain for electron and laser beam, respectively. The probability P_i^{1D} for the overlap in one dimension is assumed to be the convolution of the electron bunch- and laser pulse-distribution

$$P_i^{1D}(\tau_i) = \frac{\sqrt{(\sigma_i^e)^2 + (\sigma_i^l)^2}}{\sqrt{2\pi}\sigma_i^e\sigma_i^l} \int_{-\infty}^{\infty} e^{\frac{(t-\tau_i)^2}{2\,\sigma_i^e}} \cdot e^{\frac{t^2}{2\,\sigma_i^l}}\, dt \tag{D.1}$$

$$= e^{\frac{\tau^2}{2((\sigma_i^e)^2+(\sigma_i^l)^2)}} \tag{D.2}$$

with τ_i being the offset for every dimension, e.g. the arrival time difference or the transverse offset. The probability for the six-dimensional overlap P^{6D} is assumed to be the product of the one-dimensional probabilities. The offset values τ_i are assumed to be normal-distributed with a mean value μ_{τ_i} and a standard deviation σ_{τ_i}. With this, the expectation value can be calculated that the overlap-probability P^{6D} exceeds a certain level of for example 0.8. The value depends on the widths of both beams and on the mean and standard deviations of all offset values. Table D.1 lists the assumed numbers for each parameter. Figure D.1 shows the expectation value for the condition $P^{6D} > 0.8$ as a function of the time delay μ_{τ_t} between electron bunch and laser pulse. At $\mu_{\tau_t} = 0\,\text{fs}$ the expected frequency to have a sufficient laser-electron overlap is about 15 %. This value will be additionally decreased if the fluctuations of the seed pulse energy are considered.

parameter	σ^e	σ^l	μ_τ	σ_τ
time	50 fs	10 fs	variable	120 fs
spectrum	0.2 nm	0.14 nm	0.1 nm	0.01 nm
space x	100 μm	500 μm	0 μm	25 μm
space y	100 μm	500 μm	86 μm	25 μm
angle x'	20 μrad	800 μrad	25 μrad	35 μrad
angle y'	20 μrad	800 μrad	35 μrad	100 μrad

Table D.1: *Assumed electron- and photon-beam properties for the calculation of the six-dimensional overlap probability. The mean value for the temporal offset μ_{τ_t} is varied from -500 fs to 0 fs in steps of 50 fs. This corresponds to the time delay scans which are performed to find the laser-electron overlap.*

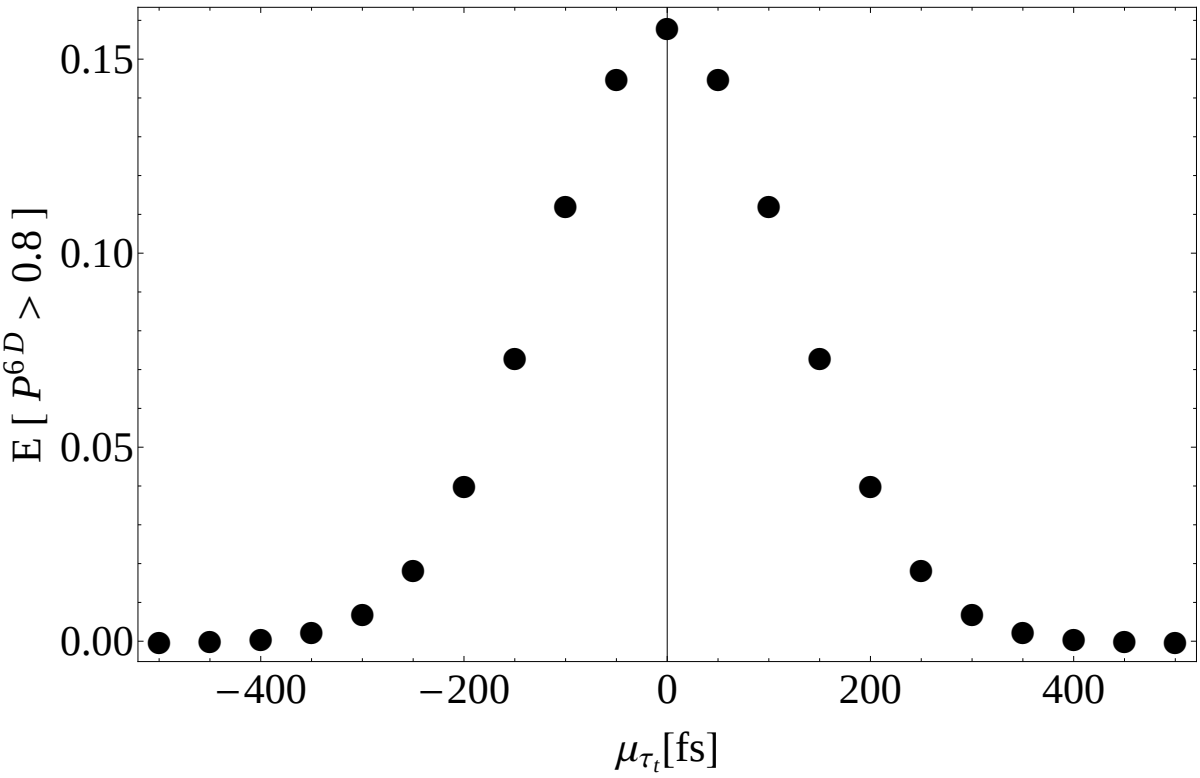

Figure D.1: *Expectation value to have a six-dimensional overlap probability P^{6D} larger than 0.8 as a function of the temporal offset μ_{τ_t}, based on a simplified model.*

E Technical Realisation of the Seed Beamline

The requirements for the realization of the sFLASH seed injection beamline were listed in Chapter 4. Due to the geometry of the location of the HHG source and the accelerator, it was clear from the beginning that a single mirror at grazing incidence will reflect the beam upwards and that a set of one spherical focusing mirror a two to four plane mirrors will reflect and focus the beam into the undulator chamber. To realize the option for transporting two wavelengths, one decided to use plane mirror substrates coated with different layers of material on the same coating (see Fig. E.1 and Tab. 4.1). The plane mirrors are moved parallel to the mirror plane to select the coating. In addition to this, the yaw and pitch angle of the first mirror in the beamline need to be remotely adjustable. Due to the ultra-clean and ultra-high vacuum requirements of the accelerator it was not possible to use in-vacuum motors. Therefore, all actuators for moving the mirror were build outside the vacuum chamber. The mirror substrate is mounted on a rocker which allows the adjustment of the yaw angle. A translation stage mounted on the rocker allows to switch between the coatings. In addition, one can move the mirror completely outside the beam axis. With an additional flange on the back of the mirror chamber one has the possibility to send the beam elsewhere, e.g. for additional diagnostics. The pitch angle can be adjusted by turning the complete mirror chamber. Figure E.2 shows a technical view of the mirror chamber.

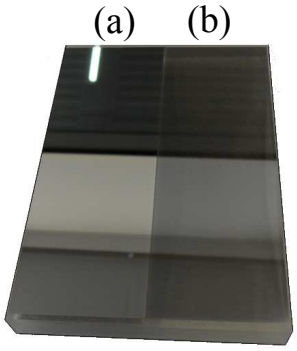

Figure E.1: *Plane mirror substrate with two different coatings: (a) Mo/B_4C $\lambda = 13\,nm$; (b) Ti/B_4C, $\lambda = 38\,nm$.*

For beam focusing, three different focal length mirrors for both wavelength were intended to be build in the beamline. Different options of mirror holders for switching and steering were suggested. Finally, one decided to use an XY-translation stage and to mount the mirrors on a circle (see Fig. E.4). With that, the translation can be used for switching the substrates and to steer the beam. Because one could not guarantee the required par-

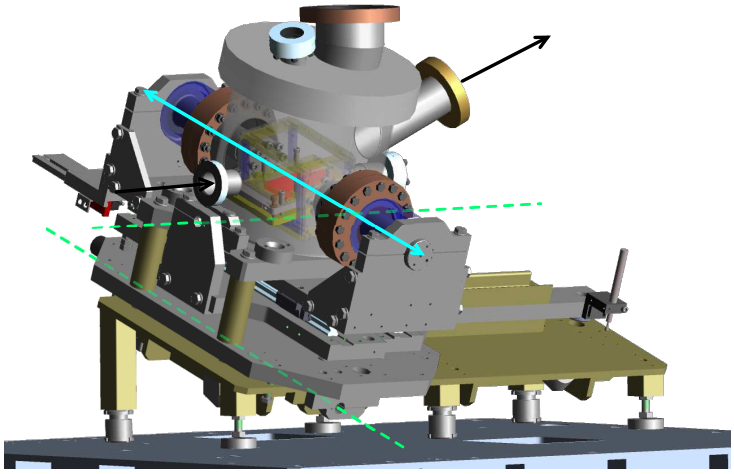

Figure E.2: *Model view of the sFLASH injection beamline mirror chamber 1. The black arrows indicate the input and output ports for the XUV beam. The dashed lines indicate the two axis of rotation. The travel direction of the translation stage on the rocker is indicated with the cyan-colored arrow.*

allelism of less than 0.65 μrad (see Tab. 4.2) between each mirror, one decided to attach mirrors on a gimbal-mounted holder to have two more degrees of freedom with the angle adjustment(see Fig. E.5).

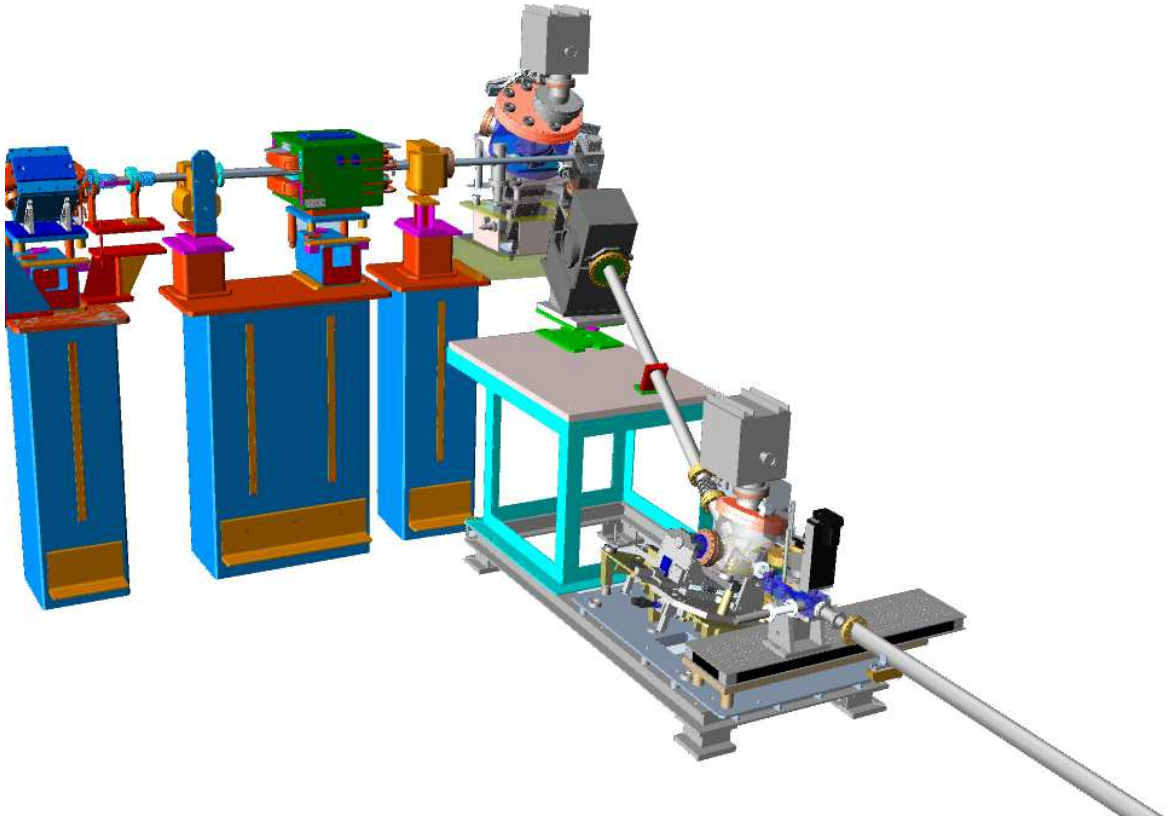

Figure E.3: *Model view of the sFLASH injection beamline.*

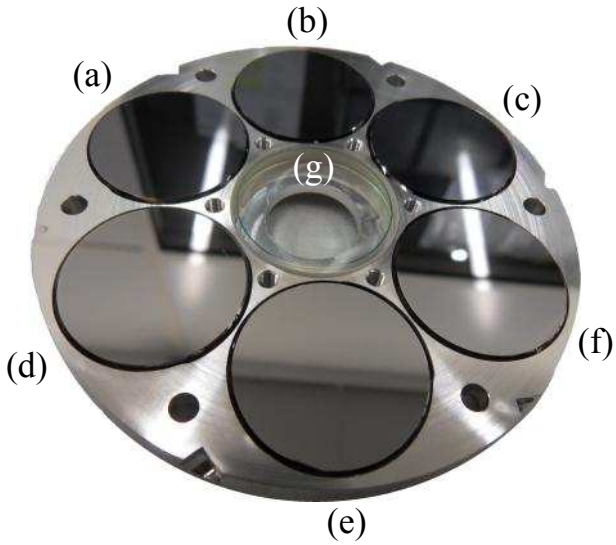

Figure E.4: *Mount with focusing mirrors for the seed laser injection beamline. The mirror have the following radii and wavelength coatings: (a) $R = 12.5\,m$, Sc/Si for $\lambda = 38\,nm$; (b) $R = 17.0\,m$, Sc/Si for $\lambda = 38\,nm$; (c) $R = 14.0\,m$, Sc/Si for $\lambda = 38\,nm$; (d) $R = 12.5\,m$, Mo/Si for $\lambda = 13\,nm$; (e) $R = 17.0\,m$, Mo/Si for$\lambda = 13\,nm$; (f) $R = 14.0\,m$, Mo/Si for $\lambda = 13\,nm$; (g) $R = 10.0\,m$, dielectric coating for $\lambda = 800\,nm$.*

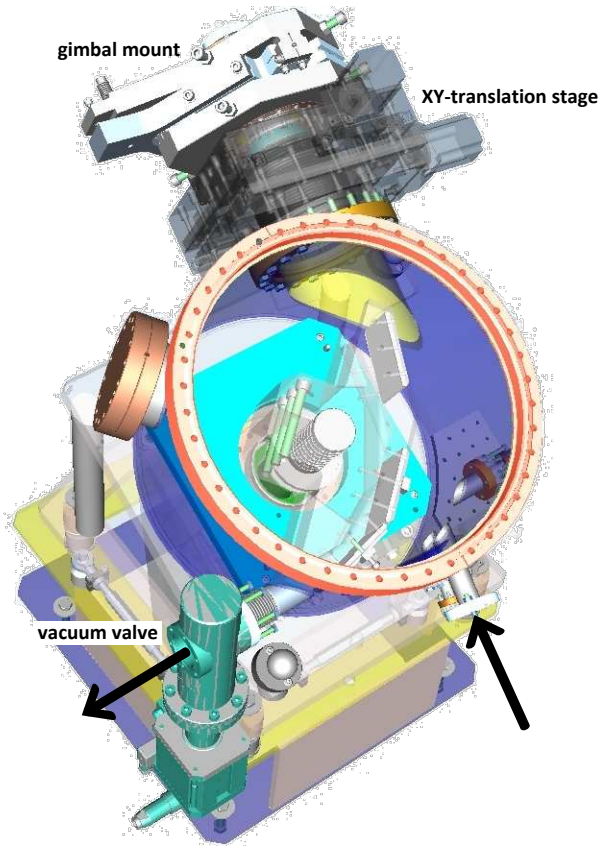

Figure E.5: *Model view of the sFLASH injection beamline mirror chamber 2. The arrows indicate the input and output ports for the XUV beam.*

Bibliography

[AAA+00] J. Andruszkow, B. Aune, V. Ayvazyan, N. Baboi, et al. First observation of self-amplified spontaneous emission in a free-electron laser at 109 nm wavelength. *Phys. Rev. Lett.*, 85(18):3825–3829, Oct 2000.

[AAA+07] W. Ackermann, G. Asova, V. Ayvazyan, A. Azima, N. Baboi, J. Bahr, V. Balandin, et al. Operation of a free-electron laser from the extreme ultraviolet to the water window. *Nature Photonics*, 1(6):336 – 342, Jun 2007.

[ABB+02a] V. Ayvazyan, N. Baboi, I. Bohnet, R. Brinkmann, M. Castellano, P. Castro, et al. Generation of gw radiation pulses from a vuv free-electron laser operating in the femtosecond regime. *Phys. Rev. Lett.*, 88(10):104802, Feb 2002.

[ABB+02b] V. Ayvazyan, N. Baboi, I. Bohnet, R. Brinkmann, et al. A new powerful source for coherent vuv radiation: Demonstration of exponential growth and saturation at the ttf free-electron laser. *The European Physical Journal D - Atomic, Molecular, Optical and Plasma Physics*, 20:149–156, 2002. 10.1140/epjd/e2002-00121-4.

[ABC+07] M. Altarelli, R. Brinkmann, M. Chergui, W. Decking, B. Dobson, S. Düsterer, G. Grübel, W. Graeff, et al. The technical design report of the european XFEL. 2007.

[Ack11] S. Ackermann. Transverse phase-space studies for FEL seeding at FLASH, 2011.

[AK69] J. A. Arnaud and H. Kogelnik. Gaussian light beams with general astigmatism. *Appl. Opt.*, 8(8):1687–1693, Aug 1969.

[BBH+95] K. Balewski, W. Brefeld, U. Hahn, J. Pfluger, and R. Rossmanith. An undulator at PETRA II-a new synchrotron radiation source at DESY. In

Particle Accelerator Conference, 1995., Proceedings of the 1995, volume 1, pages 275 –277 vol.1, may 1995.

[BES] BESSY I. Website. Available online at `http://de.wikipedia.org/wiki/Berliner_Elektronenspeicherring-Gesellschaft_fr_Synchrotronstrahlung#BESSY_I`; visited on 29-Jul-2011.

[BFR+01] R. Brinkmann, K. Flöttmann, J. Roßbach, P. Schmüser, N. Walker, and H. Weise. TESLA technical design report part II: The accelerator. 2001.

[CAB+09] F. Curbis, A. Azima, J. Bödewadt, H. Delsim-Hashemi, M. Drescher, et al. Photon diagnostic for the seeding experiment at FLASH. In *Proceedings FEL Conference*, Liverpool, 2009.

[CAB+10] F. Curbis, A. Azima, J. Bödewadt, H. Delsim-Hashemi, M. Drescher, et al. Characterization of seeded FEL pulses at FLASH: Status, challenges and opportunities. In *Proceedings FEL Conference*, Malmö, 2010.

[CL84] R. Colella and A. Luccio. Proposal for a free electron laser in the x-ray region. *Optics Communications*, 50(1):41 – 44, 1984.

[Cor93] P. B. Corkum. Plasma perspective on strong field multiphoton ionization. *Phys. Rev. Lett.*, 71(13):1994–1997, Sep 1993.

[DES10] Photon science 2010 - highlights and HASYLAB annual report. page 220, Jul 2010.

[DH08] H. Delsim-Hashemi. *Infrared Single Shot Diagnostics for the Longitudinal Profile of the Electron Bunches at FLASH*. PhD thesis, Universität Hamburg, 2008.

[DHMR+09] H. Delsim-Hashemi, V. Miltchev, R. Roßbach, M. Tischer, et al. Status of the sFLASH undulator system. In *Proceedings FEL Conference*, Liverpool, 2009.

[DHRT+09] H. Delsim-Hashemi, R. Roßbach, M. Tischer, A. Schöps, and Y. Holler. Undulator system for a seeded FEL experiment at FLASH. In *Proceedings PAC Conference*, Vancouver, 2009.

[ea09] P. Salén et al. Results from the optical replica synthesizer at FLASH. In *Proceedings FEL*, Liverpool, 2009.

[ESR] European synchrotron radiation facility. Website. Available online at `http://www.esrf.eu`; visited on 04-Aug-2011.

[ESY00] E. Schneidmiller E. Saldin and M. Yurkov. *The Physics of Free Electron Lasers*. Springer- Verlag, Berlin, 2000.

[EXF] European XFEL. Website. Available online at `www.xfel.eu/de/`; visited on 04-Aug-2011.

[FBA+11] B. Faatz, N. Baboi, V. Ayvazyan, V. Balandin, W. Decking, S. Duesterer, H.-J. Eckoldt, J. Feldhaus, N. Golubeva, K. Honkavaara, et al. Flash II: Perspectives and challenges. *Nuclear Instruments and Methods in Physics Research Section A: Accelerators, Spectrometers, Detectors and Associated Equipment*, 635(1, Supplement):S2 – S5, 2011. ¡ce:title¿PhotonDiag 2010¡/ce:title¿.

[FBG+03] M. Felber, M. K. Bock, P. Gessler, K. E. Hacker, T. Lamb, F. Ludwig, H. Schlarb, and B. Schmidt. Rf-based synchronization of the seed and pump-probe lasers to the optical synchronization system at FLASH. In *Proceedings PAC*, Portland, 2003.

[FER] FERMI@elettra. Website. Available online at `http://www.elettra.trieste.it/FERMI/`; visited on 04-Aug-2011.

[FFK+99] B. Faatz, J. Feldhaus, J. Krzywinski, E. L. Saldin, E. A. Schneidmiller, and M. V. Yurkov. Regenerative FEL amplifier at the TESLA test facility at DESY. *Nuclear Instruments and Methods in Physics Research Section A: Accelerators, Spectrometers, Detectors and Associated Equipment*, 429(1-3):424 – 428, 1999.

[FHPW61] P. A. Franken, A. E. Hill, C. W. Peters, and G. Weinreich. Generation of optical harmonics. *Phys. Rev. Lett.*, 7(4):118–119, Aug 1961.

[FLA] FLASH at DESY. Website. Available online at `http://flash.desy.de/`; visited on 04-Aug-2011.

[FLL+88] M. Ferray, A. L'Huillier, X. F. Li, L. A. Lompre, G. Mainfray, and C. Manus. Multiple-harmonic conversion of 1064 nm radiation in rare gases. *Journal of Physics B: Atomic, Molecular and Optical Physics*, 21(3):L31, 1988.

[Frö06] L. Fröhlich. Thermal load on wirescanners in the FLASH linac. DESY Technical Note 2006-02, Jul 2006.

[Fri] Private communication with J. Frisch.

[FSS+97] J. Feldhaus, E. L. Saldin, J. R. Schneider, E. A. Schneidmiller, and M. V. Yurkov. Possible application of x-ray optical elements for reducing the spectral bandwidth of an x-ray sase fel. *Optics Communications*, 140(4-6):341 – 352, 1997.

[GDG+04] R. Ganter, M. Dehler, J. Gobrecht, C. Gough, G. Ingold, S.C. Leemann, et al. Ultra-low emittance electron gun project for FEL application. In *Proceedings LINAC*, Lübeck, 2004.

[GF45] V. L. Ginzburg and I. M. Frank. Radiation of a uniformly moving electron due to its transition from one medium into another. *J. Phys. (USSR)*, 9:353–362, 1945.

[Git92] B. Gitter. Optical transition radiation. *Tech. note in PBPL*, page 24, 1992.

[GKS10] G. Geloni, V. Kocharyan, and E. Saldin. Self-seeded operation of the LCLS hard x-ray FEL in the long-bunch mode. *ArXiv e-prints*, dec 2010.

[Ham] Hamamatsu photonics. Website. Available online at `http://www.hamamatsu.com/`; visited on 12-Aug-2011.

[Has11] E. Hass. Elektron- und Laserstrahldiagnostik mit Drahtscannern am XUV-seeding Experiment bei FLASH, 2011.

[HBC+08] U. Hahn, N.v. Bargen, P. Castro, O. Hensler, S. Karstensen, M. Sachwitz, and H. Thom. Wire scanner system for FLASH at DESY. *Nuclear Instruments and Methods in Physics Research Section A: Accelerators, Spectrometers, Detectors and Associated Equipment*, 592(3):189 – 196, 2008.

[HBF+03] K. Honkavaara, A. Brenger, R. Fischer, D. Nölle, K. Rehlich, et al. Design of OTR beam profile monitors for the TESLA test facility, phase 2 (TTF2). In *Proceedings PAC*, Portland, 2003.

[HGD93] B. L. Henke, E. M. Gullikson, and J. C. Davis. X-ray interactions: Photoabsorption, scattering, transmission, and reflection at e = 50-30,000 ev, z = 1-92. *Atomic Data and Nuclear Data Tables*, 54(2):181 – 342, 1993.

[Hip11] U. Hipp. Investigations on the wavefront of the seed laser at the XUV seeding experiment at FLASH, 2011.

[HK07] Z. Huang and K.-J. Kim. Review of x-ray free-electron laser theory. *Phys. Rev. ST Accel. Beams*, 10(3):034801, Mar 2007.

[HKM+02] J F Hergott, M Kovacev, H Merdji, C Hubert, Y Mairesse, E Jean, P Breger, P Agostini, B Carré, and P Salières. Extreme-ultraviolet high-order harmonic pulses in the microjoule range. *Physical Review A*, 66(2):2–5, 2002.

[HMS+09] Xinkui He, M. Miranda, J. Schwenke, O. Guilbaud, T. Ruchon, C. Heyl, E. Georgadiou, R. Rakowski, A. Persson, M. B. Gaarde, and A. L'Huillier. Spatial and spectral properties of the high-order harmonic emission in argon for seeding applications. *Phys. Rev. A*, 79(6):063829, Jun 2009.

[HR06] Z. Huang and R. D. Ruth. Fully coherent x-ray pulses from a regenerative-amplifier free-electron laser. *Phys. Rev. Lett.*, 96(14):144801, Apr 2006.

[ILC] International linear collider. Website. Available online at `http://www.linearcollider.org/`; visited on 04-Aug-2011.

[Joh98] Thomas F. Johnston. Beam propagation (m2) measurement made as easy as it gets: The four-cuts method. *Appl. Opt.*, 37(21):4840–4850, Jul 1998.

[KAB+10] M. Khojoyan, G. Asova, J. Bähr, H.J. Grabosch, L. Hakobyan, M. Hänel, Y. Ivanisenko, et al. Measurement and simulation studies of emittance for short gaussian pulses at pitz. In *Proceedings FEL Conference*, Malmö, 2010.

[KKM+11] A. Kaukher, I. Krouptchenkov, B. Michalek, D. Noelle, and H. Tiessen. XFEL beam loss monitor system. In *Proceedings DIPAC*, Hamburg, 2011.

[KL66] H. Kogelnik and T. Li. Laser beams and resonators. *Applied Optics*, 5(10):1550, 1966.

[KSR08] K.-J. Kim, Y. Shvyd'ko, and S. Reiche. A proposal for an x-ray free-electron laser oscillator with an energy-recovery linac. *Phys. Rev. Lett.*, 100(24):244802, Jun 2008.

[L+07] S. Lederer et al. Conditioning of a new gun cavity towards 60 mv/m at PITZ. In *Proceedings PAC Conference*, Albuquerque, 2007.

[LBI+94] M. Lewenstein, Ph. Balcou, M. Yu. Ivanov, Anne L'Huillier, and P. B. Corkum. Theory of high-harmonic generation by low-frequency laser fields. *Phys. Rev. A*, 49(3):2117–2132, Mar 1994.

[LCL] LCLS. Website. Available online at `http://lcls.slac.stanford.edu/`; visited on 04-Aug-2011.

[Leo94] W.R. Leo. *Techniques for nuclear and particle physics experiments: a how-to approach*. Springer, 1994.

[Löh09] F. Löhl. *Optical Synchronization of a Free-Electron Laser with Femtosecond Precision*. PhD thesis, Universität Hamburg, 2009.

[LHG+08] G. Lambert, T. Hara, D. Garzella, T. Tanikawa, M. Labat, B. Carre, H. Kitamura, et al. Injection of harmonics generated in gas in a free-electron laser providing intense and coherent extreme-ultraviolet light. *Nature Physics*, 4(4):296 – 300, Apr 2008.

[LSC+06] F. Löhl, S. Schreiber, M. Castellano, G. Di Pirro, L. Catani, A. Cianchi, and K. Honkavaara. Measurements of the transverse emittance at the FLASH injector at DESY. *Phys. Rev. ST Accel. Beams*, 9(9):092802, Sep 2006.

[LSKP+11] L.G. L.G. Sukhikh, K. Kube, Yu.A. Popov, A.P. Potylitsyn, D. Krambrich, and W. Lauth. Experimental investigations of backward transition radiation from flat target in extreme ultraviolet region. In *Proceedings DIPAC Conference*, Hamburg, 2011.

[LSL95] M. Lewenstein, P. Salières, and A. L'Huillier. Phase of the atomic polarization in high-order harmonic generation. *Phys. Rev. A*, 52(6):4747–4754, Dec 1995.

[MAB+08a] V. Miltchev, A. Azima, J. Bödewadt, M. Drescher, H. Delsim-Hashemi, S. Khan, T. Maltezopoulos, M. Mittenzwey, et al. Tolerance studies on the high harmonic laser seeding at FLASH. In *Proceedings FEL Conference*, Gyeongju, 2008.

[MAB+08b] V. Miltchev, A. Azima, J. Bödewadt, M. Drescher, H. Delsim-Hashemi, S. Khan, T. Maltezopoulos, M. Mittenzwey, J. Rossbach, R. Tarkeshian, et al. Experimental layout of 30 nm high-harmonic laser seeding at FLASH. In *Proceedings EPAC Conference*, Genoa, 2008.

[MCW+08] T. Maltezopoulos, S. Cunovic, M. Wieland, M. Beye, A. Azima, H. Redlin, M. Krikunova, and et al. Single-shot timing measurement of extreme-ultraviolet free-electron laser pulses. *New Journal of Physics*, 10(3):033026, 2008.

[Min04] M. Minty. Diagnostics. Cern Accelerator School, 2004.

[Mit11] M. Mittenzwey. *High Harmonic Generation for the XUV seeding experiment at FLASH*. PhD thesis, Universität Hamburg, 2011.

[MKZ00] Ch. Luschchik M. Kirm, A. Luschchik and G. Zimmerer. Investigation of luminescence properties of pure and ce3+ doped y3al5o12 crystals using vuv radiation. In *ECS Proceedings*, volume 99-40, pages 113–122, 2000.

[MRBZ+00] A. Murokh, J. Rosenzweig, I. Ben-Zvi, X. Wang, and V. Yakimenko. The physics of high brightness beams. In *Proceedings of the 2nd ICFA Advanced Accelerator Workshop*, page 564, Los Angeles, 2000.

[MRBZ+01] A. Murokh, J. Rosenzweig, I. Ben-Zvi, X. Wang, and V. Yakimenko. Limitations on measuring a transverse profile of ultradense electron beams with scintillators. In *Particle Accelerator Conference, 2001. PAC 2001. Proceedings of the 2001*, volume 2, pages 1333 –1335 vol.2, 2001.

[MSM+11] J. Mießner, M. Sachwitz, M. Markert, R. Sternberger, K. Tiedtke, and A. Hofmann. An ionization profile monitor for the determination of the FLASH photon beam parameter. *Nuclear Instruments and Methods in Physics Research Section A: Accelerators, Spectrometers, Detectors and Associated Equipment*, 635(1, Supplement 1):104 – 107, 2011. PhotonDiag 2010.

[MT01] G Materlik and Th. Tschentscher. TESLA technical design report part V: The x-ray free electron laser. 2001.

[NFG+97] Dinh C. Nguyen, C. M. Fortgang, J. C. Goldstein, J. M. Kinross-Wright, and R. L. Sheffield. Synchronously injected amplifiers, a novel approach to high-average-power FEL. *Nuclear Instruments and Methods in Physics Research Section A: Accelerators, Spectrometers, Detectors and Associated Equipment*, 393(1-3):252 – 256, 1997. Free Electron Lasers 1996.

[NSL] A brief history of the NSLS. Website. Available online at `http://www.nsls.bnl.gov/about/history/`; visited on 29-Jul-2011.

[NW04] D. Nölle and M. Wendt. Ttf2 beam monitors for beam position, bunch charge and phase measurements. In *Proceedings LINAC*, Lübeck, 2004.

[PET] PETRA III. Website. Available online at `http://petra3.desy.de`; visited on 04-Aug-2011.

[Pra09] E. Prat. *Spurious Dispersion Effects at FLASH*. PhD thesis, Universität Hamburg, 2009.

[PS09] S. Prestemon and R. Schlueter. Undulator options for soft x-ray free electron lasers. In *Proceedings FEL Conference*, Liverpool, 2009.

[Rei99] S. Reiche. GENESIS 1.3: a fully 3d time-dependent FEL simulation code. *Nuclear Instruments and Methods in Physics Research Section A: Accelerators, Spectrometers, Detectors and Associated Equipment*, 429(1-3):243 – 248, 1999.

[RGK+03] M. Richter, A. Gottwald, U. Kroth, A. A. Sorokin, S. V. Bobashev, L. A. Shmaenok, J. Feldhaus, Ch. Gerth, B. Steeg, K. Tiedtke, and R. Treusch. Measurement of gigawatt radiation pulses from a vacuum and extreme ultraviolet free-electron laser. *Applied Physics Letters*, 83(14):2970–2972, 2003.

[S+05] S. Schreiber et al. The injector of the VUV-FEL at DESY. In *Proceedings FEL Conference*, Standford, 2005.

[SAC] SACLA. Website (Japanese). Available online at `http://xfel.riken.jp/`; visited on 04-Aug-2011.

[SCC+00] R. W. Schoenlein, S. Chattopadhyay, H. H. W. Chong, T. E. Glover, P. A. Heimann, C. V. Shank, A. A. Zholents, and M. S. Zolotorev. Generation of femtosecond pulses of synchrotron radiation. *Science*, 287(5461):2237–2240, 2000.

[Sch] Schott BG39 glass filter data. Website. Available online at `http://www.optical-filters.com/bg39.html`; visited on 12-Aug-2011.

[SDP+96] P. Salieres, T. Ditmire, M. D. Perry, A. L'Huillier, and M. Lewenstein. Angular distributions of high-order harmonics generated by a femtosecond laser. *Journal of Physics B: Atomic, Molecular and Optical Physics*, 29(20):4771, 1996.

[SDR09] P. Schmüser, M. Dohlus, and J. Rossbach. *Ultraviolet and Soft X-Ray Free-Electron Lasers*. 2009.

[SFF+09] S. Schreiber, B. Faatz, J. Feldhaus, K. Honkavaara, and R. Treusch. FLASH operation as an FEL user facility. In *Proceedings PAC Conference*, Vancouver, 2009.

[SFF+10] S. Schreiber, B. Faatz, J. Feldhaus, K. Honkavaara, R. Treusch, and M. Vogt. FLASH upgrade and first results. In *Proceedings FEL Conference*, Malmö, 2010.

[SFH08] S. Schreiber, B. Faatz, and K. Honkavaara. Operation of FLASH at 6.5 nm wavelength. In *Proceedings EPAC Conference*, Genoa, 2008.

[SFK+11] B. Schutte, U. Fruhling, R. Kalms, M. Wieland, A. Azima, and M. Drescher. Xuv femtosecond pulse width characterization with a laser-based terahertz-field-driven streak camera. In *Lasers and Electro-Optics (CLEO), 2011 Conference on*, pages 1 –2, may 2011.

[SiG] Data sheet, si scientific instruments gmbh.

[SLAL97] P. Salieres, A. L'Huillier, P. Antoine, and M. Lewenstein. Study of the spatial and temporal coherence of high order harmonics. 1997.

[SPR] SPring-8. Website. Available online at `http://http://www.spring8.or.jp/`; visited on 04-Aug-2011.

[ST07] B.E.A. Saleh and M.C. Teich. *Fundamentals of photonics*. Wiley series in pure and applied optics. Wiley-Interscience, 2007.

[STH+08] T. Shintake, H. Tanaka, T. Hara, T. Tanaka, K. Togawa, Ma. Yabashi, Y. Otake, et al. A compact free-electron laser for generating coherent radiation in the extreme ultraviolet region. *Nature Photonics*, 2(9):555 – 559, Sep 2008.

[Stu04] F. Stulle. *A Bunch Compressor for small Emittances and high Peak Currents at the VUV Free-Electron Laser*. PhD thesis, Universität Hamburg, 2004.

[Stu09] G. Stupakov. Using the beam-echo effect for generation of short-wavelength radiation. *Phys. Rev. Lett.*, 102(7):074801, Feb 2009.

[SW09] G.R. Shorack and J.A. Wellner. *Empirical Processes with Applications to Statistics*. Classics in Applied Mathematics. Society for Industrial and Applied Mathematics, 2009.

[TAB+11] R. Tarkeshian, A. Azima, J. Bödewadt, F. Curbis, and et al. Femtosecond resolved determination of electron beam and XUV seed pulse temporal overlap in sFLASH. In *Proceedings PAC Conference*, New York, 2011.

[Tar11] R. Tarkeshian. *Femtosecond Resolved Diagnostics for Electron Beam and XUV Seed Temporal Overlap at sFLASH*. PhD thesis, Universität Hamburg, 2011.

[TAvB+09] K. Tiedtke, A. Azima, N. von Bargen, L. Bittner, S. Bonfigt, S. Düsterer, B. Faatz, U. Frühling, M. Gensch, Ch. Gerth, N. Guerassimova, U. Hahn, et al. The soft x-ray free-electron laser FLASH at DESY: beamlines, diagnostics and end-stations. *New Journal of Physics*, 11(2):023029, 2009.

[TBB+07] M. Tischer, M. Barthelmess, M. Bräuer, U. Englisch, J. Pflüger, and J. Skupin. Insertion devices for the PETRA III storage ring. *AIP Conference Proceedings*, 879(1):343–346, 2007.

[TEM+10] M. Tischer, U. Englisch, T. Müller, A. Schöps, P. Vagin, et al. Undulator of the sFLASH experiment. In *Proceedings IPAC Conference*, Kyoto, 2010.

[TFH+08] K. Tiedtke, J. Feldhaus, U. Hahn, U. Jastrow, T. Nunez, T. Tschentscher, S. V. Bobashev, A. A. Sorokin, J. B. Hastings, S. Möller, et al. Gas detectors for x-ray lasers. *Journal of Applied Physics*, 103(9):094511, 2008.

[TSB+04] K. Togawa, T. Shintake, H. Baba, T. Inagaki, K. Onoe, and T. Tanaka. Low emittance 500 kv thermionic electron gun. In *Proceedings LINAC Conference*, Lübeck, 2004.

[Wen11] M. Wendt. Overview of recent trends and developments for bpm systems. In *Proceedings DIPAC Conference*, Hamburg, 2011.

[Wie03a] H. Wiedemann. *Particle Accelerator Physics*. Number Bd. 1 in Physics and astronomy online library. Springer, 2003.

[Wie03b] H. Wiedemann. *Particle Accelerator Physics: Nonlinear and higher-order beam dynamics*. Particle Accelerator Physics. Springer, 2003.

[Win98] David L. Windt. Imd—software for modeling the optical properties of multilayer films. *Computers in Physics*, 12(4):360–370, 1998.

[Wiz79] Joseph Ladislas Wiza. Microchannel plate detectors. *Nuclear Instruments and Methods*, 162(1-3):587 – 601, 1979.

[WKBB+10] W. W. Koprek, C. Behrens, M. K. Bock, M. Felber, P. Gessler, K. Hacker, H. Schlarb, C. Schmidt, B. Steffen, and S. Wesch. Intra-train longitudinal feedback for beam stabilization at FLASH. In *Proceedings FEL Conference*, Malmö, 2010.

[WS11] S. Wesch and B. Schmidt. Summary of COTR effects. In *Proceedings DIPAC Conference*, Hamburg, 2011.

[WY01] Juhao Wu and Li Hua Yu. Coherent hard x-ray production by cascading stages of high gain harmonic generation. *Nuclear Instruments and Methods in Physics Research Section A: Accelerators, Spectrometers, Detectors and Associated Equipment*, 475(1-3):104 – 111, 2001.

[WYD+11] A. Willner, M. Yeung, T. Dzelzainis, C. Kamperidis, M. Bakarezos, D. Adams, V. Yakovlev, F. Tavella, and et al. Complete control of high-harmonic generation for high average power applications. In *Quantum Electronics and Laser Science Conference*. Optical Society of America, 2011.

[XCD+10] D. Xiang, E. Colby, M. Dunning, S. Gilevich, C. Hast, K. Jobe, D. McCormick, J. Nelson, T. O. Raubenheimer, K. Soong, G. Stupakov, Z. Szalata, D. Walz, S. Weathersby, M. Woodley, and P.-L. Pernet. Demonstration of the echo-enabled harmonic generation technique for short-wavelength seeded free electron lasers. *Phys. Rev. Lett.*, 105(11):114801, Sep 2010.

[YBG+11] M. Yan, C. Behrens, Ch. Gerth, G. Kube, B. Schmidt, and S. Wesch. Suppression of coherent optical transition radiation in transverse beam diagnostics by utilizing a scintillation screen with a fast gated ccd camera. In *Proceedings DIPAC Conference*, Hamburg, 2011.

[ZEM] Zemax: Software for optical system design. Radiant ZEMAX LLC.

[Zho05] Alexander A. Zholents. Method of an enhanced self-amplified spontaneous emission for x-ray free electron lasers. *Phys. Rev. ST Accel. Beams*, 8(4):040701, Apr 2005.

Danksagung

Allen, die zum Gelingen dieser Arbeit beigetragen haben, möchte ich an dieser Stelle danken. Meinem Doktorvater Prof. Dr. Shaukat Khan sowie Prof. Dr. Markus Drescher und Prof. Dr. Jörg Roßbach möchte ich für ihr Vertrauen und ihre Unterstützung danken, und dass sie mir die Möglichkeit gaben, an diesem überaus spannenden Projekt mitzuarbeiten.

Außerdem gilt der Dank dem gesamten sFLASH Team sowie allen Mitarbeitern der Werkstätten und technischen Gruppen der Universität Hamburg und des DESY, ohne die der Aufbau und die Realisierung dieses Projektes nicht möglich gewesen wären. Namentlich möchte ich hier Josef Gonschior sowie Otto Peters erwähnen, die mit ihrer Erfahrung und ihrer Kreativität einen großen Beitrag dazu geleistet haben, manchmal auch unmöglich erscheinende Ideen umzusetzen oder auch zu verwerfen, wenn sie einen einfacheren oder besseren Lösungsweg kannten.

Für die zahlreichen Kommentare und Verbesserungsvorschläge sowie die Korrekturen dieser Arbeit, möchte ich Dr. Juliane Rönsch-Schulenburg, Dr. Theophilos Maltezopoulos, Dr. Velizar Miltchev und Dr. Katja Honkavaara danken.

Zum Schluss möchte ich mich bei meiner Familie bedanken, insbesondere meiner Frau Julika und meinem beiden entzückenden Kindern Johann und Lenja. Gerade während der Schichtblöcke und während der letzten Monate dieser Arbeit wurde ihre Geduld des Öfteren auf die Probe gestellt. Für ihre Liebe und die Kraft, die sie mir geben, gibt es keine passenden Worte.

Vielen, vielen Dank.